Theylor Schumacher Klippel

Asteroseismology of massive ZZ Ceti stars: An updated grid of fully evolutionary models

Brasil

07/10/2021

Theylor Schumacher Klippel

Asteroseismology of massive ZZ Ceti stars: An updated grid of fully evolutionary models

Dissertação submetida ao Programa de Pós Graduação em Física do Instituto de Física da UFRGS, como quesito parcial para obtenção do título de Mestre em Física, com ênfase em Astronomia.

Universidade Federal do Rio Grande do Sul – UFRGS

Instituto de Física

Programa de Pós-Graduação

Supervisor: Prof. Dr. Alejandra Daniela Romero

Co-supervisor: Prof. Dr. Kepler de Souza Oliveira Filho

Brasil

07/10/2021

Theylor Schumacher Klippel
Asteroseismology of massive ZZ Ceti stars:
An updated grid of fully evolutionary models/ Theylor Schumacher Klippel. –
Brasil, 07/10/2021-
104 p. : il. (algumas color.) ; 30 cm.

Supervisor: Prof. Dr. Alejandra Daniela Romero

Master Thesis – Universidade Federal do Rio Grande do Sul – UFRGS
Instituto de Física
Programa de Pós-Graduação, 07/10/2021.

1. Palavra-chave1. 2. Palavra-chave2. I. Orientador. II. Universidade xxx. III.
Faculdade de xxx. IV. Título

CDU 02:141:005.7

Theylor Schumacher Klippel

Asteroseismology of massive ZZ Ceti stars: An updated grid of fully evolutionary models

Dissertação submetida ao Programa de Pós Graduação em Física do Instituto de Física da UFRGS, como quesito parcial para obtenção do título de Mestre em Física, com ênfase em Astronomia.

Prof. Dr. Alejandra Daniela Romero
Orientador

Prof. Dr. Kepler de Souza Oliveira Filho
Coorientador

Professor
Barbara Castanheira

Professor
Antônio Kanaan

Professor
José Eduardo da Silveira Costa

Brasil
07/10/2021

Dedico aos meus pais e a minha companheira de longa data

Acknowledgements

Fazer um mestrado acadêmico era algo impensável para o Theylor do ensino médio. Apesar de reconhecer as minhas limitações, principalmente por não ter tido um ensino de qualidade, eu persisti. Consegui obter meu diploma, em mais tempo do que várias pessoas é verdade, mas com muito esforço e dedicação. Por fim, consegui entrar no mestrado, onde consegui terminar o trabalho iniciado na graduação. Foram vários aprendizados, entre eles a escrita de uma dissertação e de um artigo em língua inglesa e, também, aventuras por terras estrangeiras. Obrigado pela hospitalidade Universidad Nacional de la Plata. Entretanto, nem tudo são flores. No mestrado eu também desenvolvi diversos problemas psicológicos, e o pior deles foi sem dúvida a ansiedade. A academia é um ambiente hostil, e é difícil manter-se nos eixos.

Quem me manteve em pé para enfrentar todas as adversidades de uma pós-graduação foi minha namorada, Thayana. Eu não seria nada sem você do meu lado todos os dias, desde sempre. Tu és o que tenho de mais importante na vida!

Uma das melhores coisas que o fim da graduação e o mestrado me trouxeram foram minhas grandes amigas Jamile e Larissa. Sem nossas conversas diárias, os sermões e os incentivos, teria sido impossível concluir o mestrado. Obrigado pelas inúmeras contribuições para a construção dessa dissertação.

Agradeço também os meus orientadores Profa. Dra. Alejandra e Prof. Dr. Kepler pelos aprendizados e por darem um norte para minha pesquisa.

Agradeço a UFRGS e o departamento de astronomia por me fornecerem um local adequado e um bom computador para a realização deste trabalho.

Por fim, meu muito obrigado a CAPES por ter financiado a minha pesquisa.

"Os que se encantam com a prática sem a ciência são como os timoneiros que entram no navio sem timão nem bússola, nunca tendo certeza do seu destino". (Leonardo da Vinci)

Abstract

White dwarfs stars are by far the most common outcome of stellar evolution, being the final product of more than 95% of all stars in the Milk Way. During their evolution, the white dwarf stars cross several zones known as pulsational instability strips. This allows us to study the white dwarf stars through asteroseismology, which is a technique that exploits the comparison between observed periods and the periods computed using theoretical models. With asteroseismology, we can study the evolutionary and structural properties of pulsating stars. For white dwarf stars ,it is a powerful tool to estimate the mass of hydrogen and helium envelopes and to infer the stellar mass with accuracy. In this work, I present an asteroseismological study of 40 massive variable DA white dwarf stars known as ZZ Ceti stars. The sample has spectroscopic masses above $0.74 M_{\odot}$ and includes SDSSJ181222.74+432107.6, the new massive ZZ Ceti discovered within the TESS mission. To this end, I updated the grid of fully evolutionary carbon-oxygen core DA white dwarf models generated using LPCODE, adding $\sim$500 sequences in the white dwarf cooling curve. For each stellar mass, I expanded the model grid in hydrogen envelope mass, in steps of 0.1 on a logarithmic scale for $\log(\mathrm{M_H}/\mathrm{M_\star})$ from -4 to -6, and in steps of 0.5 for values below. In addition, three new cooling sequences with white dwarf masses of 0.8, 0.86 and 0.9 $\mathrm{M_\odot}$ were included, in order to fill some gaps in the stellar mass present in the original grid. I study the distribution of log(g), effective temperature, and hydrogen envelope thickness. The mean value of the sample for the asteroseismological mass is $\langle M_\star \rangle_{\mathrm{sis}} = 0.84 \pm 0.04 M_{\odot}$, which is in excellent agreement with the value obtained for the mean spectroscopic mass $\langle M_\star \rangle_{\mathrm{spec}} = 0.84 \pm 0.07 M_{\odot}$. The mean hydrogen envelope mass of $\langle \mathrm{M_H} \rangle = 9 \times 10^{-7} \mathrm{M_\star}$. For 36 out of the 40 stars analyzed, I have found a best-fit model with less hydrogen than that predicted by standard evolutionary computations. I also conclude that the DAVs in the domain of thick envelopes usually have less hydrogen than what was expected by the prior evolution.

Key words: white dwarfs. zz cetis. variability. asteroseismology. stellar evolution.

Resumo

As estrelas anãs brancas são o resultado mais comum da evolução estelar, sendo o produto final de mais de 95% das estrelas da nossa Galáxia. Durante a sua evolução, as estrelas anãs brancas atravessam diversas zonas conhecidas como faixas de instabilidade, em que essas estrelas irão apresentar pulsações. Isto nos permite estudar as estrelas anãs brancas através da asterosismologia, que é uma técnica que explora a comparação entre períodos observados e períodos calculados, usando modelos teóricos. Com a asterosismologia, nós podemos estudar as propriedades evolucionárias e estruturais das estrelas pulsantes. Além disso, ela também é uma poderosa ferramenta para determinar a massa de envelopes de hidrogênio e de hélio, assim como para inferir massas estelares com acurácia. Neste trabalho, eu apresentou um estudo asterosismológico de 40 anãs brancas massivas DA variáveis, conhecidas como estrelas ZZ Ceti. A amostra possui massas espectroscópicas acima de $0.74M_{\odot}$ e inclui a estrela SDSSJ181222.74+432107.6, a nova ZZ Ceti massiva descoberta na missão TESS. Para este fim, eu atualizei uma grade de modelos completamente evolucionários de anãs brancas DAs com núcleo de carbono e oxigênio calculados através do LPCODE, adicionando ~ 500 sequências para a curva de esfriamento das anãs brancas. Para cada massa estelar, eu atualizei a grade de modelo adicionando novas massas para o envelope de hidrogênio em passos de 0.1 em escala logarítmica para $\log(\mathrm{M_H/M_\star})$, partindo de -4 até -6, e em passos de 0.5 para valores abaixo disso. Além disso, três novas sequências de esfriamento com massas de anã branca de 0.8, 0.86 e 0.9 $\mathrm{M_\odot}$ foram incluídas para preencher uma lacuna na massa estelar da grade original. Eu estudei a distribuição de log(g), temperatura efetiva e espessura do envelope de hidrogênio. O valor médio obtido para massa asterosismológica da amostra foi de $\langle M_\star \rangle_{\mathrm{sis}} = 0.84 \pm 0.04 M_\odot$. Este valor está em excelente concordância com o valor médio para a massa espectroscópica que é de $\langle M_\star \rangle_{\mathrm{spec}} = 0.84 \pm 0.07 M_\odot$. O valor médio obtido para a massa de hidrogênio foi de $\langle \mathrm{M_H} \rangle = 9 \times 10^{-7} \mathrm{M_\star}$. Em 36 das 40 estrelas analisadas, eu encontrei um modelo de melhor ajuste com menos hidrogênio do que o esperado por cálculos evolucionários. Conclui-se que as estrelas ZZ Ceti, no domínio de envelopes espessos, possuem menos hidrogênio do que o esperado pela evolução prévia.

Palavras-chave: Anãs brancas. zz cetis. variabilidade. asterosismología. evolução estelar.

Press Release

Você já ouviu falar nas estrelas anãs brancas? Essas estrelas são o que restam depois que estrelas como o Sol morrem e, em geral, é possível descrever com muita precisão seu comportamento. São objetos muito estudados por diversos grupos de pesquisa ao redor do mundo. Essas estrelas possuem mais ou menos o tamanho do nosso planeta e, além disso, são objetos bastante comuns no universo. Recentemente, a missão GAIA da Agência Espacial Europeia (ESA), que busca mapear o céu determinando a distância das estrelas, publicou dados de cerca de 230 000 anãs brancas, muitas delas nunca antes observadas. Embora sejam pequenas, essas estrelas abrigam muita informação sobre diversas áreas da física em seu interior. Como por exemplo, informações sobre física de partículas, física de plasmas e altas energias, além da astronomia. Em geral, as informações obtidas com essas estrelas seriam impossíveis de serem obtidas com os laboratórios que possuímos aqui na Terra.

Toda a informação que temos das estrelas anãs brancas é obtida através da luz que elas emitem. Em grandes telescópios aqui na Terra, ou até mesmo no espaço, a luz que provém desses objetos é coletada e processada para que seja possível realizar estudos utilizando esses dados. Através desses dados, por exemplo, é possível obter a informação do período de pulsação das estrelas ZZ Ceti, que são um tipo específico de estrela anã branca pulsante. Os períodos de pulsação, aliado a uma técnica chamada de asterosismologia, permitem obter diversas informações dessas estrelas, como sua massa, temperatura e quantidade de hidrogênio.

Para obter essas informações através da asterosismologia é necessário que se realizem simulações, o que torna possível comparar os períodos que são observados com os períodos obtidos por modelos no computador. No meu trabalho de mestrado, sob orientação da Prof Dra. Alejandra Romero e do Prof Dr. Kepler de Oliveira, eu estudei esses objetos buscando determinar as propriedades de um grupo de 40 ZZ Cetis, como sua distribuição de massa, quantidade de hidrogênio e temperatura. Um dos resultados que obtive através desse estudo foi de que essas estrelas possuem uma menor quantidade de hidrogênio do que o esperado.

Além disso, eu espero que as simulações que realizei neste trabalho possam ajudar diversas outras pesquisas no futuro, melhorando não só nossa compreensão sobre as estrelas anãs brancas, mas também ajudando a montar os blocos que formam nossa compreensão do universo.

List of Figures

List of Tables

List of abbreviations and acronyms

ZAMS	Zero age main sequence
MS	Main sequence
CNO	Carbon-nitrogen-oxygen cycle
p-p	Proton-proton cycle
RGB	Red giant branch
HB	Horizontal Branch
AGB	Assymptotic giant branch
WD	White dwarf
SN	Supernova
IMF	Initial mass function
SDSS	Sloan Digital Sky Survey
LTP	Late thermal pulse
VLTP	Very Late thermal pulse
IFMR	Initial-to-final mass relation
HR	Hertzsprung Russell diagram
ZZ Ceti	Hydrogen-dominated pulsating white dwarfs
LPCODE	La Plata Evolutioary Code

List of symbols

$M_{\odot}$	Solar mass
$\mathrm{T_{eff}}$	Effective temperature
DA	White dwarfs with hydrogen atmospheres
non-DA	White dwarfs deficients in hydrogen
$\mathrm{M_H}$	Hydrogen mass
$\mathrm{M_\star}$	Stellar mass
ρ	Density
P	Pressure
T	Temperature
$\vec{u}$	Flux velocity
S	Specific entropy
Φ	Gravitational potential
$\vec{f}$	External eletromagnetic forces
Θ	Viscosity tensor
ϵ_N	Nuclear energy generation rate
ϵ_V	Heat generated by viscosity
$\vec{F_R}$	Radiation energy flux
∇	Gradient operator
f'	Eulerian perturbation of a physical parameter f
$Y_\ell^m(\theta,\phi)$	Spherical harmonics
$e^{(i\sigma_{k,\ell,m}t}$	Oscillation frequency
$f'_{k,\ell,m}(r)$	Radial part of the eigenfunctions
k	Radial order

ℓ	Harmonic degree
m	Azimuthal order
N	Brunt-Väisälä frequency
L_ℓ	Lamb frequency
Γ_1	Adiabatic exponent
c_s^2	Adiabatic local sound velocity
$\mathrm{k_r}$	Radial wavenumber

Contents

1 Introduction

1.1 Stellar evolution

Stars are formed from a massive interstellar cloud of gas and dust. This cloud will remain in hydrostatic equilibrium as long as the gas pressure is in balance with the potential energy of the internal gravitational force. If the cloud has a mass above a mass limit called the Jeans Mass (around 10 000 $M_\odot$ for low metallicity), the cloud will collapse due to gravity. During the collapse, several protostellar clouds are formed by fragmentation. These clouds will contract until the gas becomes hot enough for the internal pressure to support further gravitational collapse. The resulting object is known as a protostar. For protostars with masses lower than 0.08 $M_\odot$, depending on metallicity,[1] the temperature required to start the hydrogen-burning ($\sim 10^6$ K) is never reached. In this case, the contraction stops when the matter becomes degenerate, forming what it is called a brown dwarf.[2] For protostars with masses above 0.08 $M_\odot$, the central region will become dense and opaque and it will reach the temperature necessary to burn hydrogen into helium. If that happens to occur, the gravitational contraction becomes balanced by the pressure exerted by the nuclear reactions and the protostar soon enters the *Main Sequence* (MS).

When the stars are burning hydrogen into helium and are in hydrostatic equilibrium, they are in the Main Sequence, the longest evolutionary stage in the life of the stars. The time that a star expends in the main sequence is related to its mass. A rough estimate of the time spent in the main sequence is given by

$$t_{MS} \approx 10^{10} \left(\frac{M}{M_\odot} \right)^{-2} \text{years} \tag{1.1}$$

This holds for stars up to ~ 3 $M_\odot$, but can be a good estimate up to ~ 60 $M_\odot$ if the effects of metallicity are ignored. The higher the metallicity, the longer the time spent in the main sequence, due to the increase in the opacity that decreases the luminosity of the star. For instance, a star with an initial mass of 20 $M_\odot$ has a lifetime in the MS of 1 million years, while a 1 $M_\odot$ star has a lifetime of 10 billion years.

After a star is formed, its temperature and luminosity continuously change over time. These two quantities are very important, being used to track the evolution of the stars. Figure 1 shows a Hertzprung-Russel diagram in which the effective temperatures of the stars are plotted as a function of their luminosity. Where a star will be placed in an HR diagram depends mainly on its mass and evolutionary stage. Due to this, the stars of

[1] in Astronomy, all elements heavier than helium are historically referred to as metals

[2] This section is based on the book "Stellar Structure and Evolution", Kippenhahn, Rudolf, Weigert, Alfred, Weiss, Achim, 2012 [10]

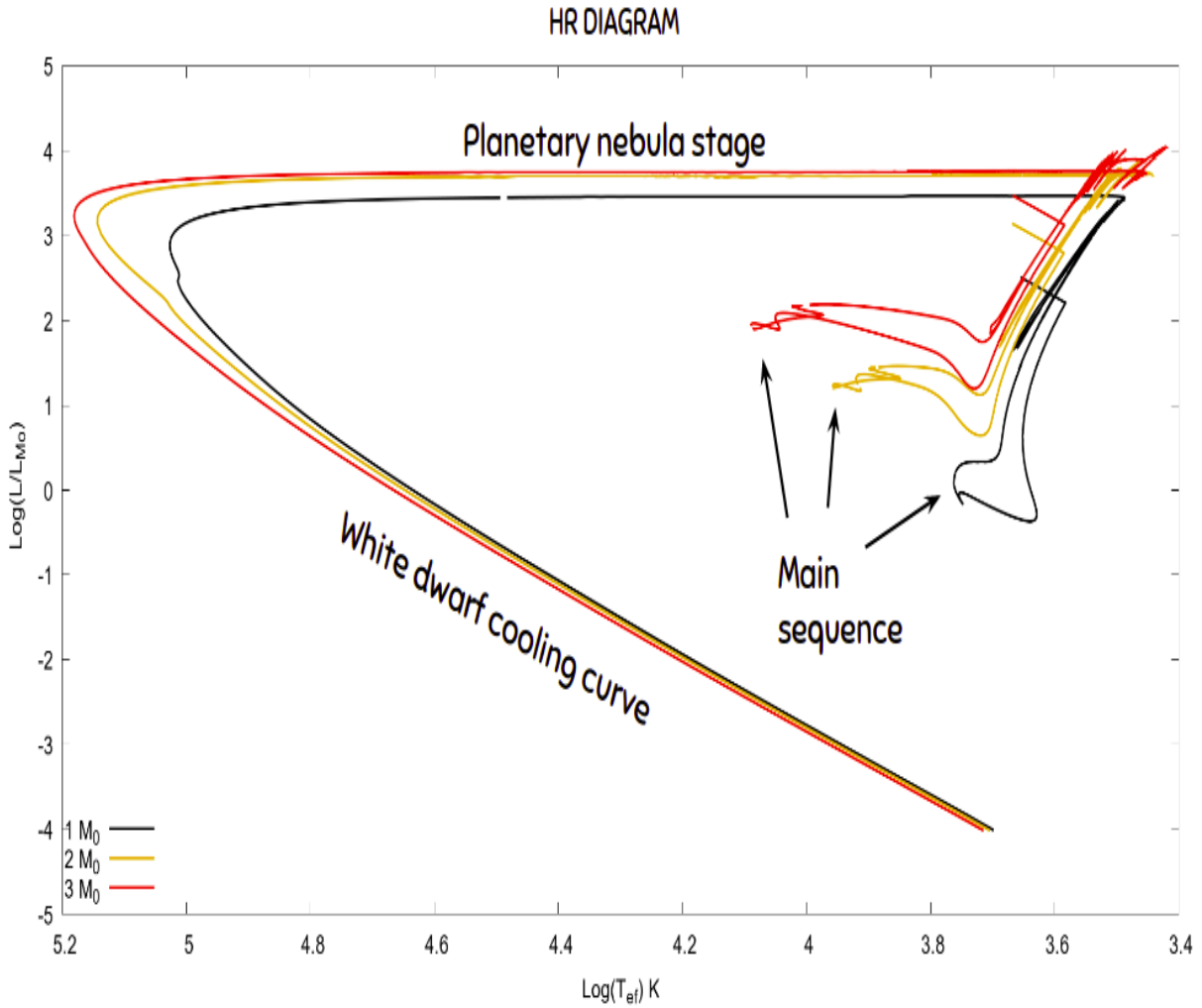

Figure 1 – Hertzprung-Russel diagram where the effective temperature of the stars are plotted in function of their luminosity. The position of a star in the diagram provides information about its present stage and mass. The colors represent different masses at zero age main sequence.

different masses and ages populate distinct regions of the HR diagram The hot and blue stars are placed on the left whereas the cold and red stars are placed on the right. The diagonal stripe in the diagram is the main sequence. The massive stars, which have blue or even white colors, are located in the upper left end of the main sequence, while the intermediate-mass stars, which have a yellow color, like the Sun, are found in the mid-way. Low mass stars, characterized by a red color, are found towards the lower right.

For stars with masses up to 1.25 $M_{\odot}$ the fusion channel is the proton-proton (p - p) chain reaction, in which protons are directly combined to form helium. Above this mass, for stars with non-zero metallicity, the nuclear process mainly uses atoms of carbon, nitrogen and oxygen as intermediaries in the CNO cycle.

The central burning of hydrogen ceases when the star has converted 10% of its initial mass into helium. This is the so-called Schoenberg-Chadrasekhar limit [11], and

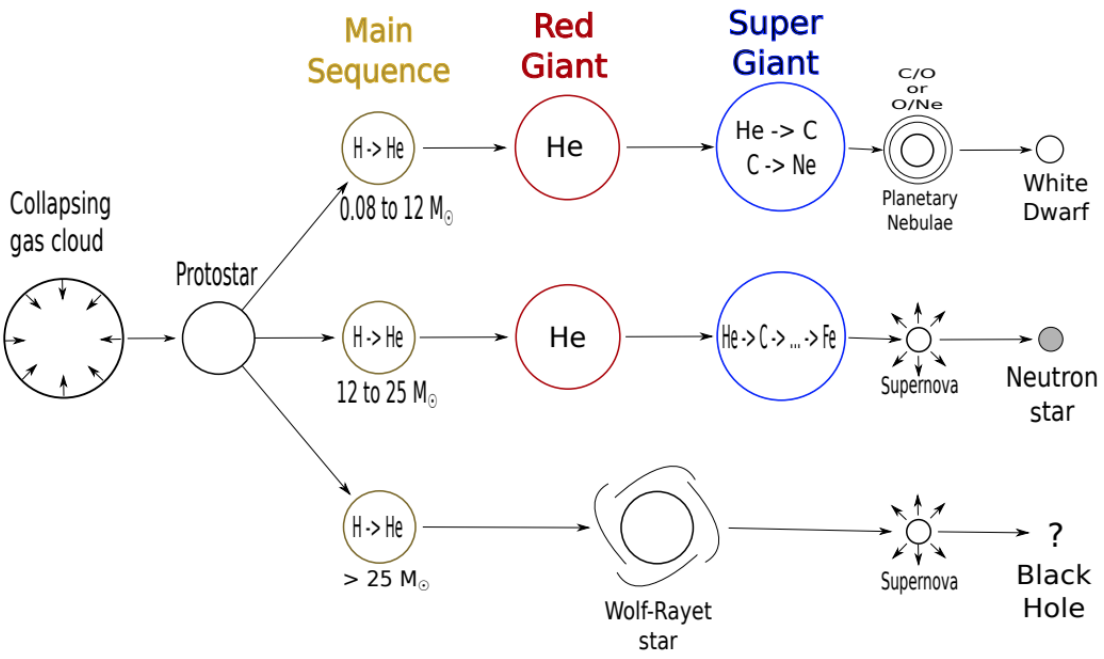

Figure 2 – Evolutionary paths that a single star may follow according to its mass. Extracted from Gabriel Lauffer Master Dissertation (2018) - Universidade Federal do Rio Grande do Sul

once it is reached, the internal pressure will not be enough to balance the gravitational collapse, and the star starts to contract. During the contraction, half of the energy will be released, according to the virial theorem, which causes the outer layers of the star to expand. This expansion of the envelope reduces the effective temperature and the star goes to the *Red giant branch* (RGB) phase. The decrease in the temperature causes the radiative transport become not enough to maintain the radiative equilibrium. Due to this, the star becomes almost fully convective, approaching the Hayashi limit, where stars are fully convective [12]. In this stage, the stars have their luminosity increased at an almost constant effective temperature. The shell around the inert helium core is still burning hydrogen, which increases the mass of the core. The growth of the core mass results in contraction and an increase in its temperature. When the core temperature reaches $\sim 10^8$ K, the burning of helium into carbon via triple-α process starts. This stage in stellar evolution is called *Horizontal Branch* (HB), which is similar to the main sequence, but helium is burnt in the core, instead of hydrogen.

What happens after the helium-burning stage depends on the mass and metallicity of the star at the beginning of the MS. Considering single stellar evolution (as along all this work) and solar metallicity, the stars can be divided into three main evolutionary paths, shown in Figure 2: the stars in the mass range of $0.08M_\odot \leq M \leq\sim 12M_\odot$, those with masses between $\sim 12M_\odot \leq M \leq 25M_\odot$ and the ones with $M \geq 25M_\odot$.

The stars in the mass range of $0.08M_{\odot} \leq M \leq\sim 12M_{\odot}$ develop a degenerate and inert core of carbon and oxygen, surrounded by a helium layer. Once there are no nuclear reactions in the core, the core contracts and the envelope expands. With the expansion of the envelope, the luminosity increases and the star reach the *Asymptotic giant branch* (AGB).

During the AGB, the scenario is similar to that presented in the RGB, but instead of only one energy source, there are two: the one originating from the hydrogen-burning layer; and another one from the helium burning layer which surrounds the inert carbon and oxygen core. With time, the helium burning layer becomes thinner, triggering an unstable energy production. These instabilities mark the beginning of the thermal pulse stage. As the star goes through the AGB, the core mass increases due to the constant deposit of carbon and oxygen by the helium burning layer. In addition, a large amount of mass is lost due to mass loss in the form of stellar wind. The thermal pulses produce periods of high mass loss, resulting in detached shells of circumstellar material. A star may lose 50 to 70% of its mass during the AGB phase. What it is left is a degenerate object with a small hydrogen and helium envelope, that has approximately the size of the Earth. The material that was ejected forms what it is called *Planetary Nebula*, which will shine for tens or even hundreds of years due to ultraviolet radiation coming from the central remaining object. When the gas dissipates and gets lost in the interstellar medium, what it is left is a *White Dwarf* star (WD).

For the stars with masses between ~ 11 $M_{\odot}$ and 25 $M_{\odot}$ the carbon/oxygen core does not become degenerate. The contraction of the core will be enough for it to reach the temperature of carbon fusion ($\sim 10^9$ K). Then, the star evolves burning all the elements heavier than carbon until iron is synthesised. When the star forms iron, it cannot generate energy via nuclear fusion, since the binding energy of iron is maximal. At this point, the only energy source is the gravitational contraction, which increases the temperature and causes the disassociation of the atomic nuclei into protons and neutrons. With the increase in the density, the protons capture the electrons to form neutrons, emitting neutrinos. At some point, the neutrons will form a degenerate gas. The gas becomes incompressible and stops the gravitational collapse of the outer layers. The result of this process is a shock wave which, allayed with the neutrinos emission, transfers momentum to the envelope and ejects the outer layers into a *Supernova* (SN) explosion that shines for a couple of minutes. The remaining object is a degenerate core composed of neutrons.

Stars with masses above 25 $M_{\odot}$ expend most of their evolution as Wolf-Rayet stars, which are very luminous objects. The stars in this mass range have strong convection, thus, the processed material from the core gradually reaches the surface. When in a sufficient amount, these materials absorb all the incoming radiation, creating strong winds. These winds cause a mass loss rate of 10^{-5} - $10^{-5}M_{\odot}$/year. The physical processes inside stars

with masses above 25 $M_\odot$ are believed to be similar as in stars in the mass range of $\sim 12M_\odot \leq M \leq 25M_\odot$, with the iron core leading to a supernova event. However, in this case, the mass of the core is too high and the pressure due to the neutron degenerate gas is not enough to balance the gravitational collapse. The contraction of the core leads to the formation of a *Black Hole*.

1.2 White Dwarf Stars

White dwarfs are by far the most common outcome of stellar evolution. They represent the final stage of all-stars with an initial mass lower than 7 - 11.8 $M_\odot$, depending on their metallicity [13, 14, 15, 16]. We can directly estimate the expected percentage of white dwarf stars in the Galaxy using the Salpeter Initial Mass Function [17]. Considering the upper limit for the solar metallicity $M = 12M_\odot$ and the IMF for the stars in the solar neighborhood $\xi(M) = 0.06M^{-2.35}$, we have:

$$\int_{0.1}^{12} 0.06M^{-2.35}dM = \frac{0.06}{1.35}(0.1^{-1.35} - 12^{-1.35}) = 0.993, \tag{1.2}$$

which implies that 99% of the stars in the Galaxy will become white dwarf stars.

Most of the white dwarf stars start their lives surrounded by a planetary nebula at very high temperatures. Since at this point the star has no considerable energy source, it begins to cool down. The degenerate core prevents any gravitational contraction, leading to an evolution with an almost constant radius. The degeneracy in the core is responsible for the singular characteristic of the white dwarfs to have have their radius inversely proportional to the mass. This implies that a white dwarf with a higher mass will be smaller than one with a lower mass. The existence of a mass limit that no white dwarf star can exceed without collapsing is also a consequence of electron degeneracy. This mass limit is known as the *Chandrasekhar limit*, with a value of $\approx 1.4M_\odot$, when the electron velocity approaches the speed of light.

Also because of the electron degeneracy, white dwarfs have an almost isothermic core. Despite that, the variation of the temperature between the center and the surface of the white dwarfs can reach $\sim 10^7$ K. The large temperature difference between the surface and the core occurs mainly in the envelope of the star. In cold stars, this temperature gradient opens the way for the formation of convective zones in the surface. The cooling rate of white dwarfs is therefore directly affected by the presence of convection. This occurs when the convective zone reaches the degenerate core, which increases the flow of energy through the envelope when compared to the case of a pure radiative transport.

White dwarfs with low temperatures, typically lower than 10 000 K, depending on the mass, experience the phenomenon of crystallization. With the cooling of the star, the ions, which are completely decoupled from the electrons, start to lose their kinetic energy,

initiating a series of phase transitions. During the crystallization process, the cooling rate of the star goes down in response to the release of a new energy source, the latent heat. This is the last energy source of a white dwarf. When it is over the white dwarf will cool until it disappears as a black dwarf, on a timescale much larger than the present Hubble time

The core of white dwarfs with masses in the range 0.4-1.05 $M_\odot$ should be composed of carbon and oxygen (C/O). In contrast, the progenitors of white dwarfs with masses higher than ≈1.05 $M_\odot$ probably reach stable carbon-burning, producing an oxygen/neon (O/Ne) or neon/oxygen/magnesium (Ne/O/Mg) core [13, 15, 16]. The determination of the mass range for each type of core composition still is an open question. Recently, Althaus et al. 2020[18] showed that ultra-massive white dwarf stars ($M > 1M_\odot$) could be formed with carbon-oxygen cores if the rotation of the degenerate core after the helium-burning is implemented together with a reduced mass-loss rate in the AGB stage. They reported that the characteristic of an ultra-massive WD with a C/O resulted from a single star evolution is markedly different from those with O/Ne, and from those with C/O core that might result of a double degenerate merger. In summary, determining the values of these limits is critical to improve our understanding of the population of massive and ultra-massive white dwarfs.

The stellar evolution theory usually predicts the formation of white dwarfs with pure hydrogen atmospheres. However, there are some events like *very late thermal pulse* (VLTP) and also *late thermal pulse* (LTP) that can form H-deficient white dwarfs. The VLTP happens during the Born-Again episode [19, 20, 21, 22, 23], in which a helium flash occurs in the cooling track of the white dwarfs, forcing the star to evolve back to the AGB stage. As a result, the VLTP burn a great part of the hydrogen left in the envelope of the star. While in Late Thermal Pulse (LTP), the star experience an intense helium-shell pulse that occurs just following AGB departure and causes a rapid looping evolution between the AGB and PN phases.

The composition of white dwarfs atmospheres allows us to separate them into two groups: DA and non-DA. The DA spectral type shows a hydrogen-dominated atmosphere typically with $M_H = 10^{-4}M_\odot$, but it depends on the white dwarf mass. This class represents the majority of white dwarf stars, to be precise 80% of them [24]. The remaining $\sim$ 20% are non-DA, which includes all the white dwarfs that do not have hydrogen as the main element of the atmosphere. The non-DA white dwarf are composed of the spectral types DO, DB, DQ, DZ, and DC (see Althaus et al. 2010 [25] for further details), depending on the element present in their atmospheres.

The use of white dwarfs models combined to observational data can be a powerfool tool to have information about a variety of topics in modern astrophysics. An important example is the Initial-to-Final mass relation (IFMR), which is a connection between the

WD and their progenitor star. The IFMR leads to constraints on the upper mass limit that separates WD progenitors of Type-II supernovae [26, 27]. Also, by the comparisons of theoretical computations with the distribution in the Color-Magnitude Diagram [28, 29] or from white dwarf luminosity function [30, 31], the age of stellar populations can be obtained. Furthermore, binaries systems with white dwarfs are believed to originate Type-Ia supernovae, when the WD accrete a mass close to the Chandrasekhar limit [32]. Lastly, the use of white dwarf models can enhance the comprehension of the physics in extreme regimes [33, 34]. Most of white dwarfs cross at least one stage of pulsational instability during their lives,[3] turning them into multi-periodic pulsating variable, which allows us to analyze their internal structure employing the tools of asteroseismology [35, 36, 37, 25, 2, 24].

1.3 Stellar Pulsations

The pulsations are a natural well known phenomenon on Earth, manifesting in a variety of forms and environments. Some examples are the waves on the surface of the oceans produced by the action of gravity, or also as the sound waves produced by pressure gradients. The physical principles responsible for the characteristics of the pulsations are the same in stars: conservation of mass, energy, and momentum.

In a simple approximation, the structure of a star can be described as a self-gravitating sphere of gas. This sphere is thought to be in equilibrium, which means that the gradient pressure balances the gravitational force. Besides that, many processes can occur inside the star which can disturb this equilibrium. These processes can have their origin in changes in the radius of the star, in the surface temperature, in the area, or in the orientation of the stellar surface, or a combination of all of these effects. Some of these perturbations can reach amplitudes high enough to become visible on the surface of the star, becoming observable as periodic variations in the luminosity. When it happens the star becomes a pulsating star.

Stellar pulsations are a common phenomenon, with pulsating stars present at all the stages of stellar evolution. Figure 3 shows a HR diagram with all the instabillity strips. We can see that the variable stars are numerous, spanning over a large range of masses, spectral types, evolutionary stages, with distinct excitation mechanisms [1].

The pulsation in stars can be categorized in two oscillation types: radial and nonradial. In the radial pulsations, the luminosity variations are due to changes in the volume of the star, which keeps its spherical symmetry. Radial oscillations are acoustic waves, where the restoring force is the pressure, the p-modes. On the other hand, in nonradial pulsations, the star comes out of its equilibrium state without preserving spherical

[3] An exception are the high-field magnetic white dwarfs, that represents a fraction of the local population and there is no observational evidence of variability due pulsations

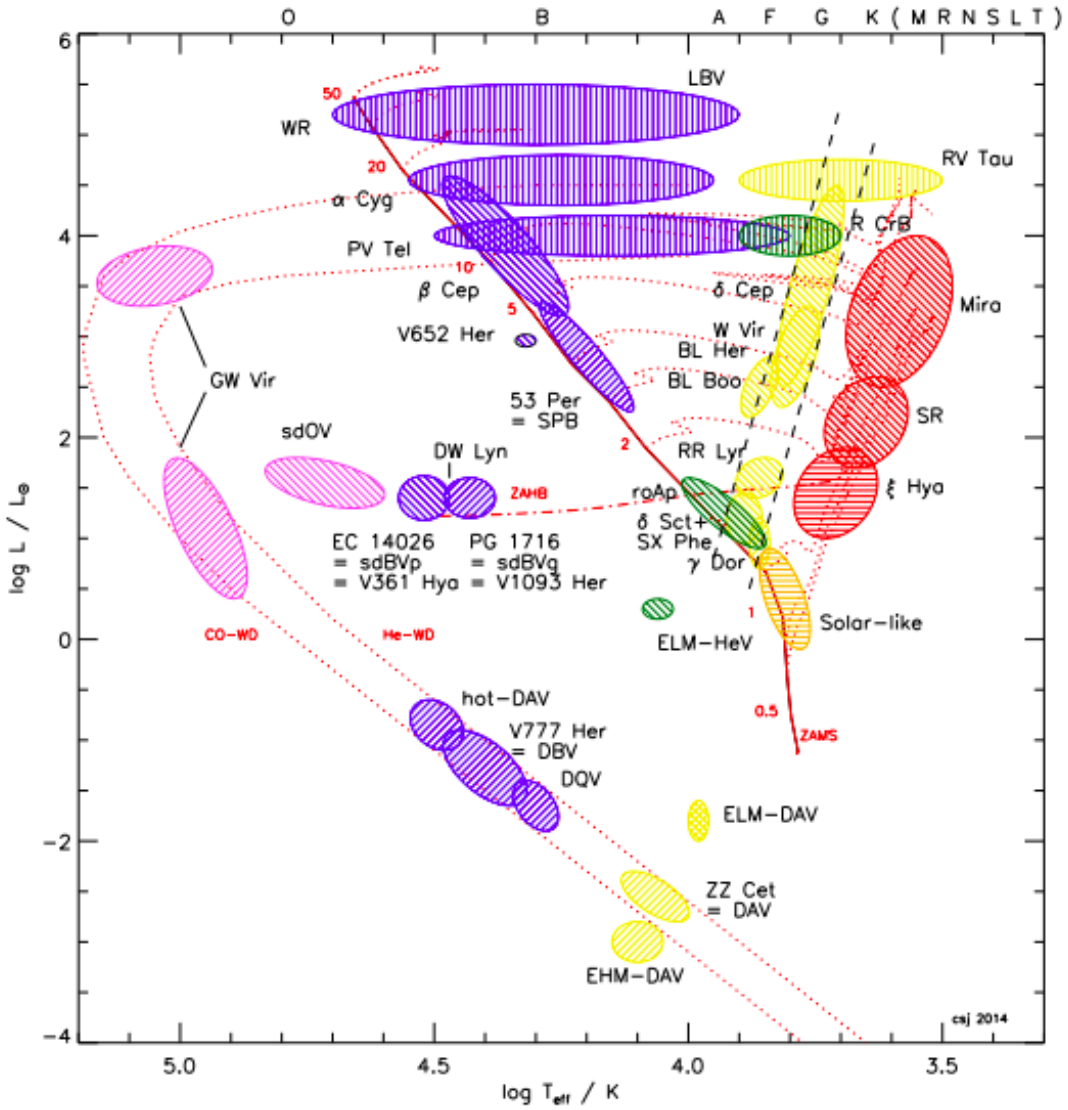

Figure 3 – Approximate locations of major pulsating variables colored roughly by spectral type in the Luminosity-effective temperature diagram (or Hertzsprung Russell diagram). Shadings represent opacity driven p-modes (\ \ \), g-modes (///), strange modes (|||), and acoustically-driven modes (≡). Approximate spectral types are indicated on the top axis. Extracted from Jeffery & Saio 2016 [1].

symmetry. The stellar material displaces in the radial and the horizontal direction, with the pressure and the also the gravity acting as the restoring forces. Notwithstanding, whereas the radial pulsations show an acoustic mode spectrum, the nonradial pulsations can also show a gravity mode spectrum, the g-modes [38].

In the Figure 3, the color represents roughly the spectral type, and the shading represents the excitation mechanisms: opacity-driven p-modes (\ \ \), g-modes (///), strange modes (|||), and acoustically-driven modes (≡). Still, it is possible to classify these stars according to the type of pulsation they experience. In the radial group are the "classical pulsating stars" like the Cefeidas type II, RR Lyrae, and the Miras. The stars

that composed the nonradial pulsations group are the β Cep, γ Dor, GW Vir, and the ZZ Ceti [4].

1.3.1 Nonradial pulsations

The objects studied in this work exhibit nonradial pulsations, which are described by hydrodynamics[5] through the equations for conservation of mass (eq 1.3), momentum (eq 1.4), and energy (eq 1.5):

$$\frac{\partial \rho}{\partial t} + \nabla.(\rho \vec{u}) = 0 \quad , \tag{1.3}$$

$$\rho \left(\frac{\partial}{\partial t} + \nabla.\vec{u} \right) \vec{u} = \rho \vec{f} - \nabla P - \rho \nabla \Phi + \nabla \Theta \quad \text{and} \tag{1.4}$$

$$\rho T \left(\frac{\partial}{\partial t} + \nabla.\bar{u} \right) S = \rho(\epsilon_N + \epsilon_V) - \nabla.\vec{F}_R \quad . \tag{1.5}$$

where ρ is the density, P is the pressure, T the temperature, $\vec{u}$ is the flux velocity, S is the specific entropy, Φ the gravitational potential, $\vec{f}$ the external electromagnetic forces, Θ the viscosity tensor, ϵ_N nuclear energy generation rate, ϵ_V generation of heat by viscosity, $\vec{F_R}$ the radiation energy flux, and ∇ is the gradient operator.

In order to model the pulsations, small perturbations are applied to a system in equilibrium that has spherical symmetry. a system of linearized equations is obtained, assuming first order perturbations. Thus, we can describe the variables according to the following equation:

$$f'(r, \theta, \phi, t) = f'_{k,\ell,m}(r)\, Y_\ell^m(\theta, \phi)\, e^{(i\sigma_{k,\ell,m}t)} \quad , \tag{1.6}$$

here f' represents an Eulerian perturbation of a physical parameter f, $Y_\ell^m(\theta, \phi)$ is the spherical harmonics, and $\sigma_{k,\ell,m}$ is the oscillation frequency. The function $f'_{k,\ell,m}(r)$ describes the radial part of the perturbation while $Y_\ell^m(\theta, \phi)$ and $e^{(i\sigma_{k,\ell,m}t)}$ describe the nonradial part. The nonradial oscillations problem needs to be solved numerically. In the adiabatic approximation (dS=0), the linearized nonradial pulsations problem becomes a fourth-order eigenvalue problem. Once it is solved, the eigenfunctions with their correspondent eigenvalues ($\sigma_{k,\ell,m}$) become available.

According to equation 1.6, each mode is described by three parameters: the radial order k, the harmonic degree ℓ, and the azimuthal order m. These parameters indicate the number of nodes and nodal lines, which are imaginary lines that separate the the star in

[4] The EHM-DAV are the massive ZZ Ceti stars and it cannot be in the place where they are puted in Figure 3. Therefore, this pulsation subclass should be disregarded.

[5] For further details it is recommended to consult the works of Cox (1980) [39] and Unno et al. (1989) [40]

sectors. Geometrically, k = 0, 1, 2 .. is the number of nodes in the radial component of the function, $\ell = 0, 1, 2$ .. is the number of nodal lines in the stellar surface, and $m = -\ell, .., 0, .., \ell$ is the number of nodal lines longitudinally. The harmonic degree indicates the number of nodal lines in the star surface, where $|m|$ correspond to meridians and $\ell - |m|$ are parallels. The modes are known as spheroidal modes [40].

Figure 4 depicts the nodal pattern over a stellar surface of the spherical harmonics according to certain values of ℓ and m. Two particular cases are observed: when ℓ=$|m|$, and $m = 0$. In the first one, the nodal lines are all meridians, while in the second, all lines are parallels. When m=ℓ=0, the oscillation is radial and the spherical symmetry is conserved.

In the nonradial oscillation, some regions of the stellar surface become more brilliant and other ones dimmer, with these regions becoming smaller as the value of ℓ increases. What we observe is a luminosity variation due to the combination of these regions. Therefore, modes with $\ell \geq 3$ are too hard to observe in white dwarf stars because the surfaced averaged variations are very small. This phenomenon is known as *geometric cancellation*, which occurs when the regions of opposite brightness are too small for a variation in luminosity to be detected.

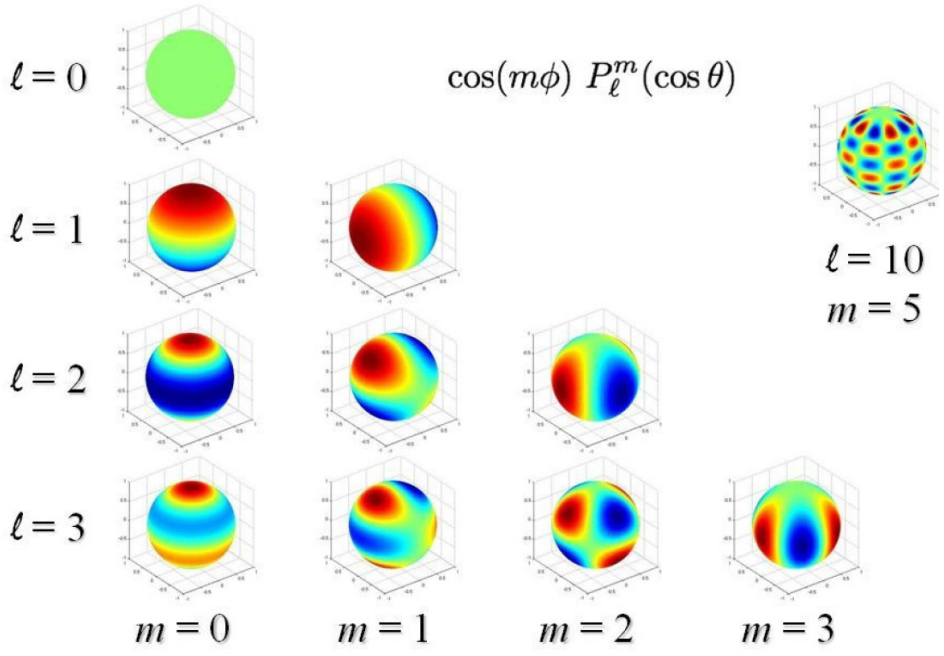

Figure 4 – Representation of the real part of the spherical harmonics $Y_\ell^m(\theta, \phi)$. Extracted from Romero (2012) - PhD. Thesis Universidad De Buenos Aires, Facultad de Ciencias Exactas y Naturales

In models where magnetic fields and rotation are not considered, the pulsation equations become independent of the azimuthal order m, because the spherical symmetry is conserved. It means that the eigenfrequencies σ will be degenerate, with each frequency

splitted into $2\ell + 1$ components. Therefore, for each certain value of k and ℓ it will exist $2\ell + 1$ normal modes characterized by the same frequency of oscillation.

1.3.2 Spheroidal modes

The spheroidal modes are classified according to the restoring force, being called p-modes when this force is the pressure gradient and g-modes when it is the gravity. The properties of these two types of modes are ruled by two characteristic frequencies: N and L_ℓ.

The g-modes are in the domain of the low frequencies (long periods), becoming lower (longer) as the values of ℓ and k increase. Their period spectrum is ruled by the Brunt-Väisälä (N) frequency, which can be written as:

$$N^2 = \mathrm{g}\left(\frac{1}{\Gamma_1}\frac{\mathrm{dlnp}}{\mathrm{dr}} - \frac{\mathrm{dln}\rho}{\mathrm{dr}}\right) \quad , \tag{1.7}$$

with g being the local gravitational acceleration, Γ_1 the adiabatic exponent, p the pressure, and ρ the density. In particular, N provides the difference between real and adiabatic density gradients. When N^2 is positive, then N is the oscillation frequency of a convective bubble around its equilibrium position [40]. In white dwarf stars, the Brunt-Väisälä frequency assumes lower values in the center due to the degenerate core.

On the other hand, the p-modes are in the high frequencies (short periods) regime, and are characterized by displacement of the material essentially in the radial direction. The period spectrum is ruled by the Lamb frequency, which can be written as:

$$\mathrm{L}_\ell^2 = \frac{(\ell+1)\mathrm{l}}{\mathrm{r}^2}\,\mathrm{c_s^2} \quad , \tag{1.8}$$

where c_s^2 is the adiabatic local sound velocity $c_s = \sqrt{\Gamma_1 p/\rho}$. The Lamb frequency is inversely proportional to the time that takes a sound wave to travel a distance $\lambda_\ell = 2\pi r/\ell$ [40].

Considering the Cowling approximation [38], where $\Phi = 0$ (Φ is the gravitational potential), the coefficients in the equations varies slowly in comparison with the eigenfunctions. Then, if we assume a radial dependency of the displacements in the form $\mathrm{e}^{\mathrm{ik_r,r}}$, where $\mathrm{k_r}$ is the radial wavenumber, we can write a dispersion relation in the following way:

$$\mathrm{k_r} = \frac{1}{\sigma^2 \mathrm{c_s^2}}(\sigma^2 - \mathrm{L}_\ell^2)(\sigma^2 - N^2) \quad . \tag{1.9}$$

The equation 1.9 is the dispersion relation, which relates the wavenumber to the frequency. The appearance of the Lamb frequency and Brunt-Väisälä frequency as critical

frequencies should be noted. For a mode to be able to propagate, k_r necessary needs to be positive, which occurs when:

$$\sigma^2 > L_\ell^2, N^2 \quad , \tag{1.10}$$

and

$$\sigma^2 < N^2, L_\ell^2 \quad . \tag{1.11}$$

These inequations define the regions where waves can propagate inside the star. The solution 1.10 represents the p-modes, where the radial displacements are dominant. These oscillations have a timescale of a few seconds in the white dwarfs, making them to be very hard to be observed. To the date of this dissertation, no p-mode was observed in a white dwarf star. On the other hand, the solutions given by the inequation 1.11 represent the g-modes, which have a scale time of hundreds of seconds or more. In these modes there are predominant horizontal motions across equipotential surfaces of gravity, which is energetically more favorable to excite the pulsation modes to observable amplitudes. If these inequations are not satisfied, k_r is a pure imaginary number and the solutions are evanescent. Due to this,the stellar interior is divided into propagation zones and evanescent zone, determined by the characteristic frequency profiles.

Figure 5 shows the propagation diagram[6] for a subdwarf B model (or sdB), with $M_\star = 0.473 M_\odot$ and $T_{\rm eff} = 28\,700$K. The quantity ω^2 denotes the square of dimensionless frequency [$\omega^2 = \sigma^2/(GM/R^3)$] and is plotted as function of the radial coordinate $-\log(1 - M_r/M_\star)$. It shows the $\log(N^2)$, the $\log(L_\ell^2)$, and with dotted horizontal lines the oscillation frequencies of several modes, along with the nodes of the correspondent radial eigenfunction. The region between the Brunt-Väisälä and the Lamb frequencies is the evanescent region (gray shaded), where the modes do not propagate. The region above $\log(N^2)$ is the high-frequency domain, where the p-modes do propagate. The region below the $\log(L_1^2)$ is where the g-modes do propagate, in the low-frequency domain. In realistic stellar models, the characteristic frequencies have a dependence on the position. Indeed, it is possible to see bumps in the Lamb and Brunt-Väisälä frequencies profile in Figure 5. It will be shown later that these 'bumps' are associated with changes in the chemical composition of the models due to the presence of chemical interfaces.

1.4 Pulsating white dwarfs

During their evolution, white dwarf stars cross some instability strips manifesting nonradial pulsations. When it happens, brightness variations can be detected from these stars. Each one of these pulsating white dwarfs will present a characteristic period spectrum

[6] see Cox 1980 [39]; Unno et al. 1989 [40] for further details

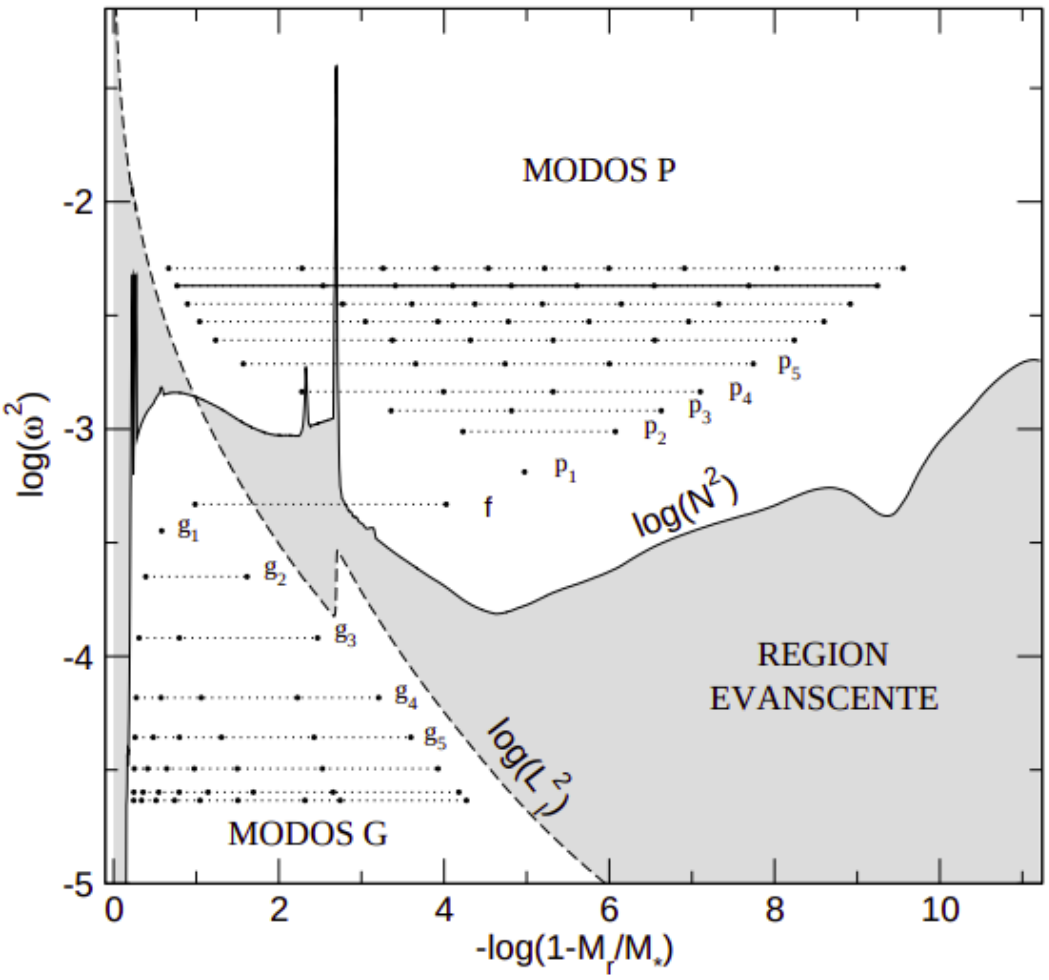

Figure 5 – Propagation diagram of a sdB star with $M_\star = 0.473 M_\odot$ and $T_{\rm eff} = 28\,700$K for modes with $\ell = 1$. The shaded-gray region is the evanescent zone where the modes do not propagate, whereas white zones are propagation zones. The logarithm of the Brunt-Väisälä and the Lamb frequencies are depicted with filled and dashed lines, respectively. The horizontal lines show the squared eigenfrequencies, whereas the black dots are the nodes of the radial eigenfunction. Extracted from Romero (2012) - PhD. Thesis

and we can classify them according to their effective temperature and surface gravities. The white dwarfs that show periodic variabilities can be classified into the following groups[7]:

1. **PG1159/PNNVs/DOVs**: these objects are pre-white dwarfs with hydrogen deficient envelopes, but rich in C/O/He. Their effective temperature and surface gravity are around $80\,000\text{K} \leq T_{\rm eff} \leq 180\,000\text{K}$ and $5.5 \leq \log(g) \leq 7.5$, respectively. Some of the stars in this class are surrounded by a planetary nebula and are called PNNVs, while those that do not are called DOVs;

[7] For further details about the evolutionary and pulsating properties of the white dwarf stars, it is recommended to consult the works of Winget & Kepler (2008) [36], Fontaine & Brassard (2008) [37], Córsico et al. (2019) [24] and Aerts (2021) [41].

2. **DBVs or V777 Her**: this class is composed of helium-rich white dwarfs with 22 000K $\leq T_{eff} \leq$ 31 000K and 7.6 $\leq \log(g) \leq$ 8.2;

3. **DQs**: white dwarfs stars with the presence of C and He in their envelopes, with 19 000K $\leq T_{eff} \leq$ 22 000K;

4. **DAVs or ZZ Ceti**: composed of white dwarfs with hydrogen envelopes. Their effective temperature and log(g) spans over 14 000K $\leq T_{eff} \leq$ 10 500K and 7.8 $\leq \log(g) \leq$ 9, respectively;

5. **GW Lib**: accreting pulsating WDs in cataclysmic variables. Their atmospheres are H-dominated, but due to accretion from a solar composition or He-enriched low mass companion, they can have an enhanced He abundance. Their temperature and surface gravities are around 16 000K $\leq T_{eff} \leq$ 10 500K and 8.3 $\leq \log(g) \leq$ 8.7. The first object of this class was named GW Librae, discovered by Warner and van Zyl (1998) [42];

6. **ELMVs**: extremely low-mass WDs variables with 10 000K $\leq T_{eff} \leq$ 7 800K and 6 $\leq \log(g) \leq$ 6.8.

7. **pre-ELMVs**: probable the precursors of the ELMVs [43]. Their effective temperature and surface gravity are usually around 13 000K $\leq T_{eff} \leq$ 8 000K and 4 $\leq \log(g) \leq$ 5;

8. **hot DAVs**: these objects were predicted theoretically by Shibahashi et al. (2005, 2007) [44, 45], which found that g modes should be excited in DA stars at high temperatures ($T_{eff} \geq$ 30 000 K) and with very thin hydrogen envelopes, about $10^{-14} M_{\odot}$.

1.5 The ZZ Ceti or DAV stars

ZZ Ceti stars where the first pulsating white dwarfs to be discovered [46], and they are currently the most numerous, with approximately ∼300 objects detected [24, 47, 48]. These stars have their atmospheres composed of hydrogen, have effective temperature in the range 10 500K $\geq T_{eff} \geq$ 14 000K, and have superficial gravity 7.8 $\leq \log(g) \leq$ 9. They pulsate in low harmonic degree ($\ell \leq 2$) g-modes, with periods usually between 100 - 2 000 s.

The ZZ Ceti can be separated into two groups [49, 50]. The first one is composed of the stars at the hot edge (high temperatures) of the instability strip. Stars in this group usually exhibits only a few modes characterized by short periods, less than 350 s, and amplitudes around 1.5 to 20 mma. They present a light curve that is stable over decades, with sinusoidal pulse shapes. In opposition, the ZZ Cetis at the red edge (lower temperatures) of the instability strip show several long periods (up to 1000 s) usually with high amplitudes (40-110 mma). The pulsation spectra of ZZ Cetis at red edge can

suddenly change due to amplitude variation. It can cause the appearance of harmonics and combination of frequencies, making the light curve of these objects more complex.

There are strong observational evidences indicating that the ZZ Ceti instability strip is pure, i.e., all DA white dwarfs that are inside the instability strip will pulsate. The observational determination of the instability strip is directly related to two factors: the sensibility and precision of the light curves, and also the precision of the determinations of parameters like the log(g) and the effective temperature.

1.6 Asteroseismology of ZZ Ceti stars

The analysis of the pulsation spectrum and the amplitudes of a variety of stars has led to the development of several techniques which, taken together, are known as *asteroseismology*. These techniques exploit the comparison between observed periods and the periods computed using theoretical stellar models. It is based on the hypothesis that each pulsation mode propagates in a particular zone in the stellar interior, the one in which the mode oscillates with higher amplitude. Thus, each mode carries information about a specific part of the star. The crucial point for a successful use of asteroseismology is not the absolute number of observed modes itself, but the heterogeneity of the eigenfunctions of the modes. Therefore, the information provided by a few periods corresponding to low-order modes is, in general, richer than the information provided by a larger set of high-order modes, which are close to the asymptotic regime.

Asteroseismology applied to white dwarf stars is a very powerful technique that allows us to determine with good precision the stellar mass, the thickness of the outer envelope, magnetic fields, rotation rates, cooling rates, and more. Using the pulsation periods through asteroseismology, allows us to constrain the value of the $C(\alpha,\gamma)O$ cross-section [51], which cannot be measured in any terrestrial laboratory. Pulsating white dwarfs are valuables laboratories to study the physics at extreme conditions: crystallization [52, 53, 54], neutrino cooling [55], axion emission [56, 57, 34, 58] and also important properties about the convection zone in the envelope of the star [59, 60]. Finally, asteroseismology in pulsating white dwarfs can be used to obtain the rotation period, the presence and the magnitude of magnetic fields, the asteroseismological distance, and many more applications.

Is possible to mention the important work of Tassoul et al. (1990) [61], in the early days of asteroseismology of ZZ Ceti stars, which presented a model grid of DA and also DB (He-rich) stars. These models were by many years the reference models in white dwarf asteroseismology, being explored in the important works of Brassard et al. (1991, 1992ab) [62, 63, 64]. However, some models had some inconsistencies like a pure carbon core, whereas the evolutionary computations predict a mix of carbon and oxygen depending on the stellar mass. Another inconsistency is that the chemical interfaces were modeled

considering diffusive equilibrium. This produces abrupt changes in the chemical profile, that translates into unreal bumps in the Brunt-Väisälä frequency [65, 66].

A significant improvement in the white dwarf models was introduced by the group of Stellar Evolution and Pulsations of La Plata [67, 68]. They presented models considering time-dependent diffusion, which includes gravitational settling and chemical diffusion. The core chemical profile was extracted from the evolutionary tracks of Salaris et al. (1997) [69], appropriately scaled according to the stellar mass. However, despite representing great progress, those models were not fully evolutionary, coming from artificially initial models not consistent with white dwarf previous evolutionary stages.

Years later, Castanheira & Kepler (2008, 2009) [70, 71] carried out an asteroseismological study of a sample composed of 87 ZZ Ceti stars, which at that time represented almost all know ZZ Cetis. To this end, they used artificial initial models, with a core composed of 50% of carbon and 50% oxygen, and with the He/H interface modeled following the predictions of time-dependent diffusion. The most important result of these works was the evidence of the existence of a range of hydrogen envelope mass ($10^{-4} \geq M_H/M_\star \geq 10^{-10}$), suggesting that there is also a group of DA white dwarfs with thinner hydrogen envelopes. In the same year of the work of Castanheira & Keppler, Bischoff-Kim et al. (2008) [57] presented an asteroseismological study of the ZZ Ceti stars G117-B15A and R 548, using parametrized models similar of those used in Castanheira & Kepler (2008, 2009), but with core chemical profiles extracted from evolutionary computations of Salaris et al. (1997).

In the past few years, the use of fully evolutionary models have become more important. Therefore, it is possible to use two approaches for white dwarf asteroseismology. The first one uses static models in which it is possible to parametrize the chemical profiles to explore a large variety of combinations [72, 73, 74]. The other one uses evolutionary models that result from the computation of the complete evolution of the progenitor stars [75, 76, 47, 77]. The chemical profiles of the white dwarf models, in this case, are consistent with the previous evolution, a feature that is important to correctly assess the pulsation periods and also the mode-trapping properties of the ZZ Ceti stars [24]. In addition, an analysis of the impact of the uncertainties from the evolutionary history of progenitor stars in the pulsational properties of the white dwarf models was presented by De Geronimo et al. (2017) [78], adding confidence in the use of evolutionary models as a robust asteroseismological approach.

The first asteroseismological study using complete evolutionary models was presented by Romero et al. (2012) [75]. The authors presented an asteroseismological study for 44 ZZ Ceti stars in the mass range 0.42-0.81 $M_\odot$, which include the G117-B15A, one of the most studied ZZ Ceti [79, 80, 81, 82, 83]. They used a grid of evolutionary models characterized by consistent chemical profiles and covering a wide range of stellar masses, thicknesses of the hydrogen envelope, and effective temperatures. One of their results, in

agreement with Castanheira & Kepler (2008, 2009), was the existence of DA white dwarfs with less hydrogen in their envelopes than predicted by the previous evolution.

The study was continued in Romero et al. (2013) [76], where the authors analyzed the massive branch of the ZZ Ceti stars, with 42 objects in the mass range of 0.72 - 1.05$M_{\odot}$. To this end, they extended the model grid towards the high mass domain. They found that the phase diagram presented in Horowitz et al. (2010) [84] seemed to be a good representation of the crystallization process inside white dwarf stars. Another important report was the discrepancies between the determination of mass from spectroscopy and asteroseismology. The treatment of convective energy transport, which is encompassed in the mixing-length theory in one-dimensional models, was quoted as a possible explanation.

Tremblay et al. (2013) [85] presented a grid of mean three-dimensional spectra for pure-hydrogen white dwarfs based on 3D model atmospheres. The authors applied the grid to the well-studied spectroscopic data sets from the SDSS and the White Dwarf Catalog, where they found that the so-called high-log(g) problem was not present. Therefore, the shortcomings in the 1D mixing length theory was in fact producing the high-log(g) problem. Regardless of the employing of 3D model atmospheres, Tremblay et al. (2019) [86] reported a slight residual high-mass problem in their analysis, showing that this problem is not fully accounted for by 3D log(g) corrections. It was confirmed in the seismological analysis of Romero et al. (2019) [2], where the authors reported the largest discrepancy between spectroscopy and seismology for stellar masses above $\sim 0.75 M_{\odot}$.

To extract the information from pulsating white dwarfs are required two ingredients: reliable observational data and representative theoretical models of those objects. In the last decades, the detection of white dwarf and also pulsating white dwarf was increased significantly due to the Sloan Digital Sky Survey (SDSS). The list has also been enlarged with the use of observations from satellites, such as those of *Kepler* spacecraft [87, 5] and TESS[8]. The main targets of TESS are planets that transit bright host stars [88], but compact pulsators as white dwarfs and sub dwarf stars are also being studied, once the 2-minute cadence photometry is available [89]. All the activities about compact pulsators are coordinated by the TESS Compact Pulsators Working Group (WG#8).

To summarize, the increasing number of ZZ Ceti being discovered in the last years make the use of representative models necessary to correctly extract the information they can provide. A problem that remains is the not-good agreement between spectroscopy and asteroseismology in the high-mass domain. These topics that remain open need to be solved, as ZZ Ceti allows us to study very important things about the stellar evolution and the evolution of our Galaxy.

[8] Transiting Exoplanet Survey Satellite

2 Objectives

Although there are fully evolutionary representative models for white dwarfs covering a wide range of hydrogen mass, these models used to date have large gaps between the values available. Due to this, I will study the properties of a sample composed of 40 massive ZZ Ceti stars by updating the grid of model used in Romero et al. (2019b), increasing their resolution.

Whereas the current grid has, for each stellar mass, ~ 7 distinct values of hydrogen mass in the range $10^{-3} \geq M_H/M_\star \geq 10^{-9}$, in this work I will update this value to ~ 16. For each stellar mass, I expanded the model grid in hydrogen envelope mass, in steps of 0.1 on a logarithmic scale for $\log(M_H/M_\star)$ from -4 to -6, and in steps of 0.5 for values below. With this grid, I expect to have a good resolution on the evaluation of the properties of massive ZZ Ceti stars as a group, especially about their hydrogen distribution.

Part of the sample has already been studied in previous works, which provides a comparison between the best-fit models obtained in this work. However, others do not have any asteroseismological work with the employment of evolutionary models, as in the case of SDSSJ181222.74+432107.6, the new massive ZZ Ceti discovered within the TESS mission (Romero et al. 2021 in preparation). With the updated grid, I expect help to improve the agreement between asteroseismological and spectroscopical determinations of log(g). I also aim to obtain information about the hydrogen content of these objects. As an example, if they have usually less hydrogen than expected by the evolutionary computations.

In closing, I expect that this grid can be used in many asteroseismology works in the future, not just assisting our understand about pulsating star, but also helping to build the blocks that form our knowledge of the Universe.

3 Methodology

The methodology used is described in the following:

- I computed evolutionary sequences for the white dwarf cooling curve in the mass range 0.498 to 1.02 $M_{\odot}$ varying the thickness of hydrogen envelope in the range 10^{-3} to $10^{-10} M_H/M_{\star}$
- With these sequences, I updated the grid of fully evolutionary carbon-oxygen core DA white dwarf models generated using LPCODE, adding ∼500 sequences for white dwarf cooling curve.
- For each stellar mass, I expanded the model grid in hydrogen envelope mass, in steps of 0.1 on a logarithmic scale for $\log(M_H/M_{\star})$ from -4 to -6, and in steps of 0.5 for values below.
- Three new cooling sequences with white dwarf masses of 0.8, 0.86 and 0.9 $M_{\odot}$ were included, in order to fill some gaps in the stellar mass present in the original grid.
- I applied this grid to a sample of 40 massive ZZ Ceti stars. For each object I perform asteroseismological fits and selected a best fit model. Some particular cases were appropriately discussed. More details about the fitting process will be given in Section 3.4.
- Finally, I study the distribution of log(g) from asteroseismology in comparison with the spectroscopy, as well as the effective temperature. I obtain the hydrogen envelope mass distribution for the sample of 40 massive ZZ Ceti stars..

3.1 Numerical Methods

3.1.1 LPCODE

The La Plata Evolutionary Code (LPCODE) computes the evolution of single stars with low and intermediate mass from the ZAMS to the white dwarfs cooling curve [90, 25, 91, 76, 92, 93]. It was written in the FORTRAN 77 language. This code was employed to study aspects of the evolution of low-mass stars [91], H-deficient white dwarfs [94, 95], the formation of horizontal branch stars [96], extremely low-mass white dwarfs [93], Blue Large-Amplitude Pulsators (BLAPs) [97], and also ultra-massive white dwarf stars [98]. For a detailed description, it is recommended to consult, besides these works,

the Ph.D. Thesis of Serenelli (2002) and also Miller Bertolami (2009). Next, the code will be briefly described.

The stellar evolution equations are based on some assumptions: the star is assumed as a sphere; the effects of rotation and magnetic fields are negligible; the evolution of the stellar structure can be described by a succession of models in hydrostatic equilibrium; the material in each layer is in local thermodynamic equilibrium and the energy transport mechanisms are the convection and some extra mixing process, like the overshooting. Taking these effects into account the equations of the stellar structure and evolution, in the lagrangian formulation, can be written as [99].

$$\frac{\partial r}{\partial m} = \frac{1}{4\pi r^2 \rho}, \tag{3.1}$$

$$\frac{\partial P}{\partial m} = -\frac{Gm}{4\pi r^4}, \tag{3.2}$$

$$\frac{\partial L}{\partial m} = \epsilon_{nuc} - \epsilon_{\nu} - c_p \frac{\partial T}{\partial t} + \frac{\delta}{\rho}\frac{\partial P}{\partial t}, \tag{3.3}$$

$$\frac{\partial T}{\partial m} = -\frac{GmT}{4\pi r^4 P}\nabla. \tag{3.4}$$

where r is the radial distance to the center of the star, L is the luminosity, T is the temperature, P is the pressure, t is the time, ϵ_{ν} is the energy loss by neutrino emission per unit of mass and time, $\epsilon_{\rm nuc}$ is the nuclear energy release per unit of mass and time, $c_{\rm P}$ is the specific heat at constant pressure per unit of mass, $\delta = \frac{\partial \ln \rho}{\partial \ln {\rm T}}$, ρ is the density, and finally, $\nabla = \frac{\partial \ln {\rm T}}{\partial \ln {\rm P}}$ is the dimensionless temperature gradient. The remaining quantities assume their usual meaning. These equations need to be solved by numerical calculations. To perform the calculations, the equations are linearized and treated discretely, in a Henyey based method. The system obtained as the result of the linearization is solved iteratively through the Newton-Raphson method. In the LPCODE there is a change in the variables, which are:

$$\xi = ln(1 - \frac{m}{M_{\star}}); \tag{3.5}$$

$$\theta = ln(T/T_0) \qquad T_0 \equiv 10^6 {\rm K}; \tag{3.6}$$

$$p = ln(P/P_0) \qquad P_0 \equiv 10^{15} {\rm din/cm^2}; \tag{3.7}$$

$$x = ln(r/r_0) \qquad r_0 \equiv 10^{10} {\rm cm}; \tag{3.8}$$

$$\lambda = \frac{L}{\Delta L_0} \qquad L_0 \equiv 10^{33} {\rm erg/s}, \tag{3.9}$$

The boundary conditions are imposed upon integration of the envelope, starting in the photosphere until the interior of the model. The independent variable is now the $\xi = \ln(1 - \frac{\mathrm{m}}{\mathrm{M}_\star})$, and the dependent variables are the radius (r), the pressure (P), the luminosity (L) and the temperature (T). The linearized equations are solved iteratively, reaching the desired precision upon correction in each iteration i of the quantities obtained:

$$y_k^i = y_k^{i-1} + \delta y_k^{i-1} \quad . \tag{3.10}$$

This iterative equation is applied to the differences in physical quantities (pressure, temperature, radius, and luminosity) between the current model and the previous. In this way, the physical quantities iterated are not θ, p, x, λ, but u_θ, u_p, u_x, and u_L, that can be written as:

$$\theta^{n+1} = \theta^n + ln(1 + u_\theta) \tag{3.11}$$

$$p^{n+1} = p^n + ln(1 + u_p) \tag{3.12}$$

$$x^{n+1} = x^n + ln(1 + u_x) \tag{3.13}$$

$$L^{n+1} = L^n + u_L \tag{3.14}$$

where $u_p = \Delta P/P^n$, $u_x = \Delta r/r^n$, $u_L = \Delta L$, $u_\theta = \Delta T/T^n$ are the dependent variables in the dimensionless form, and n is the time step.

The chemical composition in LPCODE is computed by N coupled differential equations which will give the time evolution of the N chemical species present in the model. The evolution of the chemical species can be given by changes in the composition due to the nuclear burning process and mixing, like convection, diffusion, or Rayleigh-Taylor instabilities. In the LPCODE, and also in the evolutionary codes in general, the structure and chemical equations are not solved simultaneously. The equations are resolved by iteration in which, having the values of T, P, r, and L at a time $\mathrm{t_n}$, the chemical composition is computed at a given time $\mathrm{t_{n+1}}$, and so on. The simultaneous resolution of the equations is not needed because a short time step is employed, which is a requirement to use the linearized equations.

3.1.2 Physical ingredients

The radiative opacities are those from the OPAL opacity project [100] supplemented by the Alexander & Ferguson (1994) [101] molecular opacities for low temperatures. The conductive opacities are the one presented by Cassini et al. (2007) [102]. Neutrino emission rates by pair reactions, pair production by photons, and Bremsstrahlung are taken from Itoh et al. (1994) [103] and Haft et al. (1994) [104]. Throughout the white dwarf cooling sequence, the metallicity Z is defined consistently according to the predictions of chemical diffusion.

For the evolution of the chemical species, the code considers the simultaneous treatment of the processes of the instantaneous mixture and nuclear burning of the elements. The changes in the chemical abundances are governed by the following system of equations:

$$\left(\frac{d\vec{X}}{dt}\right) = \left(\frac{d\vec{X}}{dt}\right)_{\rm nuc} + \frac{\partial}{\partial M_r}\left[(4\pi\rho r^2)D\frac{\partial \vec{X}}{\partial M_r}\right], \tag{3.15}$$

where $\vec{X}$ is a vector that contains the abundances of all chemical elements considered in the computations. The first term of equation 3.15 represents the nuclear evolution that is coupled to the changes in the chemical composition due to the mixture processes, which in turn is represented by the second term of the equation. The mixture efficiency is given by the parameter D. For further details, it is recommended to consult the work of Althaus et al. (2005) [105].

Extra-mixing episodes are considered beyond each convective edge boundary, following Herwig et al. (1997) [106]. The considerations of these extra-mixing episodes are important to the chemical stratification of the white dwarfs [33, 107]. These episodes are treated as a time-dependent diffusion process in the code, assuming that mixing speeds decay exponentially with time.

The mass loss was taken into account during the central helium burning and RGB stages, following the prescription of Shröder & Cuntz (2005) [108]. In the AGB and TP-AGB stages, it is considered the prescriptions of Vassiliadis & Wood (1993) [109].

When the model reaches the cooling curve of the white dwarf stars, some extra physical ingredient needs to be taken into account. For the low-density regime it is used an updated version of the equation of state of Magni & Mazzitelli (1989) [110], whereas for the high-density regime it is used the equation of state of Segretain (1994). The high-density regime equation includes the effects of crystallization considering the contributions of the liquid and solid states [111].

The sequences presented in this dissertation are taking into account the changes in the chemical profile due to diffusion processes. The result is that the model develops a pure hydrogen envelope whose width gradually increases with the evolution during the cooling curve. Time-dependent diffusion employed in LPCODE is based on the multi-component gas treatment presented in Burgers et al. (1969) [112]. It is taken into account the gravitational settling and chemical diffusion of $^{1}\mathbf{H}$, $^{3}\mathbf{He}$, $^{4}\mathbf{He}$, $^{12}\mathbf{C}$, $^{13}\mathbf{C}$, $^{14}\mathbf{N}$, and $^{16}\mathbf{O}$ [113]. Chemical abundance changes due to residual nuclear burning are also considered in the computations. The chemical re-homogenization of the inner carbon-oxygen profile induced by Rayleigh–Taylor (RT) instabilities was also included, following Salaris et al. (1997) [69]. For the convective process the mixing-length theory, in its ML2 flavor, $\alpha = 1.0$, is adopted.

As a result of strong Coulomb interactions in their interior, cool white dwarfs are

expected to crystallize [114]. When this process occurs, two additional energy sources are considered in the computations: the release of latent heat and the release of gravitational energy, which is associated with the change of the chemical composition of the carbon-oxygen profile induced by crystallization [115, 116, 54]. This is done self-consistently and coupled with the full set of stellar evolution equations. The luminosity equation is appropriately modified to take into account the additional energy sources. To assess the oxygen enhancement in the core due to crystallization the azeotropic-type formulation of Horowitz et al. (2010) [84] was adopted.

3.2 Pulsation computations

The nonradial pulsations in the adiabatic approximation were computed with the LP-PUL, developed by Alejandro Córsico in his Ph.D. thesis [117]. The adiabatic computations are a mathematical approximation to the real non-adiabatic problem. Bradley (1998) [80] performed a study where he showed that the typical differences between adiabatic and non-adiabatic periods are from the order of 10^{-4} s. The pulsation equations are a linear four-order eigenvalue problem, which needs to be solved numerically. The resolution is made using a generalized version of the Newton-Raphson technique [118], where a solution is proposed and then iteratively improved. For detailed information about the processes, it is recommend to consult the works of Córsico and Benvenuto (2002) [65] and also the Ph.D. thesis of Córsico (2003) [117]. I computed adiabatic g-mode pulsation with harmonic degree $\ell = 1$ and $\ell = 2$ for the new sequences added to the model grid. The periods are in the 80-2000 s range, which corresponds in average to $1 \leq k \leq 50$ for $\ell = 1$, and $1 \leq k \leq 90$ for $\ell = 2$.

To compute g-modes in the white dwarfs, it is required to obtain the numerical value of the Brunt-Väisälä frequency. Following the description of Brassard et al. (1991) [62], this quantity is written as:

$$N^2 = \frac{g^2 \rho}{P} \frac{\chi_T}{\chi_\rho} (\nabla_{ad} - \nabla + B), \tag{3.16}$$

whereas χ_T and χ_ρ are:

$$\chi_T = \left(\frac{\partial ln p}{\partial ln T} \right)_\rho \qquad \chi_\rho = \left(\frac{\partial ln p}{\partial ln \rho} \right)_T, \tag{3.17}$$

and B is the Ledoux term, given by:

$$B = -\frac{1}{\chi_T} \sum_{i=1}^{n-1} \chi_{X_i} \frac{dln(X_i)}{dlnp}, \tag{3.18}$$

being X_i the abundance of atoms of species i, and n the total number of species considered. The quantity χ_{X_i} is written as:

$$\chi_{X_i} = \left(\frac{\partial ln p}{\partial ln(X_i)} \right)_{\rho,T,X_{j \neq i}}. \tag{3.19}$$

This numerical treatment of the Brunt-Väisälä frequency is called "Ledoux modified" [61], which is generalized to include variations in the nuclear species abundance most abundant in the white dwarfs interior (H, He, C, and O). The Ledoux term B is responsible for the major contribution to the Brunt-Väisälä frequency due to changes in the chemical composition. As output, the LP-PUL provide the dimensionless eigenfrequencies $\omega_{\ell,k}$, dimensionless eigenfunctions $y_1, ..., y_4$, periods $\Pi_{\ell,k}$, rotation coefficients $C_{\ell,k}$, oscillation kinetic energy $K_{\ell,k}$, and the weight functions $W_{\ell,k}$.

To consider the effects of crystallization on the pulsation spectrum of g-modes, it is adopted the "hard sphere" boundary condition, which assumes that the amplitude of the eigenfunction is abruptly reduced below the solid/liquid interface due to the non-shear modulus of the solid, as compared with the amplitude in the fluid region [119]. Therefore, our inner boundary condition is the crystallization interface that moves towards the surface with the cooling of the model and not the stellar center [52].

3.2.1 Characteristic frequencies

The Brunt-Väisälä frequency (N) is a fundamental parameter in white dwarf pulsations, characterizing the g-modes in the lower frequencies regime. It is computed using the so-called Ledoux-modified scheme, generalized to include the effects of having three different components varying in abundance [61]. This frequency is affected by each chemical transition that is presented in the chemical profile of the white dwarf model, showing peaks where these transition zones occur. The presence of these peaks modifies the theoretical period spectrum, once the Brunt–Väisälä frequency is an important quantity of the computations. Also, the Lamb frequency (L) is computed, which characterizes the p-modes in the high frequencies regime. This frequency is less dependent on the chemical transitions presented in the model.

Figure 6 shows the chemical profile (up) and the run of the Brunt-Väisälä and Lamb characteristic frequencies (low) for DA white dwarf models with $M_\star = 0.51 M_\odot$ (upper panel), $M_\star = 0.80 M_\odot$ (central panel) and $M_\star = 0.998 M_\odot$ (lower panel) at $T_{\rm eff} = 12\,000$ K and with $-\log(M_H/M_\star) \sim 6.3$. Since the Brunt-Väisälä frequency (N) [61] is proportional to the chemical gradients, it is sensitive to each chemical transition. As can be seen from Figure 6, N^2 shows bumps around the transition regions, for instance, in the core region at -log$(1 - M_r/M_\star)\approx$ 0.6-1.0, caused by steep variations in the inner C-O profile. This constitutes an important source of mode trapping in the core region [120]. Note that C-O profiles of the core for the model with $M_\star = 0.998 M_\odot$ change due to the effects of crystallization at -log$(1 - M_r/M_\star)\approx$ 0-0.2. The bump at -log$(1 - M_r/M_\star)\approx$ 3-5, for all stellar masses, is caused by the chemical transition of the He, C, and O resulting from nuclear processing in the AGB stages, and are another source of mode trapping. Once the efficiency of the chemical diffusion increases with the stellar mass, this bump is smoothed

in the $M_\star = 0.80 M_\odot$ model (central figure), and almost disappears in the $M_\star = 0.998 M_\odot$ model (lower figure). Lastly, the He/H transition region, which is responsible for the modes trapped in the outer H envelope.

3.3 The model grid

The representative DA white dwarf models used in this work are the result of fully evolutionary calculations from the ZAMS, through hydrogen and helium central burning stages, thermal instabilities, mass loss in the asymptotic giant branch (AGB), and finally through the planetary nebula domain until the models reach the white dwarf cooling curve. All the progenitor stars have initial metallicity $Z = 0.01$. This metallicity is used as a standard in the LPCODE. The initial models used for the computations of the cooling sequences are the ones presented in Romero et al. (2012, 2013, 2019b) [75, 76, 2]. In this dissertation, we only compute the cooling evolution of the white dwarfs.

In addition, I included three new sequences for the WD cooling curve with a mass of 0.82, 0.86, and 0.9 $M_\odot$. These sequences are the result of an interpolation of the chemical profiles between two evolutionary sequences. This process is performed at high effective temperatures ($\geq 90\,000$ K), in a way that any unphysical signature in the chemical profiles is washed by the chemical diffusion before the model reaches the ZZ Ceti instability strip. The values of the stellar masses of our model grid, are listed in column 1 of Table 1. The bold values are the new masses computed for this dissertation, the other masses were presented in previous works [75, 76, 2]. Are also listed the canonical (predicted by prior evolution) hydrogen mass (column 2), the helium mass (column 3), the carbon (column 4) and oxygen (column 5) central composition. In Table 1, the mass values in italics correspond to interpolated sequences.

Our parameter space expands over the following quantities: stellar mass ($M_\star$), effective temperature ($T_{\rm eff}$), and the hydrogen envelope mass ($M_{\rm H}$). The stellar mass and the effective temperature parameters are obtained consistently with what it is expected from the evolutionary calculations. For the $M_{\rm H}$, I artificially vary the thickness of the hydrogen envelope. For each sequence, with a stellar mass M and a hydrogen envelope mass $M_{\rm H}$, as predicted by the pre-white dwarf evolution, I have simply replaced ^{1}H by ^{4}He at the basis of the hydrogen envelope. This is done at temperatures above 90 000 K, in such a way that any transitory effect disappears when the model reaches the ZZ Ceti instability strip. The choice of changing the $M_{\rm H}$ is not random, once there are uncertainties related to some physical process during the pre-white dwarf previous evolution, which, consequently, causes uncertainties in the amount of hydrogen left in the envelope of white dwarf stars [75, 76, 121]. For instance, the amount of hydrogen left in the envelope of white dwarf stars is dependent on the metallicity, being thicker for models with less metallic

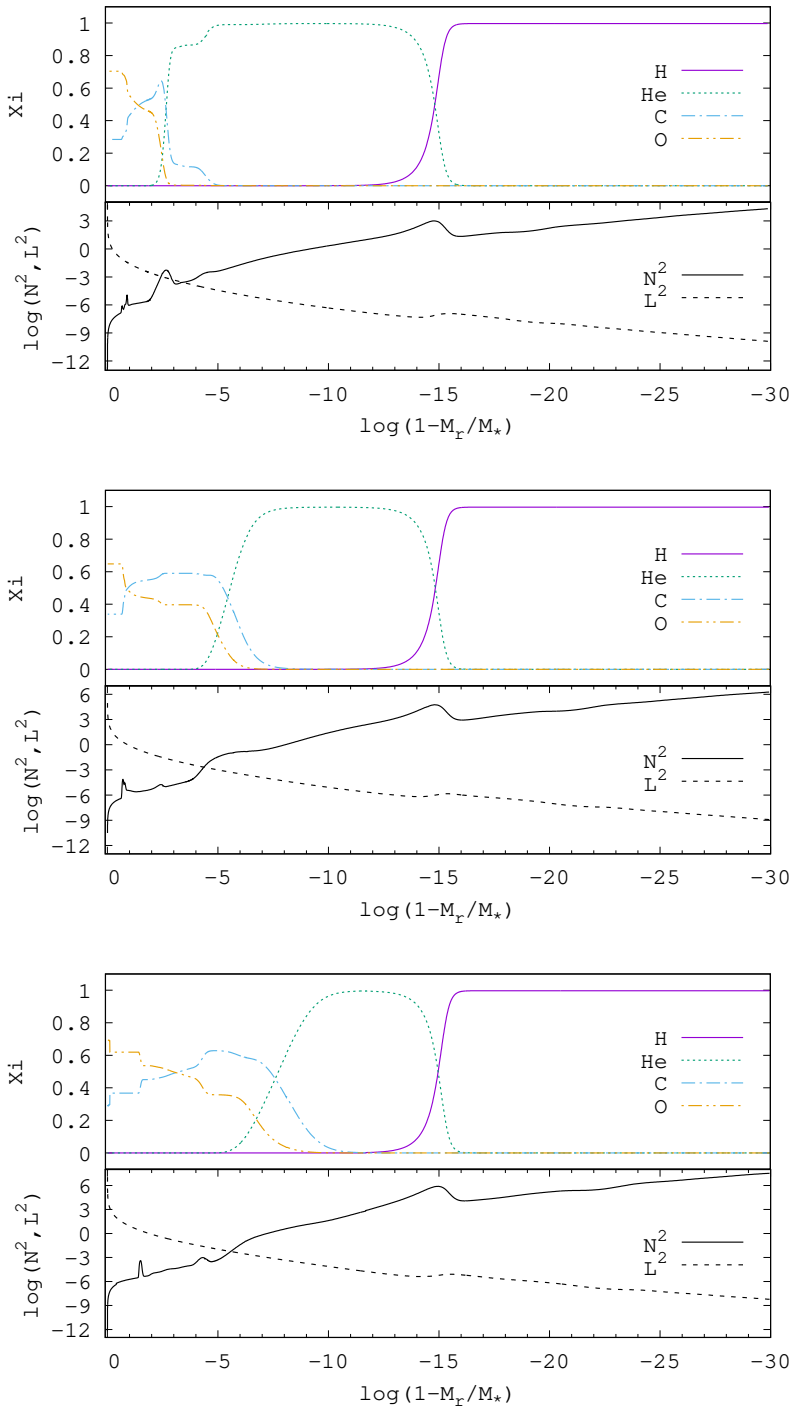

Figure 6 – Internal chemical profiles for DA white dwarfs models with $M_\star = 0.51 M_\odot$ (upper figure), $M_\star = 0.80 M_\odot$ (central figure) and $M_\star = 0.998 M_\odot$ (lower figure) for the $T_{\rm eff} = 12\,000$ K and $-\log(M_{\rm H}/M_\star) \sim 6.3$. In the lower panel of the figures it is depicted the spatial run of the logarithm of the squared Brunt-Väisälä frequency (N^2) and the logarithm of the squared Lamb frequency (L^2) for $\ell = 1$ modes for each model. Note the correspondence between the chemical transitions (upper panels of each figure) and the resulting features in the shape of the Brunt-Väisälä frequency. Note also that these features are less pronounced in the Lamb frequency.

Table 1 – The main characteristics of our set of DA white dwarf models. In column 1 are listed the stellar mass at the white dwarf stage. It is also listed the hydrogen mass at 12 000 K (column 2), the helium mass (column 3), and the central abundances of carbon (column 4) and oxygen (column 5). Sequences with mass value in italics are the result of an interpolation process of the chemical profile of two evolutionary sequences, this process is performed at high effective temperatures, typically above 90 000 K. Sequences with mass value in bold were computed for this work.

$M_\star/M_\odot$	$-\log(M_H/M_\star)$	$-\log(M_{He}/M_\star)$	X_C	X_O
0.493	3.50	1.08	0.268	0.720
0.510	3.53	1.15	0.351	0.570
0.525	3.62	1.31	0.278	0.709
0.534	3.65	1.37	0.380	0.562
0.542	3.67	1.36	0.378	0.564
0.548	3.74	1.38	0.290	0.697
0.560	3.70	1.42	0.296	0.691
0.570	3.82	1.46	0.301	0.696
0.593	3.93	1.62	0.283	0.704
0.609	4.02	1.61	0.264	0.723
0.621	4.04	1.68	0.395	0.570
0.632	4.25	1.76	0.234	0.755
0.646	4.11	1.83	0.402	0.569
0.660	4.26	1.92	0.258	0.730
0.674	4.35	1.97	0.280	0.707
0.686	4.36	2.03	0.422	0.556
0.690	4.46	2.04	0.303	0.684
0.705	4.45	2.12	0.326	0.661
0.721	4.50	2.14	0.328	0.659
0.745	4.62	2.18	0.330	0.657
0.770	4.70	2.23	0.332	0.655
0.800	4.84	2.33	0.339	0.648
0.820	4.92	2.40	0.432	0.550
0.837	5.00	2.50	0.347	0.640
0.860	5.07	2.54	0.423	0.561
0.878	5.07	2.59	0.367	0.611
0.900	5.27	2.71	0.419	0.565
0.917	5.41	2.88	0.378	0.609
0.949	5.51	2.92	0.373	0.614
0.976	5.68	2.96	0.374	0.613
0.998	5.70	3.11	0.358	0.629
1.024	5.74	3.25	0.356	0.631
1.050	5.84	2.96	0.374	0.613

progenitors. Also, Romero et al. (2020) [122] reported the detection of periodic variations on the $T_{\rm eff} = 32\,000$ K DA white dwarf HE 1017-1352, which confirms the new pulsating class of the hot DAV. These objects were predicted theoretically by Shibahashi et al. (2005, 2007) [44, 45], which found that g-modes should be excited in DA stars at high temperatures ($T_{\rm eff} \geq 30\,000$ K) and with hydrogen envelopes of about $10^{-14} M_\odot$. This is a prove of the existence of white dwarf stars with thin H-envelopes.

The hydrogen masses computed are spaced by 0.1 in logarithmic scale from the canonical value to $\log(M_H/M_\star) = -6$. Then in 0.5 until our thinner envelope with

$\log(M_H/M_\star) = -9.5$. Adding the sequences computed in this work (~ 500) to those used in Romero et al. (2019) [2], I have available a grid with ~ 800 sequences. With this updated model grid, I have on average a 2 second difference for the same mode between two models with distinct hydrogen mass at the same temperature Indeed, Kepler et al. (2012) [123] estimates that the uncertainty surrounding the physics of progenitor star evolution in the g-mode period spectrum is around 1 second. There is also the uncertainty associated with the asteroseismological fit, which needs to be taken into account. Therefore, our model grid can provide a better resolution in the asteroseismological fits.

Other structural parameters are not expected to change considerably according to evolutionary computations. Indeed, Romero et al.(2012) [75] has shown that the remaining helium left in a DA white dwarf can be slightly lower, 3 or 4 times, than what it is expected from the standard stellar evolution. This can occur only at the expense of a ~ 0.2 $M_\odot$ increase in mass of the hydrogen-free core. In addition, the structure of the carbon-oxygen core, fixed by the central helium-burning stage, is affected by the uncertainties related to the $^{12}\mathbf{C}$ $(\alpha,\gamma)^{16}\mathbf{O}$ reaction rate [78].

Figure 7 shows the model grid used in this work, with the hydrogen masses (vertical axis) calculated for each white dwarf mass (horizontal axis). The red dots are the sequences computed for this work and the black diamonds represent the models used in previous works. The thick orange line connects the maximum values of M_H for each stellar mass as predicted by our evolutionary computations (column 2 of Table 1). It is possible to see that the hydrogen mass has a strong dependence on the stellar mass, with a decrease in the amount of hydrogen envelope mass with the increase of the stellar mass.

Another phenomenon that our grid can shed light on is the 'avoided crossings', present in the g-mode period spectrum of the ZZ Ceti stars. When two modes' experiences avoided crossing, the modes exchanges their intrinsic properties [124]. We can study the avoided crossing phenomena by tracking the change in the period of a given mode with the change in the hydrogen mass. As a result, for some values of M_H, the period spacing turns to be as shorter as $\sim$8 s. Figure 8 shows the periods in terms of the hydrogen envelope thickness for modes with $\ell = 1$, for a model with $M_\star = 0.82$ $M_\odot$ at 12 000 K. It is evident that there is an increase in the periods as the hydrogen envelope becomes thinner. But this growth is not linear, and the avoided crossing becomes apparent. In particular, modes with k = 1 and 2 experience a collision at $-\log(M_H/M_\star) = 6.5$, when the modes differ by only 9 seconds.

3.4 Star sample and asteroseismological fits

In this work, I have analyzed 40 ZZ Ceti stars with spectroscopic stellar mass between 0.74 $M_\odot$ and 1.15 $M_\odot$, extracting their observed periods from the literature and

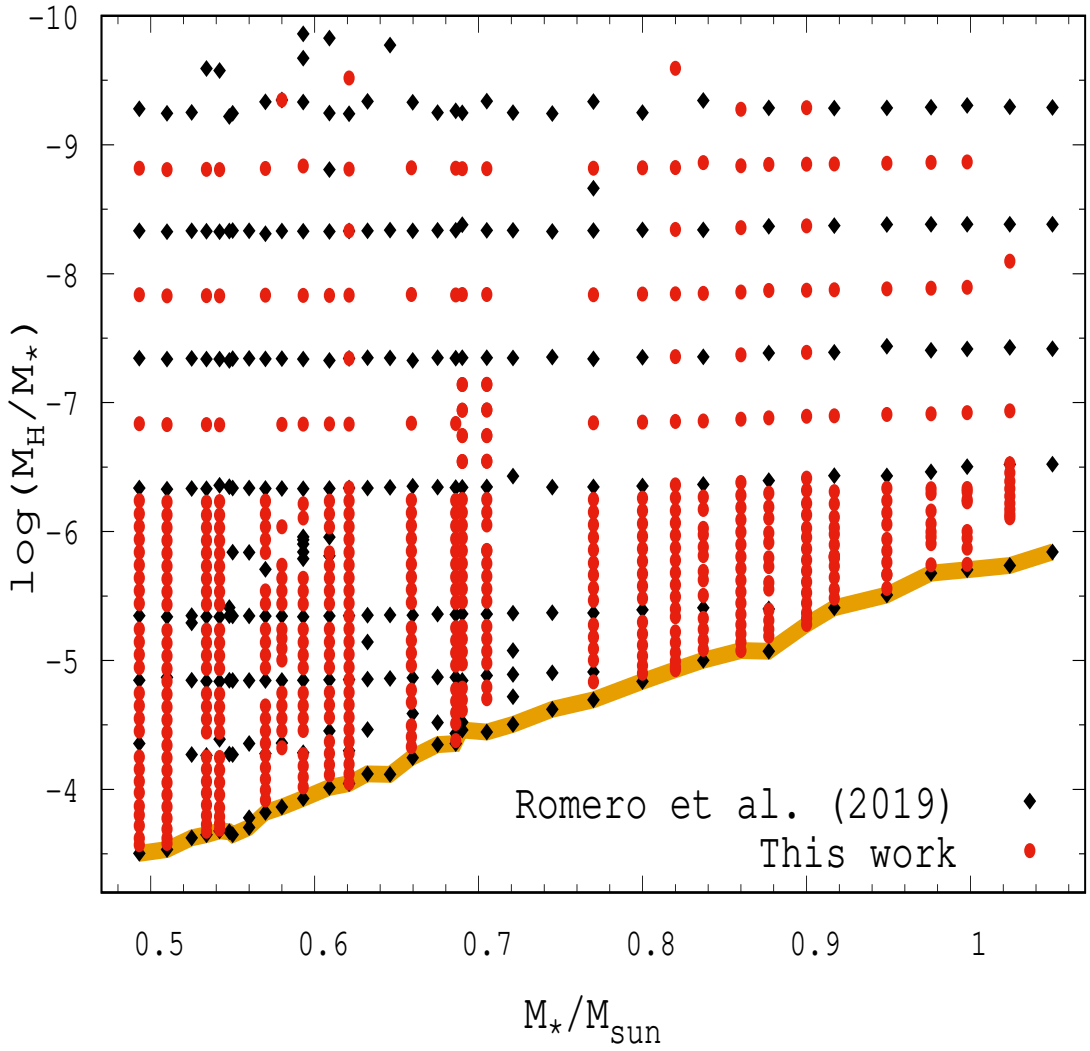

Figure 7 – Evolutionary sequences of DA WD considered in this work displaced in the $M_\star/M_\odot$ - $\log(M_H/M_\star)$ plane. Each point corresponds to a complete cooling sequence with a given stellar mass and hydrogen envelope mass. Filled red dots correspond to the evolutionary sequences computed for this work, black diamonds correspond to the sequences used in [2]. The thick orange line connects the sequences with the maximum hydrogen envelope mass predicted by our evolutionary computations. As expected, the maximum hydrogen mass decreases with the increase of the stellar mass.

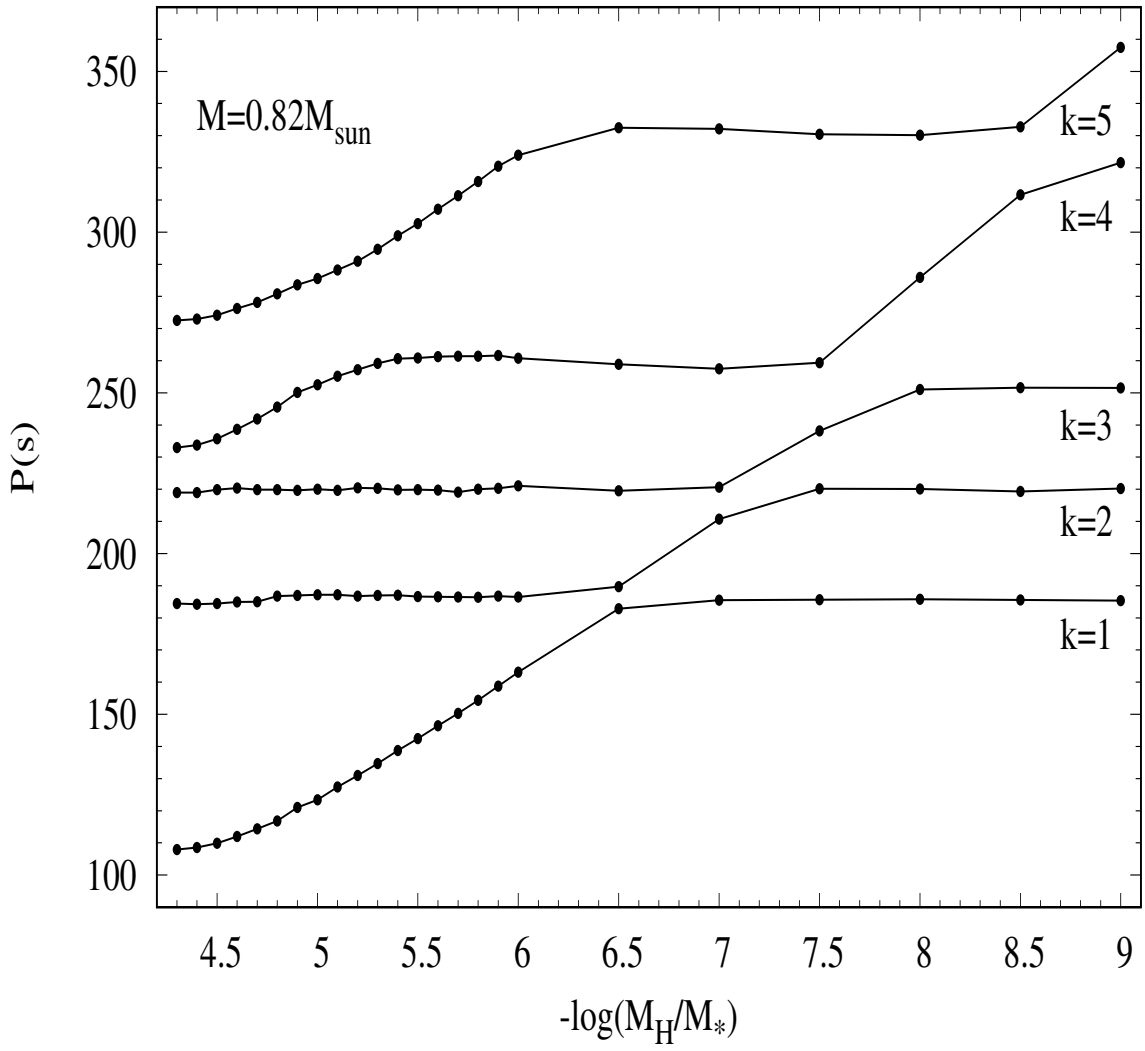

Figure 8 – Periods of the modes with $\ell = 1$ and k=1-5 in terms of the thickness of the hydrogen envelope corresponding to $M_\star = 0.82 M_\odot$ at 12 000 K. The avoid crossing can be seen in the $-\log(M_H/M_\star) = 6.5, 7, 8.5$ between the k=1 and k=2, k=2 and k=3, and k=4 and 5, respectively.

then searching for the best fit model in the model grid. These objects are listed in Table 2 (column 1) along with the effective temperature (column 2), the surface gravity (column 3), and the spectroscopic mass (column 4). The effective temperature and the log(g) values were corrected using 3D convection [85]. The stellar mass values were determined by linear interpolation of the evolutionary tracks presented by Romero et al. (2012, 2013, 2019b) [75, 76, 2] in the log(g) - $T_{\rm eff}$ diagram, using the values of the log(g) and effective temperature from Table 2.

The sample in the log(g) - $T_{\rm eff}$ plane is shown in Figure 9 as black dots, together with all ZZ Ceti known to date. The two stars with masses above 1.05 $M_\odot$, i.e. GD-518 and J0840+5222, probably do not have a C/O core according to their spectroscopic mass, and

Table 2 – Atmospheric parameters of our sample of stars corrected using 3D convection (columns 2 and 3), spectroscopic mass (column 4), and the references (column 5).

Star	T_{eff}	log(g)	$M_\star/M_\odot$	Ref.
KIC 211914185	$13\,590 \pm 380$	8.43 ± 0.06	0.87 ± 0.05	[5]
HS 1531+7436	$13\,270 \pm 250$	8.49 ± 0.04	0.90 ± 0.03	[3]
G226-29	$12\,510 \pm 250$	8.35 ± 0.04	0.81 ± 0.03	[3]*
SDSSJ005208.42-005134.7	$12\,300 \pm 427$	8.4 ± 0.1	0.9 ± 0.1	[3]
WDJ161218.08+083028.32	$12\,250 \pm 136$	8.29 ± 0.04	0.78 ± 0.04	[3]*
WDJ084021.23+522217.4	$12\,160 \pm 320$	8.93 ± 0.07	1.13 ± 0.03	[3]
G207-9	$12\,080 \pm 250$	8.37 ± 0.04	0.82 ± 0.03	[3]*
WDJ164115.61+352140.6	$12\,025 \pm 160$	8.3 ± 0.1	0.81 ± 0.09	[3]*
WDJ181222.47+432107.6	$12\,448 \pm 103$	8.49 ± 0.01	0.89 ± 0.05	[125]§
WDJ120054.55-025107.0	$11\,970 \pm 200$	8.24 ± 0.06	0.74 ± 0.05	[3]*
WDJ203857.52+771054.5	$11\,940 \pm 310$	8.38 ± 0.08	0.83 ± 0.04	[76]
WDJ215354.11-073121.9	$11\,910 \pm 200$	8.27 ± 0.06	0.77 ± 0.06	[3]
WDJ220831.39+205909.45	$11\,776 \pm 250$	8.49 ± 0.05	0.90 ± 0.04	[3]*
GD-518	$11\,760 \pm 250$	8.97 ± 0.04	1.15 ± 0.02	[3]
WDJ062159.49+252335	$11\,728 \pm 250$	8.3 ± 0.3	0.7 ± 0.3	[4]
WD 2102+233	$11\,712 \pm 310$	8.28 ± 0.05	0.77 ± 0.05	[3]
WDJ093944.89+560940.2	$11\,690 \pm 250$	8.29 ± 0.08	0.78 ± 0.07	[3]*
WDJ221458.37-002511.7	$11\,650 \pm 150$	8.30 ± 0.04	0.78 ± 0.04	[3]*
WDJ220915-091942.5	$11\,630 \pm 230$	8.30 ± 0.07	0.78 ± 0.06	[3]*
BPM37093	$11\,620 \pm 250$	8.69 ± 0.04	1.01 ± 0.02	[3]
HE 0532-5605	$11\,510 \pm 250$	8.42 ± 0.04	0.86 ± 0.03	[3]
WDJ082547.00+411900.0	$11\,510 \pm 230$	8.37 ± 0.08	0.82 ± 0.07	[3]*
WDJ125710.50+012422.9	$11\,490 \pm 250$	8.30 ± 0.09	0.78 ± 0.08	[3]*
WDJ155438.35+241032.6	$11\,470 \pm 230$	8.49 ± 0.07	0.90 ± 0.04	[3]
WDJ133714.44+010443.83	$11\,460 \pm 340$	8.6 ± 0.1	0.99 ± 0.09	[3]*
WDJ212808.49-000750.8	$11\,420 \pm 190$	8.24 ± 0.07	0.74 ± 0.04	[3]*
WDJ132350.28+010304.2	$11\,380 \pm 200$	8.45 ± 0.07	0.88 ± 0.06	[3]*
WDJ215905.52+132255.7	$11\,370 \pm 210$	8.69 ± 0.08	1.01 ± 0.05	[3]*
KUV 0159-1109	$11\,360 \pm 180$	8.29 ± 0.06	0.78 ± 0.05	[6]
WDJ103642.25+211527.9	$11\,329 \pm 250$	8.27 ± 0.03	0.76 ± 0.03	[6]
WDJ101540.14+234047.4	$11\,320 \pm 300$	8.4 ± 0.1	0.87 ± 0.04	[3]
SDSSJ030325.22-080834.9	$11\,260 \pm 220$	8.40 ± 0.08	0.84 ± 0.07	[3]*
WDJ121628.55+092246.4	$11\,240 \pm 210$	8.25 ± 0.08	0.75 ± 0.07	[3]*
WDJ092329.81+012020.0	$11\,190 \pm 160$	8.38 ± 0.06	0.83 ± 0.05	[3]*
WDJ220830.02+065448.7	$11\,147 \pm 250$	8.25 ± 0.05	0.75 ± 0.05	[3]*
WDJ171113.01+654158.3	$11\,130 \pm 70$	8.47 ± 0.03	0.89 ± 0.03	[3]*
WDJ204127.11-041724.22	$11\,114 \pm 366$	8.39 ± 0.03	0.83 ± 0.03	[6]
WDJ004154.66-030802.5	$10\,936 \pm 176$	8.36 ± 0.04	0.82 ± 0.04	[6]
WDJ165020.53+301021.2	$10\,830 \pm 110$	8.43 ± 0.06	0.86 ± 0.05	[3]*
WDJ094000.27+005207.1	$10\,590 \pm 100$	8.34 ± 0.07	0.80 ± 0.06	[3]*

Note. The values of log(g) and T_{eff} corrected by 3D convection were extracted of [24]. The values of log(g) and T_{eff} of Bognar et al. (2016) [3] white dwarf period tables were taken from the works of [126] and [127].

* Analyzed in [76]

§ Photometric determination

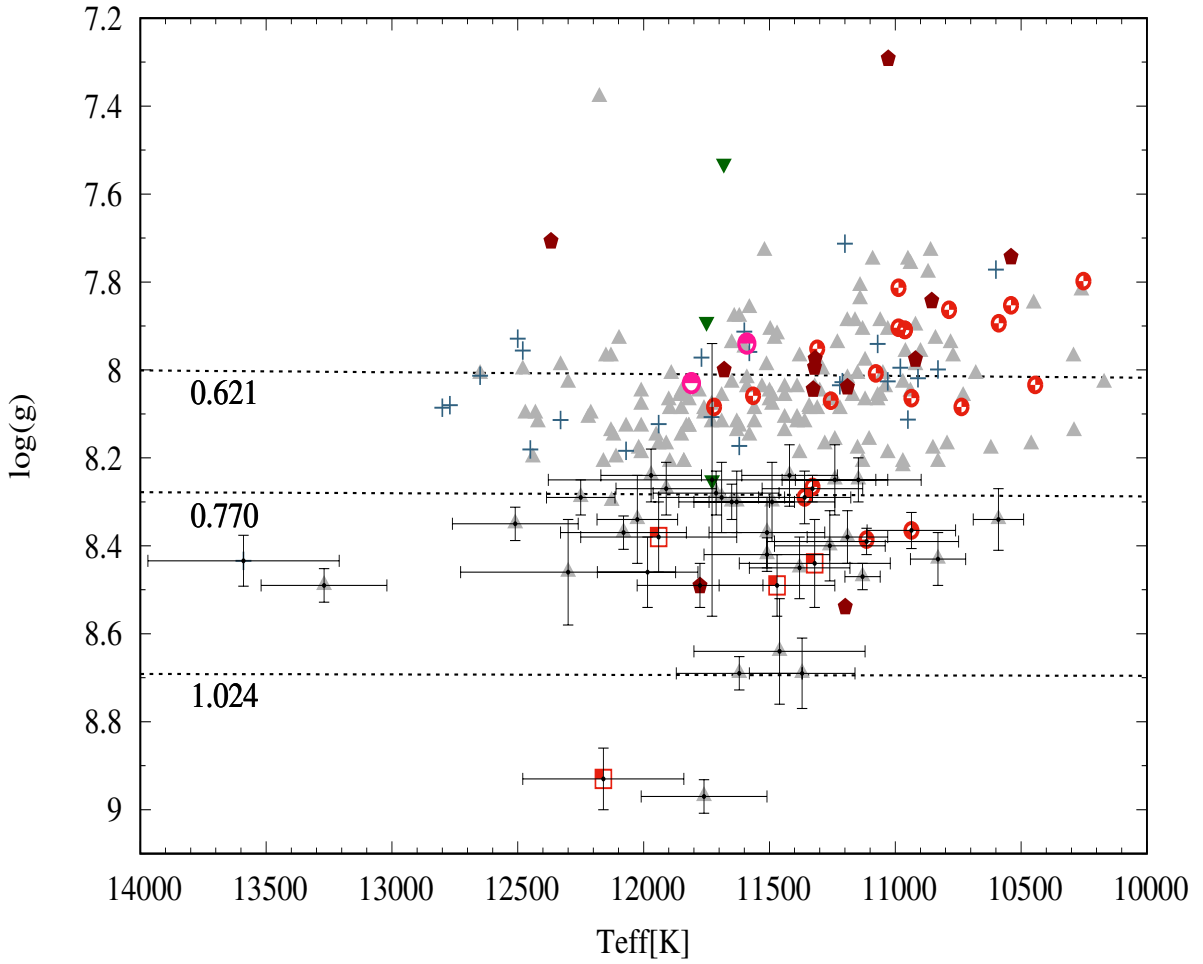

Figure 9 – ZZ Ceti stars known to date distributed in the log(g) - T_{eff} plane. They were extracted from the works of Bognar et al. (2016) [3] (grey triangle-up), Su et al. (2017) [4] (green triangle-down), Hermes et al. (2017) [5] (blue cross), Rowan et al. (2019) [6] (red semi-filled dots), Bell et al. (2017) [7] (pink up-filled dots), Fuchs (2017) [8] (dark-red pentagons), and Curd et al. (2017) [9] (red squares). The black dots with uncertainties are the objects analyzed in this work. We also include evolutionary tracks (dashed lines) with stellar masses of 0.621, 0.770 and 1.024$M_{\odot}$ from top to bottom, for guidance purposes.

are beyond the mass limit of our model grid. Nevertheless, considering the uncertainties related to the spectroscopic parameter determinations [128], and also the uncertainties in the stellar mass where the C/O core becomes an O/Ne core [13, 15, 16, 18], I decided to keep these objects in the analysis.

In the asteroseismological fits, I search for the best representative model for each of the stars presented in Table 2. To this end, I look for the theoretical model that minimizes the quality function given by Corsico et al.(2008) [129]:

$$\S^2(M_*, M_{\rm H}, T_{\rm eff}) = \frac{1}{N}\sum_{i=1}^{N} \min\left[\Pi_k^{\rm th} - \Pi_i^{\rm obs}\right]^2; \tag{3.20}$$

where N is the number of observed periods, $\Pi_k^{\rm obs}$ are the observed periods, and $\Pi_i^{\rm th}$ are

the correspondent theoretical ones. Because the period spacing between $\ell = 2$ modes is shorter than for $\ell = 1$ modes, there will always be more quadrupolar modes in a given period range. Because of that, it is easier to fit quadrupolar modes in a period interval. Therefore, I stipulate the theoretical periods to be closer to the observed periods by a factor of $N_{\ell=2}/N_{\ell=1}$, ensuring a better match between theoretical and observed periods. Note that calculating the square root of S^2, we get the standard deviation between the observed and the theoretical periods.

The effective temperature, stellar mass, and hydrogen mass of the envelope are allowed to vary in the ranges: $14\,500 \geq T_{\rm eff} \geq 9\,000$, $1.050 M_\odot \geq M_* \geq 0.686 M_\odot$, $-4.4 \geq \log(M_H/M_*) \geq -9.4$, where the values of M_H will depend on the stellar mass (see column 2 of Table 1). I also allow the stellar mass to adopt values lower than the inferior mass limit of the sample to ensure the choice of the best-fit model.

Most of the stars in the sample have data only of the discovery paper, having just a few periods detected. Thus, we cannot rely only on the periods as boundary conditions to select the best-fit model. In order to find other restrictions, to be able to overcome this issue, there are some general procedures that are used during the fits that are summarized below:

1. First, I search for the minimum in the quality function to ensure that our models match the observed periods;

2. When there are several families of solutions, I looked for those with $T_{\rm eff}$ inside 1 σ from the spectroscopic value. The log(g) could also be a boundary condition, but, in general, I use the effective temperature since the determinations of $T_{\rm eff}$ are more accurate than those of the log(g);

3. When available, I use external identification of the harmonic degree ℓ of the modes. If that information is not available, I give more weight to the model that fit the observed periods with similar amplitudes using the same harmonic degree ℓ.

4. For the stars that have a single detected mode, I often have several families of solutions that perfectly fit the observed period. Therefore, it is not possible to choose a single solution. In this case, I will present at least three possible best-fit models. Those solutions usually have the same order of hydrogen mass, which allows us to infer if the stars have a thick or a thin hydrogen envelope.

I calculate the internal uncertainties associated to the quantities $M_\star$, $T_{\rm eff}$, and $\log(L/L_\odot)$ using the following expression [130, 70]:

$$\sigma_{\rm i}^2 = \frac{d_{\rm i}^2}{S - S_0}, \tag{3.21}$$

where $(M_\star^0, M_{\rm H}^0, T_{\rm eff}^0)$ is the value of the quality function of the best-fit model and S is the value of the quality function when we change the parameter i by an amount of $d_{\rm i}$, keeping the other parameters fixed. The quantity $d_{\rm i}$ can be evaluated as the minimum step in the grid of parameters i. Those uncertainties are internal errors of the fitting procedure. Other uncertainties come from evolutionary computations and are not considered.

The results of the asteroseismological analysis are listed in Table 3 and 4. In Table 3, are presented the results of the asteroseismological fit for 22 stars of the sample that have a least two observed periods, while the results for the stars showing only one period are presented in Table 4. The Tables are organized as follows: columns 2, 3, and 4 show the effective temperature, stellar mass, and thickness of the hydrogen envelope of a given asteroseismological model, respectively. In columns 5 and 6 are shown the observed period and the amplitude used in the fitting procedure. The theoretical period along with the corresponding harmonic degree ℓ and the radial order k are listed in columns 7, 8, and 9. In columns 10, 11, and 12 are shown the difference between the observed and the theoretical period Δ, the value of the quality function $S(M_*, M_{\rm H}, T_{\rm eff})$, and the references where the observed modes were extracted. The best-fit model is always listed first, with other possible solutions listed below for comparison purposes.

The structural parameters of the best-fit models selected in the asteroseismological fit for each star analyzed in this work are listed in Table 5. The uncertainties in the $M_\star$, $T_{\rm eff}$ and $\log(L/L_\odot)$ were computed using the expression 3.21, while the uncertainties in the surface gravity and in the radius were propagated from them.

Table 3 – Results of the asteroseismological fits for 22 massive white dwarf stars that have at least two observed period.

Star	$T_{\rm eff}$ (K)	$M_\star/M_\odot$	$-\log(M_H/M_\star)$	$\Pi_i^{\rm obs}$ (s)	A(mma)	$\Pi_k^{\rm th}$(s)	ℓ	k	Δ (s)	S	Ref.
KIC 211914185	14 020	0.998	6.24	109.15	1.40	108.69	1	1	0.46	0.32	[5]
				190.45	1.85	190.40	1	3	0.05		
	12 986	0.877	7.38	109.15	1.40	109.60	1	1	-0.45	0.84	
				190.45	1.85	189.57	2	2	0.88		
J0052-0051	11 974	0.860	5.32	1077.2	4.0	1077.15	1	29	0.05	0.06	[131]
				1093.8	4.0	1093.76	2	51	0.04		
	12 504	0.976	6.06	1077.2	4.0	1077.68	1	31	-0.48	0.34	
				1093.8	4.0	1093.02	1	32	0.09		
J0840+5222	1 144	0.998	5.94	172.7	6.2	172.82	1	2	-0.12	0.67	[9]
				326.6	7.1	325.47	1	7	1.13		
				797.4	6.3	797.62	1	22	-0.22		
	12 479	1.024	6.38	172.7	6.2	174.01	1	2	-1.4	1.16	
				326.6	7.1	326.35	2	15	0.25		
				797.4	6.3	798.87	1	23	-1.47		
G207-9	12 394	0.949	5.66	129.4	1.1	125.95	2	3	3.45	2.53	[132]
				196.1	1.2	194.57	2	7	1.53		[133]
				254.29	10.4	252.96	1	5	1.33		*
				291.85	19.8	292.60	2	13	-0.75		
				305.2	0.4	302.25	1	6	2.95		
				317.20	5.3	317.79	2	14	-0.59		
				409.92	10.0	409.46	1	10	0.46		
				557.4	63.4	555.57	1	15	1.83		
				595.7	2.0	595.21	2	29	0.49		
				623.8	1.1	624.88	1	17	-1.08		
				740.4	46.4	743.62	1	21	-3.22		
J1812+4321	12 181	0.900	8.37	356.09	14.3	355.36	1	6	0.73	0.55	*
				743.44	11.1	743.19	2	30	0.25		
				798.66	12.1	799.07	1	18	-0.41		
	11 870	0.998	5.87	356.09	14.3	357.73	1	8	-1.64	1.08	
				743.44	11.1	743.72	1	20	-0.28		
				798.66	12.1	799.52	1	22	-0.86		
J1200-0251	11 866	0.770	5.46	257.10	6.69	255.10	2	8	2.0	2.09	[134]
				271.30	13.09	271.54	2	9	-0.24		
				294.10	6.69	295.01	2	10	-0.91		
				304.78	23.72	303.50	1	5	1.28		
	11 661	0.877	5.60	257.10	6.69	256.58	2	9	0.52	1.26	
				271.30	13.09	272.38	2	10	-1.08		
				294.10	6.69	293.35	2	11	0.75		
				304.78	23.72	304.90	2	12	-0.12		
J2208+2059	12 223	0.900	6.41	249.72	1.5	250.16	1	4	-0.44	1.40	[76]
				477.35	1.6	479.34	1	11	-1.99		
				538.84	5.1	537.77	2	23	1.07		
				558.89	8.5	559.84	1	13	-0.95		
				576.05	2.7	576.43	2	25	-0.38		
				592.60	4.5	594.21	1	14	-1.61		
	12 155	0.900	6.31	249.72	1.5	250.72	1	4	-1.00	1.72	
				477.35	1.6	478.73	1	11	-1.38		
				538.84	5.1	538.42	2	23	0.42		
				558.89	8.5	558.64	1	13	0.25		
				576.05	2.7	574.35	2	25	1.70		
				592.60	4.5	594.90	1	14	-2.30		
GD 518	11 905	0.976	5.99	440.2	1.5	440.20	1	11	0.00	1.24	[135]
				513.2	2.4	511.75	1	13	1.45		
				583.7	1.5	584.79	1	15	-1.09		
	12 181	1.024	6.52	440.2	1.5	440.23	2	21	-0.03	0.36	
				513.2	2.4	512.97	2	25	0.23		
				583.7	1.5	583.67	1	16	0.03		

*

Table 3 – (Continued)

Star	T_{eff} (K)	$M_\star/M_\odot$	$-\log(M_H/M_\star)$	Π_i^{obs} (s)	A(mma)	Π_k^{th}(s)	ℓ	k	Δ (s)	S	Ref.
J2214-0025	11 697	0.820	8.82	195.2	6.1	195.18	2	5	0.02	0.07	[136]
				255.2	13.1	255.14	1	3	-0.09		
	11 691	0.705	7.34	195.2	6.1	195.28	1	1	-0.08	0.23	
				255.2	13.1	255.51	1	3	-0.31		
J2209-0919	11 600	0.770	5.75	789.31	10.37	790.95	1	17	-1.64	1.40	[137]
				894.71	43.94	893.61	1	20	1.10		
	11 638	0.949	5.84	789.31	10.37	789.26	1	21	0.37	0.26	
				894.71	43.94	894.34	1	24	0.05		
BPM37093	12 382	0.949	5.76	511.7	0.7	507.54	1	13	4.16	2.08	[53]
				531.1	1.2	531.10	1	14	0.00		
				548.4	0.8	547.36	2	26	1.04		
				564.1	0.9	565.53	2	27	-1.43		
				582.0	1.0	582.79	2	28	-0.79		
				600.7	0.9	598.09	1	16	2.61		
				613.5	1.1	614.20	2	30	-0.70		
				635.1	1.1	635.31	2	31	-0.21		
				660.8	0.5	659.75	1	18	1.05		
	12 633	1.024	6.52	511.7	0.7	508.39	2	24	3.31	1.11	
				531.1	1.2	531.55	2	25	-0.55		
				548.4	0.8	551.10	2	26	-2.7		
				564.1	0.9	563.62	2	27	0.48		
				582.0	1.0	580.63	2	28	1.07		
				600.7	0.9	601.57	2	29	-0.87		
				613.5	1.1	609.76	1	16	3.74		
				635.1	1.1	637.35	1	17	-2.25		
				660.8	0.5	667.10	1	18	-6.3		
HE 0532-5605	11 460	0.860	5.99	586.4	1	586.58	1	13	-0.18	0.15	[138]
				688.8	1	688.90	1	16	-0.1		
	11 578	0.877	6.39	586.4	1	586.84	1	13	-0.46	0.45	
				688.8	1	688.35	1	16	0.45		
J0825+4119	11 559	0.800	4.89	611.0	11.2	611.18	1	14	-0.18	0.08	[139]
				653.4	17.1	653.42	1	15	-0.02		
	11 470	0.721	9.24	611.0	11.2	611.24	2	19	-0.24	0.25	
				653.4	17.1	653.11	1	11	0.29		
J1257+0124	11 277	0.837	5.88	377.8	6.6	375.37	2	6	-2.43	2.23	[140]
				398.1	6.7	398.48	1	13	-0.38		[76]
				466.4	8.9	465.29	2	8	-0.79		
				507.1	8.4	511.41	1	18	1.01		
				644.5	21.9	644.87	1	13	-0.37		
				786.9	8.9	787.45	2	16	-0.55		
				905.8	46.7	905.56	1	21	0.24		
				946.3	10.5	946.48	2	20	-0.18		
				1070.5	7.9	1069.34	2	40	-1.16		
	11 228	0.721	5.36	377.8	6.6	379.68	1	6	-1.88	1.92	[76]
				398.1	6.7	397.59	2	13	0.51		
				466.4	8.9	467.09	1	8	-0.79		
				507.1	8.4	506.38	2	18	0.72		
				644.5	21.9	649.15	1	13	-4.65		
				786.9	8.9	785.99	1	16	0.91		
				946.3	10.5	946.59	1	20	-0.29		
				1070.5	7.9	1070.92	2	40	-0.42		

*

Table 3 – (Continued)

Star	T_{eff} (K)	$M_\star/M_\odot$	$-\log(M_H/M_\star)$	Π_i^{obs} (s)	A(mma)	Π_k^{th}(s)	ℓ	k	Δ (s)	S	Ref.
J2128-0007	11 067	0.721	7.84	274.9	11.0	275.33	1	3	-0.43	0.33	[140]
				289.0	9.7	289.00	2	7	0.0		
				302.2	17.1	301.83	1	4	0.17		
	11 758	0.877	5.55	274.9	11.0	275.02	1	5	-0.12	0.37	
				289.0	9.7	288.69	2	11	0.31		
				302.2	17.1	302.37	2	12	-0.17		
J1323+0103	11 519	0.917	5.41	432.48	5.1	431.34	1	10	1.14	3.54	[123]
				497.40	6.3	489.59	1	12	7.81		[76]
				525.00	3.6	526.45	1	13	-1.45		
				550.47	8.6	550.77	2	25	-0.3		
				564.55	18.31	566.63	2	26	-2.08		
				590.13	7.1	590.73	2	27	-0.6		
				603.62	8.3	600.80	1	15	2.82		
				612.23	11.9	613.69	2	28	-1.46		
				636.39	4.8	636.23	2	29	0.16		
				656.02	15.2	658.11	2	30	-2.09		
				675.36	6.3	677.15	2	31	-1.79		
				698.64	4.3	693.81	1	18	4.83		
				731.62	5.2	730.90	2	34	0.73		
				831.06	4.6	832.62	2	39	-1.56		
				884.17	4.1	880.73	2	41	3.44		
J2159+1322	10 987	0.976	6.29	683.70	11.7	683.28	2	29	0.42	1.04	[136]
				746.67	24.2	746.07	1	18	0.60		[76]
				801.0	15.1	801.88	2	34	-0.88		
	11 004	0.900	6.02	683.70	11.7	683.50	1	16	0.2	0.26	
				746.67	24.2	746.83	1	18	-0.16		
				801.0	15.1	801.21	2	34	-0.21		
J0303+0808	11 303	0.877	5.60	707.0	4.1	706.85	1	17	0.15	0.26	[141]
				1128.0	3.5	1127.67	1	18	0.33		
	11 353	0.837	6.26	707.0	4.1	707.75	1	15	-0.75	0.58	
				1128.0	3.5	1127.67	1	25	0.33		
	11 265	0.820	5.87	707.0	4.1	707.10	2	28	-0.1	0.1	
				1128.0	3.5	1128.04	2	46	-0.04		
J1216+0922	11 669	0.770	7.33	409	30.1	408.87	1	6	0.13	2.00	[81]
				570	24.6	568.55	2	0	1.45		
				626	21.6	625.49	1	12	0.51		
				823	45.2	824.04	2	30	-1.04		
				840	42.0	837.80	1	17	2.20		
				967	20.5	970.02	1	20	-3.02		
	10 823	0.837	5.97	409	30.1	408.67	1	7	0.33	2.46	
				570	24.6	566.87	2	21	3.13		
				626	21.6	628.04	1	13	-2.14		
				823	45.2	823.86	1	18	-0.86		
				840	42.0	840.14	2	32	-0.14		
				967	20.5	966.89	2	37	0.11		
J0923-0120	11 088	0.877	6.29	668.9	3.5	669.69	1	15	-0.79	0.86	[50]
				595.1	2.7	595.39	1	13	-0.05		[76]
				1436.4	1.4	1435.16	1	34	0.37		
	11 496	0.949	5.76	655.7	4.4	655.87	1	17	-0.17	0.29	
				595.1	2.7	594.64	1	15	0.46		
				1436.4	1.4	1436.49	1	39	-0.09		
	11 306	0.800	5.39	595.1	2.7	594.37	1	13	0.73	0.52	[76]
				1436.4	1.4	1436.30	1	34	0.1		

*

Table 3 – (Continued)

Star	T_{eff} (K)	$M_\star/M_\odot$	$-\log(M_H/M_\star)$	Π_i^{obs} (s)	A(mma)	Π_k^{th}(s)	ℓ	k	Δ (s)	S	Ref.
J2208+0654	11 154	0.770	5.46	668.07	4.1	668.27	1	14	0.20	0.28	[134]
				757.23	4.5	756.89	1	16	0.16		
	11 138	0.837	5.97	668.07	4.1	668.01	1	14	0.06	0.12	
				757.23	4.5	757.14	2	29	0.09		
	11 183	0.998	5.87	668.07	4.1	668.22	1	17	-0.15	0.20	
				757.23	4.5	757.09	2	34	0.14		
J1711+6541	10 779	0.837	5.00	214.3	1.7	214.90	2	7	-0.60	3.00	[139]
				234.0	1.2	236.91	1	4	-2.71		[71]
				561.5	3.0	561.91	1	13	-0.41		
				609.5	5.5	610.01	1	14	-0.51		
				690.2	3.3	690.27	2	29	-0.07		
				934.8	2.9	935.37	2	40	-0.57		
				1186.6	3.3	1183.32	2	51	3.28		
				1248.2	3.2	1253.38	1	31	-5.18		

Note. The main structure parameters are isted for each star given by the asteroseismological solution. It is also listed the observed and the theoretical periods with the corresponding harmonic degree ℓ and the radial order k. The best-fit model is listed first; other solutions are also listed for comparison. The last column has the references from where the periods have been extracted.

*Romero et al. (2021), in preparation.

Table 4 – Results of the asteroseismological fits for 18 massive white dwarf stars that have only one observed period.

Star	$T_{\rm eff}$ (K)	$M_\star/M_\odot$	$-\log(M_{\rm H}/M_\star)$	$\Pi_{\rm i}^{\rm obs}$ (s)	A(mma)	$\Pi_{\rm k}^{\rm th}$(s)	ℓ	k	S	Ref.
HS 1531+7436	13 409	0.917	5.76	112.5	4.2	112.49	1	1	0.01	[142]
	12 792	0.917	5.73	112.5	4.2	112.50	1	1	0.00	
	13 196	1.024	6.52	112.5	4.2	112.49	1	1	0.01	
G226-29	12 571	0.860	5.27	109.27	1.1	109.32	1	1	0.05	[143, 35]
	12 270	0.770	4.69	109.27	1.1	109.25	1	1	0.02	
	12 782	0.900	5.52	109.27	1.1	109.26	1	1	0.01	
J1612+0830	12 174	0.770	4.91	116.2	5.1	116.20	1	1	0.00	[139, 71]
	12 373	0.820	5.22	116.2	5.1	116.21	1	1	0.01	
J1641+3521	12 109	0.770	5.00	809.3	27.3	809.40	1	19	0.10	[140]
	11 709	0.800	5.29	809.3	27.3	809.42	1	19	0.12	
J2038+7710	12 289	0.837	7.35	203.7	17.7	203.83	1	2	0.13	[9]
	12 134	0.917	7.87	203.7	17.7	203.73	1	2	0.03	
J2153-0731	11 909	0.705	6.54	210.2	5.6	210.08	1	2	0.12	[140]
	11 900	0.659	6.24	210.2	5.6	210.20	1	2	0.00	
J0621+2523	11 646	0.745	6.34	830.0	1.9	829.99	1	17	0.01	[4]
	11 691	0.949	7.88	830.0	1.9	829.98	1	19	0.02	
WD 2102+233	11 714	0.770	7.33	800.0	26.0	799.97	1	16	0.03	[144]
	11 721	0.820	5.58	800.0	26.0	800.02	1	19	0.02	
J0939+5609	11 671	0.770	4.91	249.9	7.2	249.90	1	4	0.00	[9]
	11 506	0.721	9.24	249.9	7.2	249.90	1	2	0.00	
	11 659	0.837	5.40	249.9	7.2	249.89	1	4	0.01	
J1554+2410	11 544	0.900	5.52	673.6	2.2	673.59	1	17	0.01	[9]
	10 954	0.917	8.37	673.6	2.2	673.60	1	14	0.00	
J1337+0104	11 338	0.998	6.24	715.0	10.0	715.01	1	18	0.01	[81]
	11 198	0.860	6.38	715.0	10.0	715.00	1	16	0.00	
KUV 0159-1109	11 339	0.770	5.85	687.0	15.0	687.02	1	14	0.02	[6]
	11 366	0.800	5.39	687.0	15.0	686.97	1	15	0.03	
J1036+2115	11 342	0.770	4.91	680.0	23.0	679.95	1	15	0.05	[6]
	11 323	0.745	4.62	680.0	23.0	680.09	1	15	0.09	
J1015+2340	11 401	0.877	6.10	498.5	4.9	498.5	1	11	0.00	[9]
	11 510	0.820	6.36	498.5	4.9	498.5	1	10	0.00	
	11 215	0.949	5.84	498.5	4.9	498.49	1	12	0.01	
J2041-0417	10 936	0.837	5.08	525.0	17.0	524.97	1	12	0.03	[6]
	11 262	0.820	4.99	525.0	17.0	524.97	1	12	0.03	
	11 314	0.800	6.84	525.0	17.0	525.0	1	10	0.00	
J0041-0308	10 986	0.820	5.06	870.0	5.0	870.17	1	21	0.17	[6]
	11 138	0.820	5.13	870.0	5.0	870.02	1	21	0.02	
J1650+3010	10 982	0.860	9.27	339.06	14.7	339.03	1	3	0.03	[141]
	10 797	0.820	9.59	339.06	14.7	339.06	1	4	0.00	
	11 017	0.721	8.33	339.06	14.7	339.07	1	4	0.01	
J0940+0052	10 550	0.800	7.84	255.36	17.1	255.41	1	3	0.05	[134]
	10 745	0.877	5.11	255.36	17.1	255.34	1	4	0.02	
	10 503	0.820	5.22	255.36	17.1	255.33	1	4	0.03	

Table 5 – Structural parameters for the best-fit models corresponding to each DAV star analyzed in this paper. Surface gravity, effective temperature, stellar mass, hydrogen and helium mass weighted by the stellar mass, luminosity and radius weighted by solar radius and finally the oxygen abundance of the core are listed. The uncertainties are the internal errors of the fitting procedure, as described in section 3.4.

Star	log(g)	T_{eff} [K]	$M_*/M_\odot$	M_H/M_*	M_{He}/M_*	$\log(L/L_\odot)$	$\log(R/R_\odot)$	X_O	Crist (%)
KIC 211914185	8.64 ± 0.04	$14\,020 \pm 197$	0.998 ± 0.026	5.75×10^{-7}	7.74×10^{-4}	-2.67 ± 0.03	-2.10 ± 0.01	0.601	0
J0052-0051	8.42 ± 0.04	$11\,974 \pm 53$	0.860 ± 0.023	4.78×10^{-6}	2.84×10^{-3}	-2.78 ± 0.01	-2.02 ± 0.02	0.561	0
J0840+5222	8.65 ± 0.02	$12\,144 \pm 150$	0.998 ± 0.026	1.15×10^{-6}	7.73×10^{-4}	-2.92 ± 0.02	-2.10 ± 0.01	0.601	16.8
G207-9	8.57 ± 0.04	$12\,394 \pm 100$	0.949 ± 0.032	2.18×10^{-6}	1.19×10^{-3}	-2.82 ± 0.01	-2.07 ± 0.01	0.582	0
J1812+4321	8.49 ± 0.03	$12\,181 \pm 105$	0.900 ± 0.023	4.26×10^{-9}	1.92×10^{-3}	-2.81 ± 0.01	-2.05 ± 0.02	0.565	0
J1200-0251	8.29 ± 0.04	$11\,866 \pm 65$	0.770 ± 0.030	3.47×10^{-6}	5.97×10^{-3}	-2.71 ± 0.01	-1.98 ± 0.01	0.546	0
J2208+2059	8.49 ± 0.03	$12\,223 \pm 72$	0.900 ± 0.023	3.89×10^{-7}	1.92×10^{-3}	-2.79 ± 0.01	-2.05 ± 0.01	0.565	0
GD 518	8.61 ± 0.04	$11\,905 \pm 120$	0.976 ± 0.027	1.02×10^{-6}	1.12×10^{-3}	-2.92 ± 0.01	-2.09 ± 0.02	0.586	8.1
J2214-0025	8.37 ± 0.02	$11\,697 \pm 42$	0.820 ± 0.020	1.51×10^{-9}	3.90×10^{-3}	-2.79 ± 0.012	-2.01 ± 0.01	0.550	0
J2209-0919	8.29 ± 0.02	$11\,600 \pm 120$	0.770 ± 0.030	1.77×10^{-6}	5.98×10^{-3}	-2.75 ± 0.02	-1.98 ± 0.01	0.546	0
BPM37093	8.57 ± 0.04	$12\,382 \pm 100$	0.949 ± 0.032	1.73×10^{-6}	1.19×10^{-4}	-2.82 ± 0.01	-2.07 ± 0.02	0.582	0
HE 0532-5605	8.43 ± 0.02	$11\,460 \pm 46$	0.860 ± 0.023	1.02×10^{-6}	2.85×10^{-3}	-2.86 ± 0.01	-2.03 ± 0.01	0.561	0
J0825+4119	8.33 ± 0.03	$11\,599 \pm 54$	0.800 ± 0.030	1.29×10^{-5}	4.72×10^{-3}	-2.77 ± 0.01	-1.99 ± 0.01	0.549	0
J1257+0124	8.37 ± 0.02	$11\,277 \pm 160$	0.837 ± 0.023	1.31×10^{-6}	3.19×10^{-3}	-2.84 ± 0.02	-2.01 ± 0.02	0.552	0
J2128-0007	8.22 ± 0.02	$11\,067 \pm 65$	0.721 ± 0.024	1.44×10^{-8}	7.25×10^{-3}	-2.79 ± 0.01	-1.96 ± 0.01	0.659	0
J1323+0103	8.52 ± 0.02	$11\,518 \pm 64$	0.917 ± 0.032	3.89×10^{-6}	1.31×10^{-3}	-2.91 ± 0.01	-2.05 ± 0.01	0.609	0
J2159+1322	8.60 ± 0.02	$10\,988 \pm 50$	0.976 ± 0.027	5.12×10^{-7}	1.10×10^{-3}	-3.07 ± 0.01	-2.09 ± 0.02	0.586	37.3
J0303+0808	8.46 ± 0.02	$11\,303 \pm 35$	0.877 ± 0.023	2.51×10^{-6}	2.59×10^{-3}	-2.90 ± 0.01	-2.03 ± 0.01	0.568	0
J1216+0922	8.29 ± 0.03	$11\,669 \pm 40$	0.770 ± 0.030	4.67×10^{-8}	5.97×10^{-3}	-2.75 ± 0.01	-1.98 ± 0.01	0.546	0
J0923-0120	8.46 ± 0.02	$11\,088 \pm 35$	0.877 ± 0.023	5.13×10^{-7}	2.59×10^{-3}	-2.94 ± 0.01	-2.04 ± 0.01	0.568	0
J2208+0654	8.30 ± 0.03	$11\,154 \pm 36$	0.770 ± 0.030	3.46×10^{-6}	5.97×10^{-3}	-2.82 ± 0.01	-1.98 ± 0.01	0.546	0
J1711+6541	8.39 ± 0.03	$10\,779 \pm 101$	0.837 ± 0.023	9.77×10^{-6}	3.19×10^{-3}	-2.94 ± 0.01	-2.01 ± 0.01	0.552	0
HS 1531+7436	8.52 ± 0.03	$13\,409 \pm 380$	0.917 ± 0.032	1.73×10^{-6}	1.31×10^{-3}	-2.65 ± 0.022	-2.05 ± 0.01	0.609	0
G226-29	8.43 ± 0.04	$12\,571 \pm 370$	0.860 ± 0.023	5.37×10^{-6}	2.85×10^{-3}	-2.70 ± 0.04	-2.02 ± 0.01	0.561	0
J1612+0830	8.30 ± 0.05	$12\,174 \pm 220$	0.770 ± 0.030	1.23×10^{-5}	5.97×10^{-3}	-2.66 ± 0.03	-1.98 ± 0.01	0.546	0
J1641+3521	8.30 ± 0.05	$12\,109 \pm 48$	0.770 ± 0.030	1.00×10^{-5}	5.97×10^{-3}	-2.67 ± 0.01	-1.98 ± 0.01	0.546	0
J2038+7710	8.40 ± 0.03	$12\,289 \pm 355$	0.837 ± 0.023	4.46×10^{-8}	3.16×10^{-3}	-2.72 ± 0.05	-2.02 ± 0.01	0.552	0
J2153-0731	8.19 ± 0.03	$11\,909 \pm 280$	0.705 ± 0.016	2.88×10^{-7}	7.66×10^{-3}	-2.64 ± 0.07	-1.95 ± 0.01	0.534	0
J0621+2523	8.25 ± 0.02	$11\,646 \pm 21$	0.745 ± 0.025	4.57×10^{-7}	6.24×10^{-3}	-2.72 ± 0.01	-1.97 ± 0.01	0.589	0
WD 2102+233	8.30 ± 0.02	$11\,714 \pm 25$	0.770 ± 0.030	4.67×10^{-8}	5.96×10^{-3}	-2.74 ± 0.02	-1.98 ± 0.01	0.546	0
J0939+5609	8.28 ± 0.02	$11\,671 \pm 45$	0.770 ± 0.030	1.23×10^{-5}	5.97×10^{-3}	-2.73 ± 0.01	-1.98 ± 0.01	0.546	0
J1554+2410	8.49 ± 0.02	$11\,544 \pm 24$	0.900 ± 0.023	3.02×10^{-6}	1.91×10^{-3}	-2.90 ± 0.01	-2.05 ± 0.01	0.565	0
J1337+0104	8.65 ± 0.02	$11\,338 \pm 48$	0.998 ± 0.026	5.75×10^{-7}	7.73×10^{-4}	-3.04 ± 0.01	-2.10 ± 0.02	0.601	41.7
KUV 0159-1109	8.29 ± 0.03	$11\,339 \pm 24$	0.770 ± 0.030	1.41×10^{-6}	5.98×10^{-3}	-2.79 ± 0.01	-1.98 ± 0.01	0.546	0
J1036+2115	8.28 ± 0.03	$11\,342 \pm 28$	0.770 ± 0.030	1.23×10^{-5}	5.97×10^{-3}	-2.78 ± 0.01	-1.98 ± 0.01	0.546	0
J1015+2340	8.46 ± 0.02	$11\,401 \pm 31$	0.877 ± 0.023	7.94×10^{-7}	2.59×10^{-3}	-2.89 ± 0.01	-2.04 ± 0.01	0.568	0
J2041-0417	8.39 ± 0.03	$10\,936 \pm 35$	0.837 ± 0.023	8.31×10^{-6}	3.18×10^{-3}	-2.92 ± 0.03	-2.01 ± 0.01	0.552	0
J0041-0308	8.36 ± 0.02	$10\,986 \pm 68$	0.820 ± 0.020	8.70×10^{-6}	3.89×10^{-3}	-2.89 ± 0.01	-2.00 ± 0.01	0.550	0
J1650+3010	8.44 ± 0.02	$10\,982 \pm 50$	0.860 ± 0.023	5.37×10^{-10}	2.85×10^{-3}	-2.94 ± 0.012	-2.03 ± 0.01	0.561	0
J0940+0052	8.35 ± 0.03	$10\,550 \pm 83$	0.800 ± 0.030	1.44×10^{-8}	4.74×10^{-3}	-2.95 ± 0.02	-2.00 ± 0.01	0.549	0

4 Results and Discussion

4.1 Particular Cases

In this section, I will discuss in detail the asteroseismological analysis of a few objects that require additional attention.

G207-9: This is a classical ZZ Ceti, the eighth known member of the DAVs, first observed by Robinson et al. (1976) [132] which detected four periods with very high amplitude and one with a low amplitude. Then, thirty years later, this star was observed again over 24 nights in the Konkoly Observatory, with the data published in the work of Bognar et al. (2016b) [133], consisting of 7 periods (five new ones and two observed previously). Also, this star was observed in Sector 26 of TESS mission (Romero et al. 2021, in preparation). We were able to detect four new pulsation periods, along with four that have already been observed before in previous works [132, 133]. Unfortunately, three of the four new periods are shorter than 240 seconds and are not trustworthy. This is due to the available TESS data for this star, which has only 120 seconds cadence. For this star, I fit the period spectrum of each observation individually, and then I do the fit considering all the periods. In all fitting procedures, the solutions are in the range of 0.9-1.05 $M_{\odot}$, with effective temperatures in the range 12 000-12 600K, more massive and hotter than the spectroscopic determinations (0.82 $M_{\odot}$ and 12 080 K). Interestingly, models with a mass of 0.949 $M_{\odot}$ are always present among the solutions. The best-fit model for G207-9 has a mass of 0.949 $M_{\odot}$, with a thick hydrogen envelope ($M_H = 2.19 \times 10^{-6} M_{\star}$), and an effective temperature of 12 394 K. This model is more massive and hotter than the spectroscopic determinations and also than the best-fit model found in the work of Romero et al. (2013) [76].

J1812+4321: This star was discovered within TESS, in Sectors 25 and 26. Three low amplitude modes were detected (356, 743, and 798 sec), characteristic of stars in the hot edge of the instability strip. I searched for a model that fits the period with the highest amplitude with $\ell = 1$ and a maximum difference of 1 sec. I have found two families of solutions: one of them has masses higher than 0.949 $M_{\odot}$, with hydrogen envelopes typically thicker than $-\log(M_H/M_{\star}) = 6$, and effective temperature lower than 11 500 K; the other family of solutions is in the mass range of 0.7-0.917 $M_{\odot}$, with thinner hydrogen envelopes and effective temperatures above 11 700 K. To break this degeneracy in the solutions, I use the temperature and log(g) obtained using the GAIA photometry [125] and selected a best-fit model with a mass of 0.90 $M_{\odot}$, a thin hydrogen envelope ($M_H = 4.25 \times 10^{-9} M_{\star}$), and an effective temperature of 12 181 K.

GD 518: Reported by Hermes et al. (2013) [135], this is an ultra massive ZZ Ceti star, with T_{eff} = 11 760 K, log(g) = 8.97, and with a mass of 1.15 $M_{\odot}$. Thus, this star may harbor a C/O/Ne core, or even an O/Ne core [13, 15, 16]. However, due to the uncertainties on the transition mass where the neon abundance becomes significant, the C/O core composition cannot be excluded [145]. In this scenario, low radial orders pulsation modes could be an important ally of the core composition identification once these modes mainly propagate in inner regions. However, for stars in this range of mass and temperature the crystallization is in advanced stages (30 - 90% of the star could be in the solid-state [146]), affecting the core chemical profile and the pulsation properties. As the g-modes do not propagate in solid material, they cannot provide information about the core composition. For this object, there were only three periods detected, all of them longer than 400 seconds. The period-to-period fit indicates that the best-fit model has a stellar mass of M=0.976 $M_{\odot}$, effective temperature of T_{eff}= 11 905 K, hydrogen mass of $M_H = 1.02 \times 10^{-6} M_{\star}$, and with a quality function S= 1.24 s. This solution has a mass 0.174 $M_{\odot}$ lower than the spectroscopy determination, however, has a consistent effective temperature and fits all the periods with good precision. The best-fit model shows that 8.1% of the mass of the star is crystallized. Our result is in good agreement with those from Córsico et al. (2019b) [77] in terms of the hydrogen mass and effective temperature, but they obtained a higher stellar mass of M=1.22 $M_{\odot}$ and 97% of its mass crystallized, using O/Ne-core DA white dwarf models.

BPM 37093: Discovered by Kanaan et al. (1992) [147], this object was the first ultra-massive ZZ Ceti star observed. This star shows a log(g) of 8.69 and an T_{eff} = 11 620 K (corrected using 3D models atmospheres), giving a spectroscopic mass of 1.024 $M_{\odot}$. This star has nine detected frequencies [53], being BPM 37093 an important object in the study of the massive and ultra-massive ZZ Ceti stars. A detailed asteroseismological analysis was carried out by Córsico et al. (2020b) [148], which used the effective temperature and log(g) not corrected by 3D as boundary conditions. The authors used white dwarfs models with oxygen/neon core in their study. They found a seismological model with 1.16 $M_{\odot}$, T_{eff} = 11 650K and 92.3% of crystallization, using the eight periods published by Metcalfe et al. (2004) [149]. In the fitting procedure, I used the nine observed modes reported by Kanaan et al. (2005) [53], which used the WET (Whole Earth Telescope) observations. The best-fit model has a mass of M=0.949$M_{\odot}$, with $M_H = 1.74 \times 10^{-6} M_{\star}$, and an effective temperature of T_{eff} = 12 382K. This model is less massive and hotter than the spectroscopic determination, and I believe that our model grid cannot consistently reproduce this star. One of the possible reasons is that this star is inside the mass range of (1.024-1.15 $M_{\odot}$) where Lauffer et al. (2018) [16] found hybrid C/O-O/Ne core white dwarfs. In this case, not even the O/Ne core white dwarf models of Córsico et al. (2019) [77] could provide a consistent asteroseismological solution. Therefore, BPM 37093, which is the ultra-massive ZZ Ceti star with the higher number of periods detected, remains an

open subject for asteroseismological studies.

KIC 211914185: This is the hottest object on our list. It has a rotation period of 1.13 hrs and it is the fastest known isolated pulsating star [5]. It has a log(g) of 8.43 and a $T_{\rm eff} = 13\,590K$, resulting in a spectroscopic mass of M=0.867 $M_{\odot}$. This object has two short periods detected, 109.15 and 190.45 s, with low amplitudes, each one of them the center of a triplet. Due to this, I searched for models that fit both modes with $\ell = 1$. I find solutions compatible with the spectroscopic mass but not so much with the effective temperature. In this case, the best-fit model have a mass of M=0.867 $M_{\odot}$, $T_{\rm eff} = 12\,986$ K and $-\log(M_{\rm H}/M_{\star}) = 7.38$. However, with the identification of both modes with a harmonic degree $\ell = 1$, the best-fit model has a mass of 0.998 $M_{\odot}$, $T_{\rm eff} = 14\,020$ K, and $-\log(M_{\rm H}/M_{\star}) = 6.24$.

J0052-0051: This object is part of a detached white dwarf plus main-sequence star binary system [131]. The WD component has two long periods detected, 1077 and 1093 s, with low amplitude. Restricting the solution for models that fit both modes with $\ell = 1$, I only found solutions hotter and massive than the spectroscopy determination. Thus I chose to fit both modes with $\ell = 2$. The best-fit model has a mass of 0.860 $M_{\odot}$, $T_{\rm eff} = 11\,974K$ and $-\log(M_{\rm H}/M_{\star}) = 5.07$. I also detected a second possible solution with 0.976 $M_{\odot}$ and $-\log(M_{\rm H}/M_{\star}) = -6.06$, ten times thinner than our best-fit model, which can be interpreted in terms of the core-envelope symmetry described in Montgomery et al. (2003) [150].

J0840-5222: This is another ultra-massive ZZ Ceti star, first published by Curd et al. (2017) [9], with three pulsation modes (172.7, 326.6, and 797.4 sec). The spectroscopic analysis suggests that this object has a log(g) of 8.93 and a $T_{\rm eff} = 12\,160K$, which gives a mass of 1.13$M_{\odot}$. Curd et al. (2017) performed an asteroseismological analysis using sequences computed with the LPCODE, with a mass in the range of 1.024 - 1.15$M_{\odot}$, and C/O core. Their best-fit model have a mass of 1.14 $M_{\odot}$, $M_{\rm H} = 5.8 \times 10^{-7} M_{\star}$, effective temperature in the range 11 850 - 12 350 K, and a of 50 - 70% of its mass crystallized. Córsico et al. (2020b) [148] also analyzed this star and found a solution with 1.10 $M_{\odot}$, $T_{\rm eff} = 12\,550K$, $M_{\rm H} = 1.02 \times 10^{-7} M_{\star}$, and a crystallized ratio of 81%, using O/Ne core white dwarf models. I found as the best-fit model a mass of 0.998 $M_{\odot}$, an effective temperature of 12 144 K, and a hydrogen mass of $M_{\rm H} = 1.15 \times 10^{-6} M_{\star}$, 100 times thicker than the solutions of Curd et al. (2017) and Córsico et al. (2020b). This model has 16.8% of the mass crystallized. The model fits the three modes with $\ell = 1$ and S=0.67 s. If the spectroscopic determination of log(g) was overestimated, then this model is a good solution.

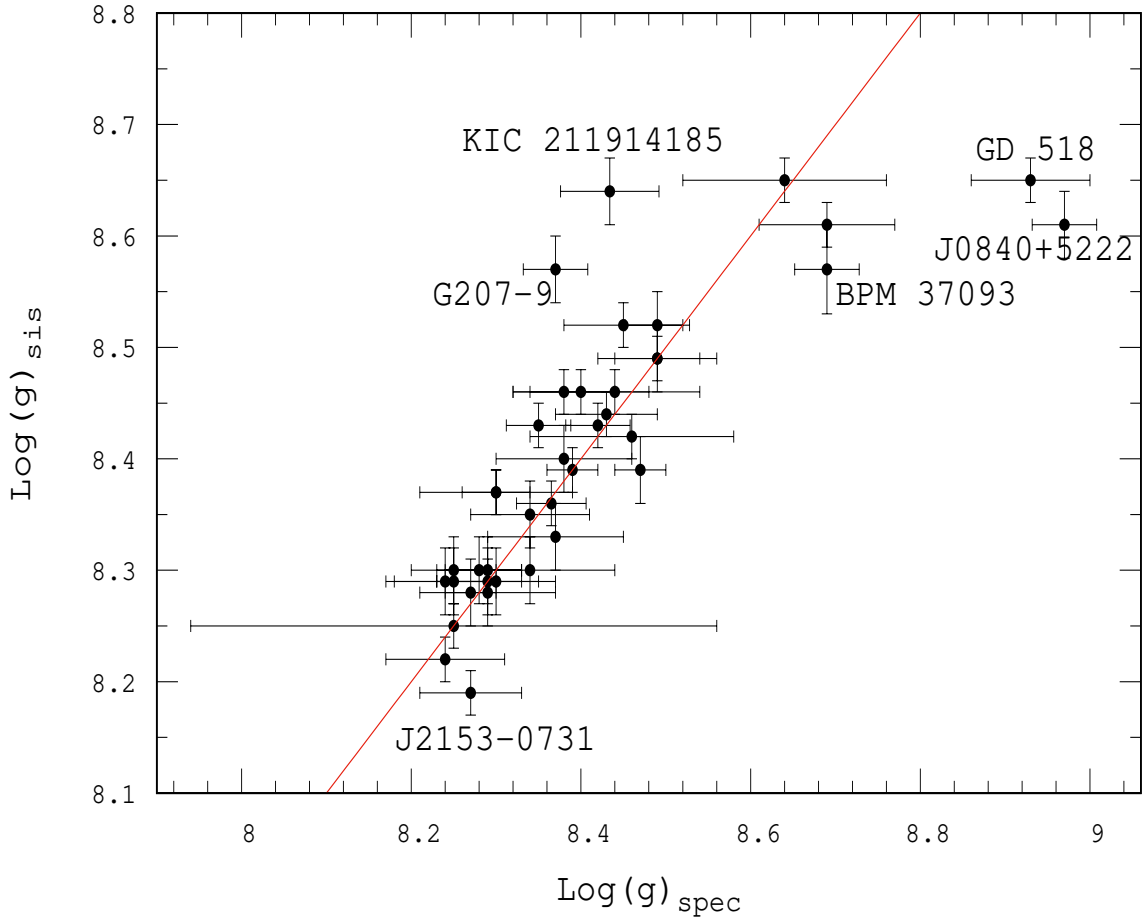

Figure 10 – Comparison between the values of surface gravity according to asteroseismology and spectroscopic 3D determinations. The uncertainties in the asterosismological log(g) are due to internal errors in the fitting procedure. The red line is the 1:1 correspondence.

4.2 Surface gravity from asteroseismology

In the analysis of the correspondence between the spectroscopy and the asteroseismological determinations performed in this work, I use directly the log(g) instead of the mass to avoid one more transformation and its uncertainties. Figure 10 shows the comparison between the spectroscopic (y-axis) and asteroseismological (x-axis) log(g) determinations. The red line is the 1:1 correspondence. We can see that the agreement between both sets of estimations is good, with the bulk of points accumulating around the 1:1 line. This result is excellent when compared to one reported by Romero et al. (2013). Probably solutions were being lost because of the limited number of sequences for the cooling curve of white dwarfs. Therefore, the ∼500 sequences computed for this work and added with the existing ones (summing ∼800) improved the correspondence between the spectroscopic and seismological log(g) determinations. However, there are five objects quite out of the 1:1 correspondence, all located above the log(g) = 8.55. The discrepancy

between the spectroscopic and seismological log(g) could reside in the fact that these stars are in the range of mass where a core composed of carbon and oxygen it is not expected [145].

The mean value of the asteroseismological mass is $\langle M_\star \rangle_{\rm sis} = 0.84 \pm 0.04 M_\odot$. whereas the average spectroscopic mass is $\langle M_\star \rangle_{\rm spec} = 0.84 \pm 0.07 M_\odot$. This agreement between asteroseismology and spectroscopy is encouraging since the methods used to derive both values are quite different. Also, they rely on two different and independent sets of observational data: the spectrum for the spectroscopy and the observed periods for the asteroseismology. If I do not consider the two ultra-massive stars of the sample, i.e. J0840+5222 and GD-518, the values are $\langle M_\star \rangle_{\rm sis} = 0.84 \pm 0.04 M_\odot$. for the asteroseismological determination, and $\langle M_\star \rangle_{\rm spec} = 0.83 \pm 0.05 M_\odot$ for the spectroscopic determination. Finally, despite some outliers, the agreement between the mean spectroscopic and asteroseismological mass is satisfactory.

4.3 Using GAIA data

In 2018, the groundbreaking second data release (DR2) of the *Gaia* mission [151] led to a true revolution in the field of white dwarfs. With accurate parallax measurements, this data enables the possibility to search for these objects on a unique scale. The early Data Release 3 (2020) of *Gaia* (EDR3) [152], relies on 34 months of observations, representing an improvement on all fronts over DR2, with parallax measurements being 20 to 30 percent more accurate [152]. For the ZZ Ceti stars, the data from the *Gaia* mission provide us additional information with the measurements of the magnitudes and distances. This makes it possible to estimate the atmospheric parameters, like the log(g) and the effective temperature, independently from the spectroscopy.

The atmospheric parameters were extracted from the work of Gentile Fusillo et al. (2021) [153], that has used the *Gaia* EDR3 data for the computations. The authors employed the standard H-atmosphere spectral models of Tremblay et al. (2011), which includes the Lα red wing absorption of Kowalski & Saumon (2006) [154]. For the white dwarf stars with masses above 0.46 $M_\odot$, they used the evolutionary sequences with thick hydrogen layers ($M_{\rm H}/M_{\rm WD} = 10^{-4}$) of Fontaine et al. (2001) [155][1]. The parallax, G apparent magnitude, $G_{\rm bp} - G_{\rm rp}$ color, $M_{\rm G}$ absolute magnitude, and log(g) are listed in columns 2, 3, 4 and 5, of Table 6, respectively. Unfortunately, seven stars of our sample (G226-29, J005208.42-005134.7, G207-9, GD-518, BPM 37093, KUV 0159-1109, and J030325.22-080834.9) are not present in the Gentile Fusillo et al. (2021) catalog, since the authors only searched for a 3 arcsec radius, which excludes the stars with elevated uncertainties in proper motion.

[1] For further details about obtaining the parameters is recommended to consult [156]

Table 6 – *Gaia* EDR3 data for 33 stars of the sample. The parallax (col 2), apparent G magnitude (col 3), color $G_{bp} - G_{rp}$ (col 4), absolute magnitude M_G (col 5), and log(g) (col 6) are listed. The objects not present are: G226-29, J005208.42-005134.7, G207-9, GD-518, BPM 37093, KUV 0159-1109, and J030325.22-080834.9.

Star	parallax (mas)	G	$G_{bp} - G_{rp}$	M_G	$log(g)$
KIC 211914185	4.8 ± 0.3	18.870 ± 0.004	0.010	12.285	8.4 ± 0.2
J0840+5222	7.4 ± 0.2	18.315 ± 0.003	0.042	12.658	8.5 ± 0.1
J1812+4321	17.21 ± 0.03	18.224 ± 0.003	0.005	12.423	8.48 ± 0.02
J1200-0251	5.4 ± 0.2	18.207 ± 0.003	0.050	11.855	7.9 ± 0.1
J2208+2059	11.01 ± 0.09	17.487 ± 0.003	0.084	12.285	8.37 ± 0.2
J2214-0025	6.7 ± 0.1	17.895 ± 0.003	0.022	12.031	8.1 ± 0.1
J2209-0919	5.2 ± 0.3	18.587 ± 0.005	0.104	12.182	8.1 ± 0.3
HE 0532-5605	20.10 ± 0.03	15.932 ± 0.003	0.040	12.448	8.41 ± 0.02
J0825+4119	5.9 ± 0.2	18.566 ± 0.003	0.057	12.411	8.4 ± 0.2
J1257+0124	4.4 ± 0.2	18.665 ± 0.004	-0.074	11.872	8.3 ± 0.2
J2128-0007	6.1 ± 0.2	18.009 ± 0.003	0.038	11.930	8.1 ± 0.1
J1323+0103	5.5 ± 0.2	18.549 ± 0.004	-0.006	12.261	8.4 ± 0.2
J2159+1322	5.1 ± 0.2	18.959 ± 0.004	0.049	12.497	8.5 ± 0.2
J1216+0922	4.5 ± 0.2	18.542 ± 0.004	0.114	11.810	7.8 ± 0.2
J0923-0120	7.41 ± 0.2	18.402 ± 0.003	0.026	12.753	8.6 ± 0.1
J2208+0654	7.6 ± 0.1	17.972 ± 0.003	0.030	12.395	8.4 ± 0.1
J1711+6541	12.63 ± 0.05	16.947 ± 0.003	0.036	12.455	8.44 ± 0.04
HS 1531+7436	13.45 ± 0.03	16.541 ± 0.003	-0.016	12.184	8.37 ± 0.03
J1612+0830	7.8 ± 0.1	17.806 ± 0.003	-0.003	12.259	8.38 ± 0.07
J1641+3521	3.6 ± 0.2	19.092 ± 0.004	0.083	11.912	8.0 ± 0.2
J2038+7710	3.7 ± 0.2	19.096 ± 0.004	-0.078	11.978	8.4 ± 0.2
J2153-0731	4.1 ± 0.2	18.506 ± 0.003	-0.029	11.551	7.9 ± 0.2
J0621+2523	7.2 ± 0.1	17.609 ± 0.003	0.094	11.899	7.9 ± 0.1
WD 2102+233	14.78 ± 0.04	15.985 ± 0.003	0.031	11.834	8.03 ± 0.03
J0939+5609	4.2 ± 0.2	18.754 ± 0.003	-0.006	11.872	8.2 ± 0.2
J1554+2410	8.91 ± 0.08	17.602 ± 0.003	0.046	12.352	8.36 ± 0.05
J1337+0104	6.1 ± 0.2	18.601 ± 0.003	0.052	12.541	8.4 ± 0.1
J1036+2115	8.89 ± 0.08	17.572 ± 0.003	0.037	12.317	8.35 ± 0.06
J1015+2340	5.7 ± 0.2	18.711 ± 0.004	0.069	12.500	8.4 ± 0.2
J2041-0417	6.9 ± 0.2	18.285 ± 0.003	0.066	12.485	8.40 ± 0.01
J0041-0308	7.4 ± 0.1	18.041 ± 0.003	0.031	12.389	8.40 ± 0.07
J1650+3010	7.7 ± 0.1	18.151 ± 0.003	0.104	12.595	8.37 ± 0.09
J0940+0052	4.7 ± 0.2	18.190 ± 0.003	0.083	11.551	7.7 ± 0.1

In order to test our asteroseismological log(g) distribution, I compared the values of log(g) obtained by Gentile Fusillo et al. (2021) with the values obtained from the best-fit models of this work. The result is presented in Figure 11. The uncertainties of the asteroseismological log(g) are obtained as described in Section 3.4, whereas the uncertainties in the log(g) obtained from *Gaia* are extracted from Gentile Fusillo et al. (2021) catalog.

For most objects, the correspondence between both determinations is in good agreement. It is possible to see that the log(g) obtained from *Gaia* EDR3 data are, in general, lower than those of asteroseismology. Also, only two out of the five outliers are

present in the catalog, for the reasons explained before. For KIC 211914185, the behavior is the same as observed in the comparison with the spectroscopy: the log(g) obtained from asteroseismology is higher. However, the log(g) from *Gaia* EDR3 data agrees with the log(g) from spectroscopy. This may suggest that the asteroseismological fit for this object was not good. The 109 s period, identified with $\ell = 1$ of this star, will always return a massive solution. Therefore, only the detection of further periods could solve this problem. For J0804+5222, the log(g) from *Gaia* EDR3 data is in agreement with the log(g) from asteroseismology, considering the uncertainties. Therefore, as discussed in Section 4.1, the spectroscopic log(g) determination for this star may be overestimated. Finally, the objects with only one period detected were highlighted (red squares) from those with at least two periods (black dots) in order to enable us to see some tendency behavior of the points. That is necessary because the spectroscopic log(g) was used as an additional boundary condition during the asteroseismological fits of these stars. Nevertheless, the objects with one period are spread all over the log(g) plane, and no tendency in the points distribution was found.

4.4 Effective temperature

Figure 12 shows a comparison between the spectroscopic (x-axis) and asteroseismological effective temperature (y-axis). The diagonal red line shows the 1:1 correspondence. This figure reveals a good agreement between both determinations, being BPM 37093 the largest discrepancy, with a 760 K difference between the spectroscopic and asteroseismological determination. As discussed in detail in Section 4.1, I only found solutions with effective temperatures above 12 000 K for BPM 37093, much higher than the 11 620 K of the spectroscopy determination. There are also some discrepancies at low temperatures, which can be related to the extent of the outer convection zone.

The agreement between the spectroscopic and asteroseismological effective temperature determination tends to be better than those of log(g) since, as mentioned before, the T_{eff} had been used as a boundary condition. If I gave more weight to the surface gravity in the fitting procedure, the differences in the log(g) determination in the Figure 10 would be, probably, less pronounced, while the differences in the effective temperature in Figure 12 maybe increase.

4.5 The hydrogen envelope distribution

One of the most powerful contributions of asteroseismology for stellar astrophysics is to probe the internal structure of the stars. Although it has some observational evidence of a range in the hydrogen content, this can only be verified in asteroseismological studies. Figure 13 shows the hydrogen envelope thickness distribution of the 40 massive DAV stars

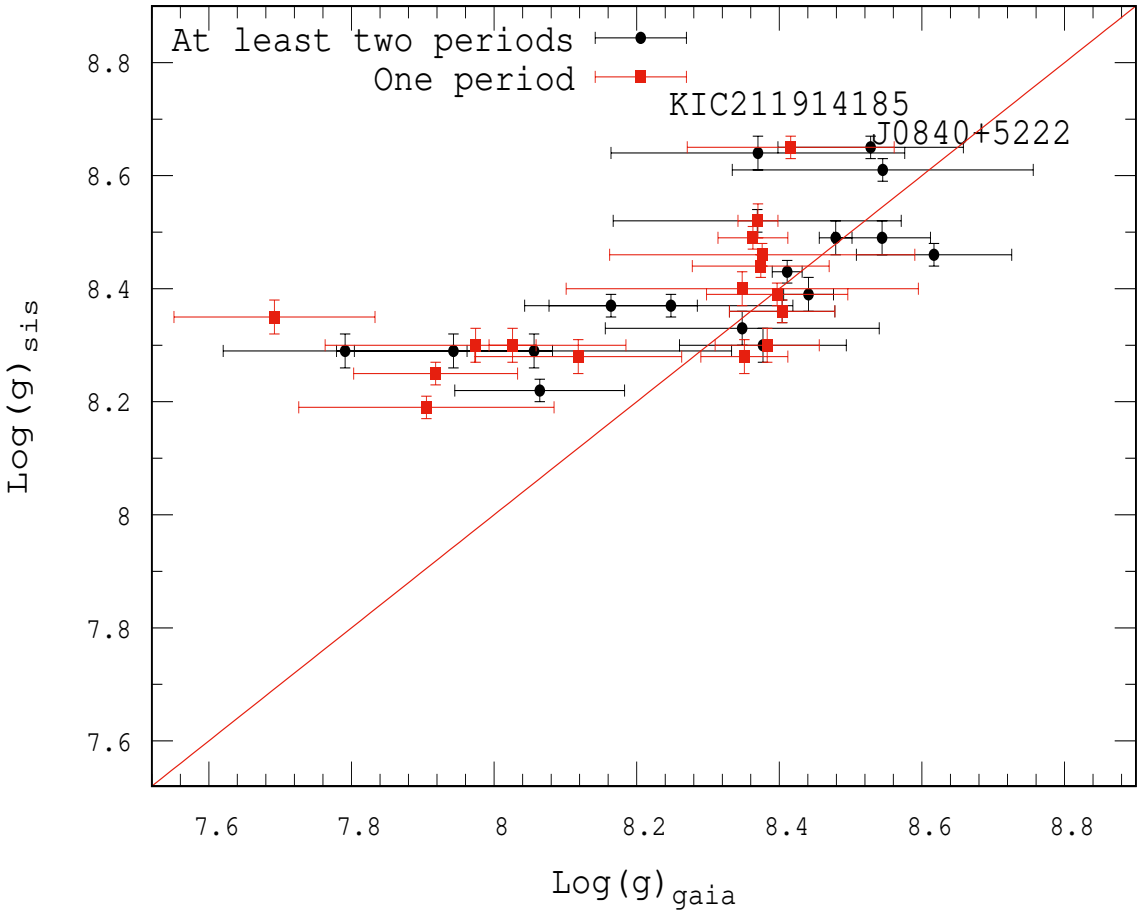

Figure 11 – Comparison between the values of surface gravity according to *Gaia* EDR3 data and asteroseismology for 33 stars of the sample. The red dots represent the stars that have one observed period, while the black dots are those with at least two observed periods. The uncertainties are due to internal errors in the fitting procedure. The red line represents the 1:1 correspondence.

studied in this work, presenting only the best-fit model for each object. The black-dashed bars are the complete sample whereas the red-filled bars are only the stars with at least two observed periods. The horizontal dotted line represents the square root of the number of objects in the sample, $\sqrt{(40)} \approx 6$, being is the expected value for a uniform distribution. This quantity shows how pronounced are the peaks in the distribution. The distribution shows a very pronounced peak at $-\log(M_H/M_\star)$ range 5 to 6 (20 objects), what I consider thick hydrogen envelopes. Of the 40 best-fit models determined in the asteroseismological fits of our sample, only 4 (10%) of them correspond to models with a canonical hydrogen content, i.e., with the hydrogen envelope thickness predicted by the prior evolution. Romero et al. (2013) reported 11 best-fit models with canonical envelopes, representing 26% of their sample, a higher value than found in the present work. These authors used a sample of 42 massive DAV stars with a spectroscopic and asteroseismological mean mass of 0.84 $M_\odot$ and 0.85 $M_\odot$ respectively, which is very similar to our sample. I reinforce, however,

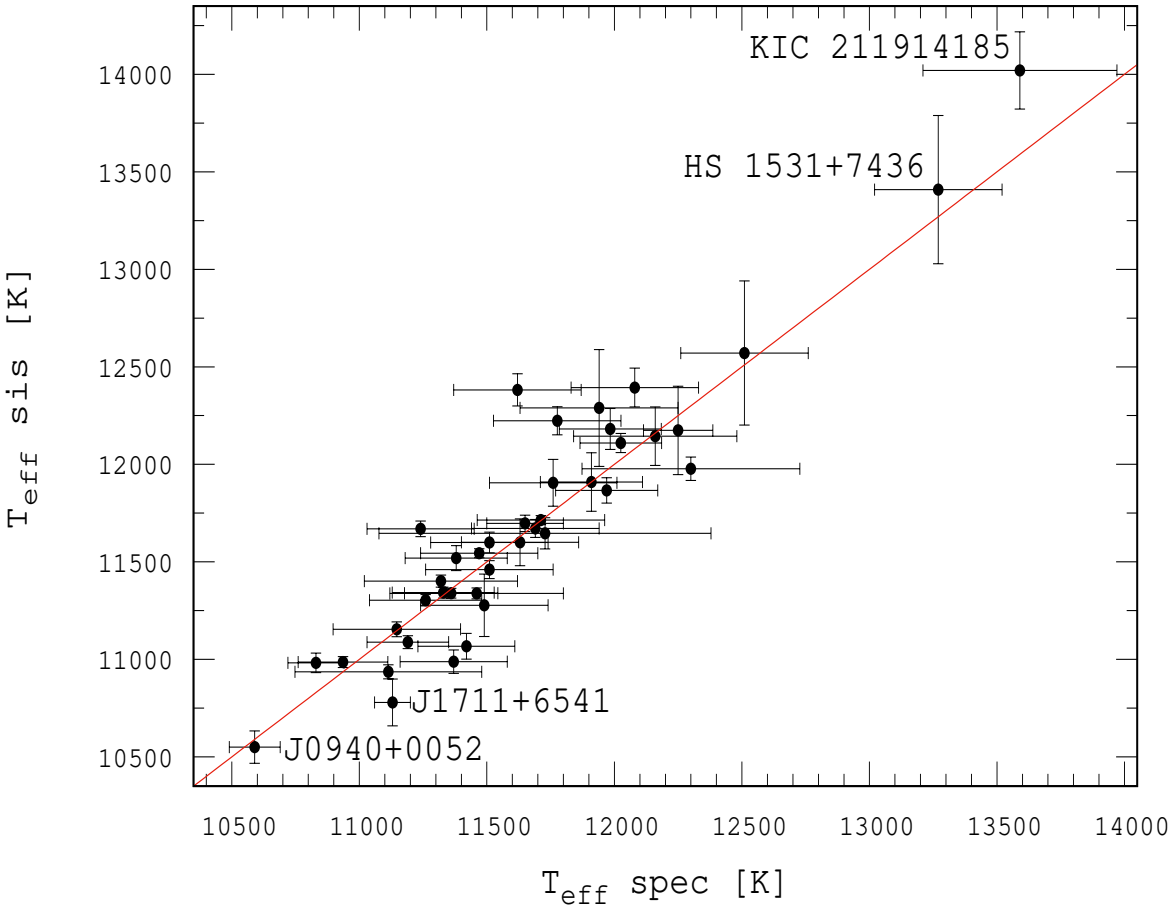

Figure 12 – Comparison between the spectroscopy (x-axis) and the asteroseismological (y-axis) determinations of the effective temperature of 40 ZZ Ceti stars analyzed in this work. The diagonal red line is the 1:1 correspondence.

that the grid used in this work has a higher resolution in hydrogen envelope mass when compared to the grid used in Romero et al. (2013). Thus, it is possible to observe deeper in the hydrogen distribution of the ZZ Ceti stars. Thus, it is possible that the ZZ Ceti stars in the domain of thick envelopes may have less hydrogen than what is expected by the prior evolution.

The smooth pattern of the hydrogen mass distribution depicted in Figure 13, together with the pronounced peak in the $-\log(M_H/M_\star)$ range 5 to 6 is a stimulating result. Around 80% of the spectroscopic identified white dwarf stars are characterized by H-rich atmospheres [24], i.e., with canonical hydrogen envelopes, or near to the canonical values, which is what we see in Figure 13. Indeed, spectroscopic and asteroseismological studies of DA stars shows that 15-20% of the DA stars have thin H-envelopes, $-\log(M_H/M_\star)$ range 6 to 10 [157, 71, 75]. In this work, I found 15 best-fit models characterized with a thinner hydrogen envelope, which represents 38% of our sample of massive DAVs. This value agrees with the result reported in Romero et al. (2013), which found 26 best-fit

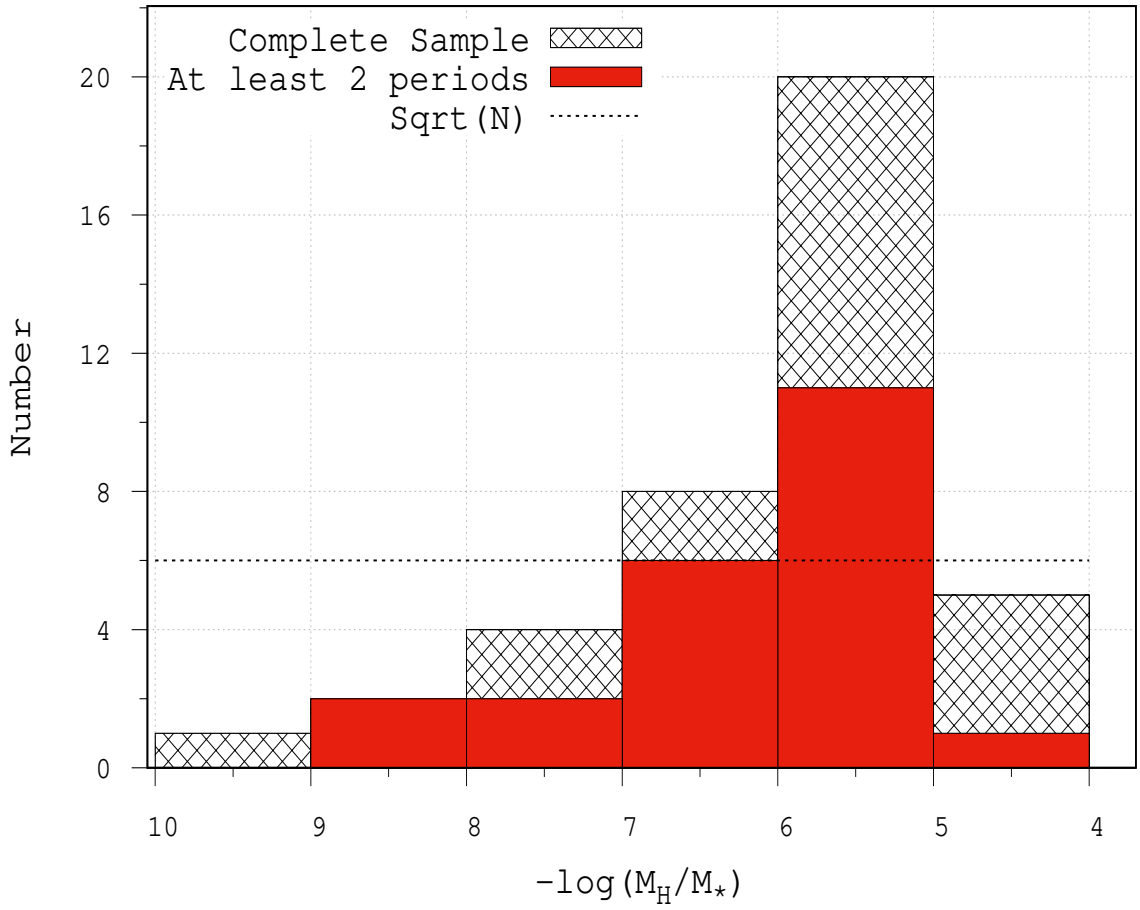

Figure 13 – Histogram showing the hydrogen envelope thickness distribution for the complete sample of 40 massive ZZ Ceti stars (black-dashed) and only for those with at least 2 periods (red-filled).

models (62%) with thin hydrogen envelopes. The presence of a high number of best-fit models with thin hydrogen envelopes in our results, when compared to the 20% expected [157, 71], could be related to the number of objects analyzed in this work. The number of DAV stars known is around 300, thus our sample represents only 13% of the total number. On the other hand, also supported by the work of [76], this could mean that H-deficient stars may not be a minority. Thus, models with thinner hydrogen envelopes cannot be ignored in asteroseismological studies of ZZ Ceti stars, especially when dealing with massive objects.

The mean value of the hydrogen mass of our sample of 40 stars is $\langle M_H \rangle = 9 \times 10^{-7} M_\star$, or $\langle M_H \rangle = 7 \times 10^{-7} M_\star$ if I consider the reduced sample of stars which have at least 2 detected periods. This value is $\sim$ six times lower than the value reported in Romero et al. (2013) and three times lower than the value reported in Romero et al. (2019b), which used a sample that covers a broad range in stellar mass. The $\langle M_H \rangle$ value is, in fact, close to the value reported by Castanheira & Kepler (2009) [71], with our result being 1.75 times

larger. It is important to point out that the grid used by Castanheira & Kepler (2009) was independent of the grid used in this work, with their sample covering a large range in stellar mass. Despite these differences, we all conclude that the possible values for the hydrogen mass left in the envelope of the DAVs span over a large range, from 10^{-4} to $10^{-10}M_{\star}$.

An important work that highlights the existence of H-deficient white dwarfs was carried out by Ourique et al. (2020) [158], who studied the spectral evolution of white dwarfs. The sample used was composed of $\sim$ 13 000 DA and $\sim$ 3 000 non-DA white dwarfs stars, both extracted from the SDSS DR12 catalog and the GAIA DR2 survey. The authors reported that the ratio of non-DA to DA white dwarfs is ~ 0.075 for effective temperatures higher than 22 000 K, increasing five times for effective temperatures below 15 000 K. The most likely explanation is the convective mixing of a thin hydrogen envelope into the underlying helium layer of 14$\pm$3% of DA white dwarfs stars. Another relevant study that proves the existence of H-deficient stars was presented by Romero et al. (2019) [47]. The authors, studying 40 Eridani B compared the theoretical mass-radius relations for different hydrogen envelope masses with the dynamical stellar mass from Mason et al. (2017) [159], and the radius obtained from photometry and distance Bond et al. (2017) [160]. One of their results is that 40 Eridani B have a thin H-envelope, with $M_H = 2.6 \times 10^{-8}M_{\star}$.

The hydrogen content of the DA white dwarfs had also been discussed in the work of Tremblay et al. (2008) [157], which studied the ratio He to H-rich in terms of $T_{\rm eff}$ from a model atmosphere analysis of the infrared photometric data from the Two Micron All Sky Survey combined with available visual magnitudes. These authors conclude that 15% of the DA white dwarfs probably harbor a $-\log(M_H/M_{\star})$ between 8 and 10. The asteroseismological study performed in this work points that 38% of the DAVs should have a hydrogen envelope thinner than the canonical values, with $-\log(M_H/M_{\star})$ between 6 and 10. Particularly, 3 stars analyzed in this work have $10^{-10} \leq M_H/M_{\star} \leq 10^{-8}$, which represents 7.5% of our sample. This result is in agreement with Tremblay et al. (2008) [157], considering that our sample is small and only composed of massive components of the DAV white dwarfs.

5 Conclusions

In this dissertation, I have carried out an asteroseismological study of 40 massive DA variable white dwarfs with spectroscopic masses higher than 0.74 $M_{\odot}$. To this end, I introduce an updated grid of fully evolutionary models characterized by models with a consistent and detailed chemical profile, from the core to the surface. This model grid is an updated version of the grid used in the pioneer works of Romero et al. (2012, 2013, 2019b) [75, 76, 47], which employed for the first time the use of a grid of fully evolutionary models in the asteroseismological fits. For each stellar mass and effective temperature, starting from the canonical value to $\log(M_H/M_\star) = -6$, the updated grid has models spaced in 0.1 in logarithmic scale, from this value on, the sequences have hydrogen masses spaced in 0.5 until our thinner envelope with $\log(M_H/M_\star) = -9.5$. Also, I computed three new sequences for the cooling curve of the white dwarfs (0.82, 0.86, and 0.9 $M_{\odot}$), in order to fill some gaps in the stellar mass present in the grid. Those sequences are the result of an interpolation of the chemical profiles between two evolutionary sequences. The updated grid has $\sim$ 800 sequences for the cooling curve of the white dwarfs, with at least $\sim$ 500 of them being computed in this work. Of the 40 best-fit models selected in the asteroseismological fits, 30 of them (75%) are from new sequences included in the grid, which highlights the importance of having a good resolution in the mass of the hydrogen envelope.

The main results of the asteroseismological fits are the following.

(i) The mean value obtained for the asteroseismological mass is $\langle M_\star \rangle_{\rm sis} = 0.84 \pm 0.04 M_{\odot}$, which it is in excellent agreement with the value obtained for the mean spectroscopic mass $\langle M_\star \rangle_{\rm spec} = 0.84 \pm 0.07 M_{\odot}$. Considering that 40 stars were analyzed, this result is encouraging.

(ii) The mean asteroseismological mass obtained is in good agreement with Kleinman et al. (2013) [161], which reported a mean mass of $\langle M_\star \rangle_{\rm spec} = 0.82 M_{\odot}$ for the massive component of the DA white dwarf stars, including variable and non variable objects.

(iii) I found a smooth distribution for the hydrogen envelopes mass, with a pronounced peak at $-\log(M_H/M_\star)$ range 5 to 6. It is the first time that a smooth distribution is obtained in asteroseismological studies. A range in the thickness of the hydrogen envelope has been also reported in previous works [71, 75, 76, 2].

(iv) For 36 out of the 40 stars analyzed, I have found a best-fit model with less hydrogen than it was predicted by standard evolutionary computations. I found 15 best-fit models characterized with a hydrogen envelope thinner than $-\log(M_H/M_\star) = 6$, which represents 38% of our sample of massive DAVs. It indicates that is possible that the

DAVs in the domain of thick envelopes have less hydrogen than what was expected by the previous evolution.

(v) I found a mean hydrogen envelope mass of $\langle M_H \rangle = 9 \times 10^{-7} M_\star$, 6 times lower than the value reported by Romero et al. (2013). This difference may be due to the higher resolution of our model grid. If I consider only the stars with at least two periods detected, the hydrogen mean mass is $\langle M_H \rangle = 7 \times 10^{-7} M_\star$.

In this work, I obtained a good agreement between the spectroscopic and asteroseismological log(g) values, despite five outliers. This is an encouraging result since the methods used to derive both values are quite different and rely on two independent sets of observational data. This might suggest that solutions were being lost in the fitting procedure because of the lower resolution in M_H. Therefore, considering previous works, the $\sim$500 sequences computed for this work, added with the existing ones (summing $\sim$ 800), improved the agreement between the spectroscopic and seismological log(g) determinations, reducing the dispersion.

In the future may be interesting to analyze the outliers in more detail. The dispersion in the comparison of the asteroseismology and spectroscopic determination of log(g) seems to occur above $\log(g)_{sis}$ 8.5. Thus, the detection followed by the asteroseismological analysis of more objects in this log(g) range could help to identify the problem: this happens because the model grid can not correctly represent the objects in this range of mass? Spectroscopy is not good for these objects? It is also important to note that this range of mass is where could be a change in the core composition. Therefore, the analysis of objects in this range of mass also enables the exploration of the mass range where the core composition of the white dwarf stars changes and perhaps constrain a limit value.

Bibliography

[1] Jeffery, C. S.; Saio, H. Radial pulsation as a function of hydrogen abundance. , v. 458, n. 2, p. 1352–1373, May 2016. Citado 3 vezes nas páginas 17, 33, and 34.

[2] Romero, A. D.; Amaral, L. A.; Klippel, T.; Sanmartim, D.; Fraga, L.; Ourique, G.; Pelisoli, I.; Lauffer, G. R.; Kepler, S. O.; Koester, D. Ground-based observation of ZZ Ceti stars and the discovery of four new variables. , v. 490, n. 2, p. 1803–1820, Dec. 2019. Citado 8 vezes nas páginas 18, 33, 43, 53, 56, 57, 58, and 81.

[3] Bognar, Z.; Sodor, A. White Dwarf Period Tables I. Pulsators with hydrogen-dominated atmospheres. *Information Bulletin on Variable Stars*, v. 6184, p. 1, Sept. 2016. Citado 3 vezes nas páginas 18, 59, and 60.

[4] Su, J.; Fu, J.; Lin, G.; Chen, F.; Khokhuntod, P.; Li, C. New ZZ Ceti Stars from the LAMOST Survey. , v. 847, n. 1, p. 34, Sept. 2017. Citado 4 vezes nas páginas 18, 59, 60, and 67.

[5] Hermes, J. J.; Gänsicke, B. T.; Kawaler, S. D.; Greiss, S.; Tremblay, P. E.; Gentile Fusillo, N. P.; Raddi, R.; Fanale, S. M.; Bell, K. J.; Dennihy, E.; Fuchs, J. T.; Dunlap, B. H.; Clemens, J. C.; Montgomery, M. H.; Winget, D. E.; Chote, P.; Marsh, T. R.; Redfield, S. White Dwarf Rotation as a Function of Mass and a Dichotomy of Mode Line Widths: Kepler Observations of 27 Pulsating DA White Dwarfs through K2 Campaign 8. , v. 232, n. 2, p. 23, Oct. 2017. Citado 6 vezes nas páginas 18, 43, 59, 60, 63, and 71.

[6] Rowan, D. M.; Tucker, M. A.; Shappee, B. J.; Hermes, J. J. Detections and constraints on white dwarf variability from time-series GALEX observations. , v. 486, n. 4, p. 4574–4589, July 2019. Citado 4 vezes nas páginas 18, 59, 60, and 67.

[7] Bell, K. J.; Hermes, J. J.; Vanderbosch, Z.; Montgomery, M. H.; Winget, D. E.; Dennihy, E.; Fuchs, J. T.; Tremblay, P. E. Destroying Aliases from the Ground and Space: Super-Nyquist ZZ Cetis in K2 Long Cadence Data. , v. 851, n. 1, p. 24, Dec. 2017. Citado 2 vezes nas páginas 18 and 60.

[8] Fuchs, J. T. *Fundamental Properties of White Dwarfs Alone and in Binaries*. Jan. 2017. Tese (Doutorado em Física) - The University of North Carolina at Chapel Hill, Jan. 2017. Citado 2 vezes nas páginas 18 and 60.

[9] Curd, B.; Gianninas, A.; Bell, K. J.; Kilic, M.; Romero, A. D.; Allende Prieto, C.; Winget, D. E.; Winget, K. I. Four new massive pulsating white dwarfs including

an ultramassive DAV. , v. 468, n. 1, p. 239–249, June 2017. Citado 5 vezes nas páginas 18, 60, 63, 67, and 71.

[10] Kippenhahn, R.; Weigert, A.; Weiss, A. *Stellar Structure and Evolution*. 2012. Citado na página 27.

[11] Schönberg, M.; Chandrasekhar, S. On the Evolution of the Main-Sequence Stars. , v. 96, p. 161, Sept. 1942. Citado na página 28.

[12] Hayashi, C. Stellar evolution in early phases of gravitational contraction. , v. 13, p. 450–452, Jan. 1961. Citado na página 29.

[13] García-Berro, E.; Ritossa, C.; Iben, ICKO, J. On the Evolution of Stars that Form Electron-Degenerate Cores Processed by Carbon Burning. III. The Inward Propagation of a Carbon-Burning Flame and Other Properties of a 9 M Model Star. , v. 485, n. 2, p. 765–784, Aug. 1997. Citado 4 vezes nas páginas 31, 32, 60, and 70.

[14] Woosley, S. E.; Heger, A. The Remarkable Deaths of 9-11 Solar Mass Stars. , v. 810, n. 1, p. 34, Sept. 2015. Citado na página 31.

[15] Doherty, C. L.; Gil-Pons, P.; Siess, L.; Lattanzio, J. C.; Lau, H. H. B. Super- and massive AGB stars - IV. Final fates - initial-to-final mass relation. , v. 446, n. 3, p. 2599–2612, Jan. 2015. Citado 4 vezes nas páginas 31, 32, 60, and 70.

[16] Lauffer, G. R.; Romero, A. D.; Kepler, S. O. New full evolutionary sequences of H- and He-atmosphere massive white dwarf stars using MESA. , v. 480, n. 2, p. 1547–1562, Oct. 2018. Citado 4 vezes nas páginas 31, 32, 60, and 70.

[17] Salpeter, E. E. The Luminosity Function and Stellar Evolution. , v. 121, p. 161, Jan. 1955. Citado na página 31.

[18] Althaus, L. G.; Gil Pons, P.; Córsico, A. H.; Miller Bertolami, M.; De Gerónimo, F.; Camisassa, M. E.; Torres, S.; Gutierrez, J.; Rebassa-Mansergas, A. The formation of ultra-massive carbon-oxygen core white dwarfs and their evolutionary and pulsational properties. *arXiv e-prints*, p. arXiv:2011.10439, Nov. 2020. Citado 2 vezes nas páginas 32 and 60.

[19] Schoenberner, D. Asymptotic giant branch evolution with steady mass loss. , v. 79, p. 108–114, Oct. 1979. Citado na página 32.

[20] Iben, I., J. On the frequency of planetary nebula nuclei powered by helium burningand on the frequency of white dwarfs with hydrogen-deficient atmospheres. , v. 277, p. 333–354, Feb. 1984. Citado na página 32.

[21] D'Antona, F.; Mazzitelli, I. Cooling of white dwarfs. , v. 28, p. 139–181, Jan. 1990. Citado na página 32.

[22] Herwig, F.; Blöcker, T.; Langer, N.; Driebe, T. On the formation of hydrogen-deficient post-AGB stars. , v. 349, p. L5–L8, Sept. 1999. Citado na página 32.

[23] Blöcker, T. Evolution on the AGB and beyond: on the formation of H-deficient post-AGB stars. , v. 275, p. 1–14, Jan. 2001. Citado na página 32.

[24] Córsico, A. H.; Althaus, L. G.; Miller Bertolami, M. M.; Kepler, S. O. Pulsating white dwarfs: new insights. , v. 27, n. 1, p. 7, Sept. 2019. Citado 7 vezes nas páginas 32, 33, 39, 40, 42, 59, and 77.

[25] Althaus, L. G.; Córsico, A. H.; Isern, J.; García-Berro, E. Evolutionary and pulsational properties of white dwarf stars. , v. 18, n. 4, p. 471–566, Oct. 2010. Citado 3 vezes nas páginas 32, 33, and 47.

[26] Siess, L. Evolution of massive AGB stars. II. model properties at non-solar metallicity and the fate of Super-AGB stars. , v. 476, n. 2, p. 893–909, Dec. 2007. Citado na página 33.

[27] Catalán, S.; Isern, J.; García-Berro, E.; Ribas, I. The initial-final mass relationship of white dwarfs revisited: effect on the luminosity function and mass distribution. , v. 387, n. 4, p. 1693–1706, July 2008. Citado na página 33.

[28] Hansen, B. M. S.; Anderson, J.; Brewer, J.; Dotter, A.; Fahlman, G. G.; Hurley, J.; Kalirai, J.; King, I.; Reitzel, D.; Richer, H. B.; Rich, R. M.; Shara, M. M.; Stetson, P. B. The White Dwarf Cooling Sequence of NGC 6397. , v. 671, n. 1, p. 380–401, Dec. 2007. Citado na página 33.

[29] Campos, F.; Bergeron, P.; Romero, A. D.; Kepler, S. O.; Ourique, G.; Costa, J. E. S.; Bonatto, C. J.; Winget, D. E.; Montgomery, M. H.; Pacheco, T. A.; Bedin, L. R. A comparative analysis of the observed white dwarf cooling sequence from globular clusters. , v. 456, n. 4, p. 3729–3742, Mar. 2016. Citado na página 33.

[30] Winget, D. E.; Hansen, C. J.; Liebert, J.; van Horn, H. M.; Fontaine, G.; Nather, R. E.; Kepler, S. O.; Lamb, D. Q. An Independent Method for Determining the Age of the Universe. , v. 315, p. L77, Apr. 1987. Citado na página 33.

[31] García-Berro, E.; Torres, S.; Althaus, L. G.; Miller Bertolami, M. M. The white dwarf cooling sequence of 47 Tucanae. , v. 571, p. A56, Nov. 2014. Citado na página 33.

[32] Wang, B.; Podsiadlowski, P.; Han, Z. He-accreting carbon-oxygen white dwarfs and Type Ia supernovae. , v. 472, n. 2, p. 1593–1599, Dec. 2017. Citado na página 33.

[33] Prada Moroni, P. G.; Straniero, O. Calibration of White Dwarf Cooling Sequences: Theoretical Uncertainty. , v. 581, n. 1, p. 585–597, Dec. 2002. Citado 2 vezes nas páginas 33 and 50.

[34] Isern, J.; Catalan, S.; Garcia-Berro, E.; Salaris, M.; Torres, S. Axions and White Dwarfs. *arXiv e-prints*, p. arXiv:1010.5351, Oct. 2010. Citado 2 vezes nas páginas 33 and 41.

[35] Kepler, S. O.; Giovannini, O.; Wood, M. A.; Nather, R. E.; Winget, D. E.; Kanaan, A.; Kleinman, S. J.; Bradley, P. A.; Provencal, J. L.; Clemens, J. C.; Claver, C. F.; Watson, T. K.; Yanagida, K.; Krisciunas, K.; Marar, T. M. K.; Seetha, S.; Ashoka, B. N.; Leibowitz, E.; Mendelson, H.; Mazeh, T.; Moskalik, P.; Krzesinski, J.; Pajdosz, G.; Zola, S.; Solheim, J. E.; Emanuelsen, P. I.; Dolez, N.; Vauclair, G.; Chevreton, M.; Fremy, J. R.; Barstow, M. A.; Sansom, A. E.; Tweedy, R. W.; Wickramasinghe, D. T.; Ferrario, L.; Sullivan, D. J.; van der Peet, A. J.; Buckley, D. A. H.; Chen, A. L. Whole Earth Telescope Observations of the DAV White Dwarf G226-29. , v. 447, p. 874, July 1995. Citado 2 vezes nas páginas 33 and 67.

[36] Winget, D. E.; Kepler, S. O. Pulsating white dwarf stars and precision asteroseismology. , v. 46, p. 157–199, Sept. 2008. Citado 2 vezes nas páginas 33 and 39.

[37] Fontaine, G.; Brassard, P. The Pulsating White Dwarf Stars. , v. 120, n. 872, p. 1043, Oct. 2008. Citado 2 vezes nas páginas 33 and 39.

[38] Cowling, T. G. The non-radial oscillations of polytropic stars. , v. 101, p. 367, Jan. 1941. Citado 2 vezes nas páginas 34 and 37.

[39] Cox, J. P. *Theory of stellar pulsation*. 1980. Citado 2 vezes nas páginas 35 and 38.

[40] Unno, W.; Osaki, Y.; Ando, H.; Saio, H.; Shibahashi, H. *Nonradial oscillations of stars*. 1989. Citado 4 vezes nas páginas 35, 36, 37, and 38.

[41] Citado na página 39.

[42] Warner, B.; van Zyl, L. Discovery of non-radial pulsations in the white dwarf primary of a cataclysmic variable star. In: . Editors Deubner, F.-L.; Christensen-Dalsgaard, J.; Kurtz, D. c1998. v. 185. p. 321. Citado na página 40.

[43] Maxted, P. F. L.; Serenelli, A. M.; Miglio, A.; Marsh, T. R.; Heber, U.; Dhillon, V. S.; Littlefair, S.; Copperwheat, C.; Smalley, B.; Breedt, E.; Schaffenroth, V. Multi-periodic pulsations of a stripped red-giant star in an eclipsing binary system. , v. 498, n. 7455, p. 463–465, June 2013. Citado na página 40.

[44] Shibahashi, H. The DB gap and pulsations of white dwarfs. In: . Editors Alecian, G.; Richard, O.; Vauclair, S. c2005. v. 17 of *EAS Publications Series*. p. 143–148. Citado 2 vezes nas páginas 40 and 55.

[45] Shibahashi, H. The DB Gap and Pulsations of White Dwarfs. In: . Editors Stancliffe, R. J.; Houdek, G.; Martin, R. G.; Tout, C. A. c2007. v. 948 of *American Institute of Physics Conference Series*. p. 35–42. Citado 2 vezes nas páginas 40 and 55.

[46] Landolt, A. U. A New Short-Period Blue Variable. , v. 153, p. 151, July 1968. Citado na página 40.

[47] Romero, A. D.; Kepler, S. O.; Joyce, S. R. G.; Lauffer, G. R.; Córsico, A. H. The white dwarf mass-radius relation and its dependence on the hydrogen envelope. , v. 484, n. 2, p. 2711–2724, Apr. 2019. Citado 4 vezes nas páginas 40, 42, 79, and 81.

[48] Vincent, O.; Bergeron, P.; Lafrenière, D. Searching for ZZ Ceti white dwarfs in the Gaia survey. *IAU Symposium*, v. 357, p. 123–126, Jan. 2020. Citado na página 40.

[49] Clemens, J. C. The pulsation properties of the DA white dwarf variables. *Baltic Astronomy*, v. 2, p. 407–434, Jan. 1993. Citado na página 40.

[50] Mukadam, A. S.; Montgomery, M. H.; Winget, D. E.; Kepler, S. O.; Clemens, J. C. Ensemble Characteristics of the ZZ Ceti Stars. , v. 640, n. 2, p. 956–965, Apr. 2006. Citado 2 vezes nas páginas 40 and 65.

[51] Metcalfe, T. S. A deeper understanding of white dwarf interiors. , v. 363, n. 1, p. L86–L90, Oct. 2005. Citado na página 41.

[52] Córsico, A. H.; Althaus, L. G.; Montgomery, M. H.; García-Berro, E. The Effects of Crystallization on the Pulsational Properties of Massive ZZ Ceti Stars. In: . Editors Koester, D.; Moehler, S. c2005. v. 334 of *Astronomical Society of the Pacific Conference Series*. p. 537. Citado 2 vezes nas páginas 41 and 52.

[53] Kanaan, A.; Nitta, A.; Winget, D. E.; Kepler, S. O.; Montgomery, M. H.; Metcalfe, T. S.; Oliveira, H.; Fraga, L.; da Costa, A. F. M.; Costa, J. E. S.; Castanheira, B. G.; Giovannini, O.; Nather, R. E.; Mukadam, A.; Kawaler, S. D.; O'Brien, M. S.; Reed, M. D.; Kleinman, S. J.; Provencal, J. L.; Watson, T. K.; Kilkenny, D.; Sullivan, D. J.; Sullivan, T.; Shobbrook, B.; Jiang, X. J.; Ashoka, B. N.; Seetha, S.; Leibowitz, E.; Ibbetson, P.; Mendelson, H.; Meištas, E. G.; Kalytis, R.; Ališauskas, D.; O'Donoghue, D.; Buckley, D.; Martinez, P.; van Wyk, F.; Stobie, R.; Marang, F.; van Zyl, L.; Ogloza, W.; Krzesinski, J.; Zola, S.; Moskalik, P.; Breger, M.; Stankov, A.; Silvotti, R.; Piccioni, A.; Vauclair, G.; Dolez, N.; Chevreton, M.; Deetjen, J.; Dreizler, S.; Schuh, S.; Gonzalez Perez, J. M.; Østensen, R.; Ulla, A.; Manteiga, M.; Suarez, O.; Burleigh, M. R.; Barstow, M. A. Whole Earth Telescope observations of BPM

37093: A seismological test of crystallization theory in white dwarfs. , v. 432, n. 1, p. 219–224, Mar. 2005. Citado 3 vezes nas páginas 41, 64, and 70.

[54] Winget, D. E.; Kepler, S. O.; Campos, F.; Montgomery, M. H.; Girardi, L.; Bergeron, P.; Williams, K. The Physics of Crystallization From Globular Cluster White Dwarf Stars in NGC 6397. , v. 693, n. 1, p. L6–L10, Mar. 2009. Citado 2 vezes nas páginas 41 and 51.

[55] Winget, D. E.; Sullivan, D. J.; Metcalfe, T. S.; Kawaler, S. D.; Montgomery, M. H. A Strong Test of Electroweak Theory Using Pulsating DB White Dwarf Stars as Plasmon Neutrino Detectors. , v. 602, n. 2, p. L109–L112, Feb. 2004. Citado na página 41.

[56] Córsico, A. H.; Benvenuto, O. G.; Althaus, L. R. G.; Isern, J.; García-Berro, E. The potential of the variable DA white dwarf G117-B15A as a tool for fundamental physics. , v. 6, n. 4, p. 197–213, June 2001. Citado na página 41.

[57] Bischoff-Kim, A.; Montgomery, M. H.; Winget, D. E. Fine Grid Asteroseismology of G117-B15A and R548. , v. 675, n. 2, p. 1505–1511, Mar. 2008. Citado 2 vezes nas páginas 41 and 42.

[58] Córsico, A. H.; Romero, A. D.; Althaus, L. R. G.; García-Berro, E.; Isern, J.; Kepler, S. O.; Miller Bertolami, M. M.; Sullivan, D. J.; Chote, P. An asteroseismic constraint on the mass of the axion from the period drift of the pulsating DA white dwarf star L19-2. , v. 2016, n. 7, p. 036, July 2016. Citado na página 41.

[59] Montgomery, M. H. White Dwarf Lightcurves: Constraining Convection and Mode Identification Using Non-sinusoidal Lightcurves. In: . Editors Koester, D.; Moehler, S. c2005. v. 334 of *Astronomical Society of the Pacific Conference Series*. p. 483. Citado na página 41.

[60] Montgomery, M. H. Convection: A Seismological Perspective. In: . Editors Stancliffe, R. J.; Houdek, G.; Martin, R. G.; Tout, C. A. c2007. v. 948 of *American Institute of Physics Conference Series*. p. 99–110. Citado na página 41.

[61] Tassoul, M.; Fontaine, G.; Winget, D. E. Evolutionary Models for Pulsation Studies of White Dwarfs. , v. 72, p. 335, Feb. 1990. Citado 2 vezes nas páginas 41 and 52.

[62] Brassard, P.; Fontaine, G.; Wesemael, F.; Kawaler, S. D.; Tassoul, M. Adiabatic Properties of Pulsating DA White Dwarfs. I. The Treatment of the Brunt-Vaeisaelae Frequency and the Region of Period Formation. , v. 367, p. 601, Feb. 1991. Citado 2 vezes nas páginas 41 and 51.

[63] Brassard, P.; Fontaine, G.; Wesemael, F.; Hansen, C. J. Adiabatic Properties of Pulsating DA White Dwarfs. II. Mode Trapping in Compositionally Stratified Models. , v. 80, p. 369, May 1992. Citado na página 41.

[64] Brassard, P.; Fontaine, G.; Wesemael, F.; Tassoul, M. Adiabatic Properties of Pulsating DA White Dwarfs. IV. an Extensive Survey of the Period Structure of Evolutionary Models. , v. 81, p. 747, Aug. 1992. Citado na página 41.

[65] Córsico, A. H.; Benvenuto, O. G.; Althaus, L. G.; Serenelli, A. M. The effects of element diffusion on the pulsational properties of variable DA white dwarf stars. , v. 332, n. 2, p. 392–398, May 2002. Citado 2 vezes nas páginas 42 and 51.

[66] Córsico, A. H.; Althaus, L. G.; Benvenuto, O. G.; Serenelli, A. M. The mode trapping properties of full DA white dwarf evolutionary models. , v. 387, p. 531–549, May 2002. Citado na página 42.

[67] Benvenuto, O. G.; Córsico, A. H.; Althaus, L. G.; Serenelli, A. M. Time-dependent diffusion in pulsating white dwarf stars: asteroseismology of G117-B15A. , v. 332, n. 2, p. 399–408, May 2002. Citado na página 42.

[68] Althaus, L. G.; Benvenuto, O. G. Diffusion in helium white dwarf stars. , v. 317, n. 4, p. 952–964, Oct. 2000. Citado na página 42.

[69] Salaris, M.; Domínguez, I.; García-Berro, E.; Hernanz, M.; Isern, J.; Mochkovitch, R. The Cooling of CO White Dwarfs: Influence of the Internal Chemical Distribution. , v. 486, n. 1, p. 413–419, Sept. 1997. Citado 2 vezes nas páginas 42 and 50.

[70] Castanheira, B. G.; Kepler, S. O. Seismological studies of ZZ Ceti stars - I. The model grid and the application to individual stars. , v. 385, n. 1, p. 430–444, Mar. 2008. Citado 2 vezes nas páginas 42 and 61.

[71] Castanheira, B. G.; Kepler, S. O. Seismological studies of ZZ Ceti stars - II. Application to the ZZ Ceti class. , v. 396, n. 3, p. 1709–1731, July 2009. Citado 6 vezes nas páginas 42, 66, 67, 77, 78, and 81.

[72] Bischoff-Kim, A.; Østensen, R. H. Asteroseismology of the Kepler Field DBV White Dwarf. It is a Hot One. , v. 742, n. 1, p. L16, Nov. 2011. Citado na página 42.

[73] Bischoff-Kim, A.; Østensen, R. H.; Hermes, J. J.; Provencal, J. L. Seven-period Asteroseismic Fit of the Kepler DBV. , v. 794, n. 1, p. 39, Oct. 2014. Citado na página 42.

[74] Giammichele, N.; Fontaine, G.; Brassard, P.; Charpinet, S. A New Analysis of the Two Classical ZZ Ceti White Dwarfs GD 165 and Ross 548. II. Seismic Modeling. , v. 223, n. 1, p. 10, Mar. 2016. Citado na página 42.

[75] Romero, A. D.; Córsico, A. H.; Althaus, L. G.; Kepler, S. O.; Castanheira, B. G.; Miller Bertolami, M. M. Toward ensemble asteroseismology of ZZ Ceti stars with fully evolutionary models. , v. 420, n. 2, p. 1462–1480, Feb. 2012. Citado 6 vezes nas páginas 42, 53, 56, 58, 77, and 81.

[76] Romero, A. D.; Kepler, S. O.; Córsico, A. H.; Althaus, L. G.; Fraga, L. Asteroseismological Study of Massive ZZ Ceti Stars with Fully Evolutionary Models. , v. 779, n. 1, p. 58, Dec. 2013. Citado 12 vezes nas páginas 42, 43, 47, 53, 58, 59, 63, 64, 65, 69, 78, and 81.

[77] Córsico, A. H.; De Gerónimo, F. C.; Camisassa, M. E.; Althaus, L. G. Asteroseismological analysis of the ultra-massive ZZ Ceti stars BPM 37093, GD 518, and SDSS J0840+5222. , v. 632, p. A119, Dec. 2019. Citado 2 vezes nas páginas 42 and 70.

[78] De Gerónimo, F. C.; Althaus, L. G.; Córsico, A. H.; Romero, A. D.; Kepler, S. O. Asteroseismology of ZZ Ceti stars with fully evolutionary white dwarf models. I. The impact of the uncertainties from prior evolution on the period spectrum. , v. 599, p. A21, Mar. 2017. Citado 2 vezes nas páginas 42 and 56.

[79] Kepler, S. O.; Robinson, E. L.; Nather, R. E.; McGraw, J. T. The pulsating white dwarf G 117-B15A. , v. 254, p. 676–682, Mar. 1982. Citado na página 42.

[80] Bradley, P. A. Asteroseismological Constraints on the Structure of the ZZ Ceti Stars G117-B15A and R548. , v. 116, n. 2, p. 307–319, June 1998. Citado 2 vezes nas páginas 42 and 51.

[81] Kepler, S. O.; Costa, J. E. S.; Castanheira, B. G.; Winget, D. E.; Mullally, F.; Nather, R. E.; Kilic, M.; von Hippel, T.; Mukadam, A. S.; Sullivan, D. J. Measuring the Evolution of the Most Stable Optical Clock G 117-B15A. , v. 634, n. 2, p. 1311–1318, Dec. 2005. Citado 3 vezes nas páginas 42, 65, and 67.

[82] Córsico, A. H.; Althaus, L. G.; Romero, A. D.; Miller Bertolami, M. M.; García-Berro, E.; Isern, J. Constraining the Axion Mass through the Asteroseismology of the ZZ Ceti Star G117-B15A. In: . Editors Shibahashi, H.; Takata, M.; Lynas-Gray, A. E. c2012. v. 462 of *Astronomical Society of the Pacific Conference Series*. p. 533. Citado na página 42.

[83] Kepler, S. O.; Winget, D. E.; Vanderbosch, Z. P.; Castanheira, B. G.; Hermes, J. J.; Bell, K. J.; Mullally, F.; Romero, A. D.; Montgomery, M. H.; DeGennaro, S.; Winget, K. I.; Chandler, D.; Jeffery, E. J.; Fritzen, J. K.; Williams, K. A.; Chote, P.; Zola, S. The Pulsating White Dwarf G117-B15A: Still the Most Stable Optical Clock Known. , v. 906, n. 1, p. 7, Jan. 2021. Citado na página 42.

[84] Horowitz, C. J.; Schneider, A. S.; Berry, D. K. Crystallization of Carbon-Oxygen Mixtures in White Dwarf Stars. , v. 104, n. 23, p. 231101, June 2010. Citado 2 vezes nas páginas 43 and 51.

[85] Tremblay, P. E.; Ludwig, H. G.; Steffen, M.; Freytag, B. Spectroscopic analysis of DA white dwarfs with 3D model atmospheres. , v. 559, p. A104, Nov. 2013. Citado 2 vezes nas páginas 43 and 58.

[86] Tremblay, P. E.; Cukanovaite, E.; Gentile Fusillo, N. P.; Cunningham, T.; Hollands, M. A. Fundamental parameter accuracy of DA and DB white dwarfs in Gaia Data Release 2. , v. 482, n. 4, p. 5222–5232, Feb. 2019. Citado na página 43.

[87] Romero, A. D.; Córsico, A. H.; Castanheira, B. G.; De Gerónimo, F. C.; Kepler, S. O.; Koester, D.; Kawka, A.; Althaus, L. G.; Hermes, J. J.; Bonato, C.; Gianninas, A. Probing the Structure of Kepler ZZ Ceti Stars with Full Evolutionary Models-based Asteroseismology. , v. 851, n. 1, p. 60, Dec. 2017. Citado na página 43.

[88] Ricker, G. R.; Winn, J. N.; Vanderspek, R.; Latham, D. W.; Bakos, G. Á.; Bean, J. L.; Berta-Thompson, Z. K.; Brown, T. M.; Buchhave, L.; Butler, N. R.; Butler, R. P.; Chaplin, W. J.; Charbonneau, D.; Christensen-Dalsgaard, J.; Clampin, M.; Deming, D.; Doty, J.; De Lee, N.; Dressing, C.; Dunham, E. W.; Endl, M.; Fressin, F.; Ge, J.; Henning, T.; Holman, M. J.; Howard, A. W.; Ida, S.; Jenkins, J.; Jernigan, G.; Johnson, J. A.; Kaltenegger, L.; Kawai, N.; Kjeldsen, H.; Laughlin, G.; Levine, A. M.; Lin, D.; Lissauer, J. J.; MacQueen, P.; Marcy, G.; McCullough, P. R.; Morton, T. D.; Narita, N.; Paegert, M.; Palle, E.; Pepe, F.; Pepper, J.; Quirrenbach, A.; Rinehart, S. A.; Sasselov, D.; Sato, B.; Seager, S.; Sozzetti, A.; Stassun, K. G.; Sullivan, P.; Szentgyorgyi, A.; Torres, G.; Udry, S.; Villasenor, J. Transiting Exoplanet Survey Satellite (TESS). In: . c2014. v. 9143 of *Society of Photo-Optical Instrumentation Engineers (SPIE) Conference Series*. p. 914320. Citado na página 43.

[89] Bell, K. J.; Kosakowski, A.; Kilic, M.; Green, E. M.; Latour, M.; Baran, A. S.; Charpinet, S.; Handler, G.; Pelisoli, I.; Ratzloff, J. K.; Silvotti, R. A Hot Subdwarf B Star Eclipsed by a Low-mass White Dwarf in TESS Data. *Research Notes of the American Astronomical Society*, v. 3, n. 6, p. 81, June 2019. Citado na página 43.

[90] Althaus, L. G.; Serenelli, A. M.; Panei, J. A.; Córsico, A. H.; García-Berro, E.; Scóccola, C. G. The formation and evolution of hydrogen-deficient post-AGB white dwarfs: The emerging chemical profile and the expectations for the PG 1159-DB-DQ evolutionary connection. , v. 435, n. 2, p. 631–648, May 2005. Citado na página 47.

[91] Renedo, I.; Althaus, L. G.; Miller Bertolami, M. M.; Romero, A. D.; Córsico, A. H.; Rohrmann, R. D.; García-Berro, E. New Cooling Sequences for Old White Dwarfs. , v. 717, n. 1, p. 183–195, July 2010. Citado na página 47.

[92] Romero, A. D.; Campos, F.; Kepler, S. O. The age-metallicity dependence for white dwarf stars. , v. 450, n. 4, p. 3708–3723, July 2015. Citado na página 47.

[93] Miller Bertolami, M. M. New models for the evolution of post-asymptotic giant branch stars and central stars of planetary nebulae. , v. 588, p. A25, Apr. 2016. Citado na página 47.

[94] Althaus, L. G.; Panei, J. A.; Miller Bertolami, M. M.; García-Berro, E.; Córsico, A. H.; Romero, A. D.; Kepler, S. O.; Rohrmann, R. D. New Evolutionary Sequences for Hot H-Deficient White Dwarfs on the Basis of a Full Account of Progenitor Evolution. , v. 704, n. 2, p. 1605–1615, Oct. 2009. Citado na página 47.

[95] Battich, T.; Althaus, L. G.; Córsico, A. R. H. On the formation of hydrogen-deficient low-mass white dwarfs. *arXiv e-prints*, p. arXiv:2003.13602, Mar. 2020. Citado na página 47.

[96] Miller Bertolami, M. M.; Althaus, L. G.; Unglaub, K.; Weiss, A. Modeling He-rich subdwarfs through the hot-flasher scenario. , v. 491, n. 1, p. 253–265, Nov. 2008. Citado na página 47.

[97] Romero, A. D.; Córsico, A. H.; Althaus, L. G.; Pelisoli, I.; Kepler, S. O. On the evolutionary status and pulsations of the recently discovered blue large-amplitude pulsators (BLAPs). , v. 477, n. 1, p. L30–L34, June 2018. Citado na página 47.

[98] Córsico, A. H.; De Gerónimo, F. C.; Camisassa, M. E.; Althaus, L. G. New fully evolutionary models for asteroseismology of ultra-massive white dwarf stars. *arXiv e-prints*, p. arXiv:2001.00671, Jan. 2020. Citado na página 47.

[99] Kippenhahn, R.; Weigert, A. *Stellar Structure and Evolution*. 1990. Citado na página 48.

[100] Iglesias, C. A.; Rogers, F. J. Updated Opal Opacities. , v. 464, p. 943, June 1996. Citado na página 49.

[101] Alexander, D. R.; Ferguson, J. W. Low-Temperature Rosseland Opacities. , v. 437, p. 879, Dec. 1994. Citado na página 49.

[102] Cassisi, S.; Potekhin, A. Y.; Pietrinferni, A.; Catelan, M.; Salaris, M. Updated Electron-Conduction Opacities: The Impact on Low-Mass Stellar Models. , v. 661, n. 2, p. 1094–1104, June 2007. Citado na página 49.

[103] Itoh, N.; Hayashi, H.; Nishikawa, A.; Kohyama, Y. Neutrino Energy Loss in Stellar Interiors. VII. Pair, Photo-, Plasma, Bremsstrahlung, and Recombination Neutrino Processes. , v. 102, p. 411, Feb. 1996. Citado na página 49.

[104] Haft, M.; Raffelt, G.; Weiss, A. Standard and Nonstandard Plasma Neutrino Emission Revisited. , v. 425, p. 222, Apr. 1994. Citado na página 49.

[105] Althaus, L. G.; Miller Bertolami, M. M.; Córsico, A. H.; García-Berro, E.; Gil-Pons, P. The formation of DA white dwarfs with thin hydrogen envelopes. , v. 440, n. 1, p. L1–L4, Sept. 2005. Citado na página 50.

[106] Herwig, F.; Bloecker, T.; Schoenberner, D.; El Eid, M. Stellar evolution of low and intermediate-mass stars. IV. Hydrodynamically-based overshoot and nucleosynthesis in AGB stars. , v. 324, p. L81–L84, Aug. 1997. Citado na página 50.

[107] Straniero, O.; Domínguez, I.; Imbriani, G.; Piersanti, L. The Chemical Composition of White Dwarfs as a Test of Convective Efficiency during Core Helium Burning. , v. 583, n. 2, p. 878–884, Feb. 2003. Citado na página 50.

[108] Schröder, K. P.; Cuntz, M. A New Version of Reimers' Law of Mass Loss Based on a Physical Approach. , v. 630, n. 1, p. L73–L76, Sept. 2005. Citado na página 50.

[109] Vassiliadis, E.; Wood, P. R. Evolution of Low- and Intermediate-Mass Stars to the End of the Asymptotic Giant Branch with Mass Loss. , v. 413, p. 641, Aug. 1993. Citado na página 50.

[110] Magni, G.; Mazzitelli, I. Thermodynamic properties and equations of state for hydrogen and helium in stellar conditions. , v. 72, n. 1-2, p. 134–147, Feb. 1979. Citado na página 50.

[111] Althaus, L. G.; García-Berro, E.; Isern, J.; Córsico, A. H.; Rohrmann, R. D. The age and colors of massive white dwarf stars. , v. 465, n. 1, p. 249–255, Apr. 2007. Citado na página 50.

[112] Burgers, J. M. *Flow Equations for Composite Gases*. 1969. Citado na página 50.

[113] Althaus, L. G.; Serenelli, A. M.; Córsico, A. H.; Montgomery, M. H. New evolutionary models for massive ZZ Ceti stars. I. First results for their pulsational properties. , v. 404, p. 593–609, June 2003. Citado na página 50.

[114] van Horn, H. M. Crystallization of White Dwarfs. , v. 151, p. 227, Jan. 1968. Citado na página 51.

[115] Garcia-Berro, E.; Hernanz, M.; Mochkovitch, R.; Isern, J. Theoretical white-dwarf luminosity functions for two phase diagrams of the carbon-oxygen dense plasma. , v. 193, p. 141–147, Mar. 1988. Citado na página 51.

[116] Garcia-Berro, E.; Hernanz, M.; Isern, J.; Mochkovitch, R. Properties of high-density binary mixtures and the age of the Universe from white dwarf stars. , v. 333, n. 6174, p. 642–644, June 1988. Citado na página 51.

[117] Córsico, A. H. *Pulsaciones en Estrellas Enanas Blancas Variables ZZ Ceti*. Feb. 2003. Tese (Doutorado em Física) - Universidad Nacional de La Plata, Feb. 2003. Citado na página 51.

[118] Kippenhahn, R.; Weigert, A.; Hofmeister, E. Methods for Calculating Stellar Evolution. *Methods in Computational Physics*, v. 7, p. 129–190, Jan. 1967. Citado na página 51.

[119] Montgomery, M. H.; Winget, D. E. The Effect of Crystallization on the Pulsations of White Dwarf Stars. , v. 526, n. 2, p. 976–990, Dec. 1999. Citado na página 52.

[120] Córsico, A. H.; Althaus, L. G. Asteroseismic inferences on GW Virginis variable stars in the frame of new PG 1159 evolutionary models. , v. 454, n. 3, p. 863–881, Aug. 2006. Citado na página 52.

[121] Althaus, L. G.; Camisassa, M. E.; Miller Bertolami, M. M.; Córsico, A. H.; García-Berro, E. White dwarf evolutionary sequences for low-metallicity progenitors: The impact of third dredge-up. , v. 576, p. A9, Apr. 2015. Citado na página 53.

[122] Romero, A. D.; Antunes Amaral, L.; Kepler, S. O.; Fraga, L.; Kurtz, D.; Shibahashi, H. Pulsation in the white dwarf HE 1017-1352: confirmation of the class of hot DAV stars. , v. 497, n. 1, p. L24–L29, June 2020. Citado na página 55.

[123] Kepler, S. O.; Pelisoli, I.; Peçanha, V.; Costa, J. E. S.; Fraga, L.; Hermes, J. J.; Winget, D. E.; Castanheira, B.; Córsico, A. H.; Romero, A. D.; Althaus, L.; Kleinman, S. J.; Nitta, A.; Koester, D.; Külebi, B.; Jordan, S.; Kanaan, A. Seismology of a Massive Pulsating Hydrogen Atmosphere White Dwarf. , v. 757, n. 2, p. 177, Oct. 2012. Citado 2 vezes nas páginas 56 and 65.

[124] Aizenman, M.; Smeyers, P.; Weigert, A. Avoided Crossing of Modes of Non-radial Stellar Oscillations. , v. 58, p. 41, June 1977. Citado na página 56.

[125] Kilic, M.; Bergeron, P.; Kosakowski, A.; Brown, W. R.; Agüeros, M. A.; Blouin, S. The 100 pc White Dwarf Sample in the SDSS Footprint. , v. 898, n. 1, p. 84, July 2020. Citado 2 vezes nas páginas 59 and 69.

[126] Gianninas, A.; Bergeron, P.; Ruiz, M. T. A Spectroscopic Survey and Analysis of Bright, Hydrogen-rich White Dwarfs. , v. 743, n. 2, p. 138, Dec. 2011. Citado na página 59.

[127] Tremblay, P. E.; Bergeron, P.; Gianninas, A. An Improved Spectroscopic Analysis of DA White Dwarfs from the Sloan Digital Sky Survey Data Release 4. , v. 730, n. 2, p. 128, Apr. 2011. Citado na página 59.

[128] Bergeron, P.; Wesemael, F.; Lamontagne, R.; Fontaine, G.; Saffer, R. A.; Allard, N. F. Optical and Ultraviolet Analyses of ZZ Ceti Stars and Study of the Atmospheric Convective Efficiency in DA White Dwarfs. , v. 449, p. 258, Aug. 1995. Citado na página 60.

[129] Córsico, A. H.; Althaus, L. G.; Kepler, S. O.; Costa, J. E. S.; Miller Bertolami, M. M. Asteroseismological measurements on PG 1159-035, the prototype of the GW Virginis variable stars. , v. 478, n. 3, p. 869–881, Feb. 2008. Citado na página 60.

[130] Zhang, E. H.; Robinson, E. L.; Nather, R. E. The Eclipses of Cataclysmic Variables. I. HT Cassiopeiae. , v. 305, p. 740, June 1986. Citado na página 61.

[131] Pyrzas, S.; Gänsicke, B. T.; Hermes, J. J.; Copperwheat, C. M.; Rebassa-Mansergas, A.; Dhillon, V. S.; Littlefair, S. P.; Marsh, T. R.; Parsons, S. G.; Savoury, C. D. J.; Schreiber, M. R.; Barros, S. C. C.; Bento, J.; Breedt, E.; Kerry, P. Discovery of ZZ Cetis in detached white dwarf plus main-sequence binaries. , v. 447, n. 1, p. 691–697, Feb. 2015. Citado 2 vezes nas páginas 63 and 71.

[132] Robinson, E. L.; McGraw, J. T. Observations of variable white dwarfs: one new variable and 35 nonvariables. , v. 207, p. L37–L40, July 1976. Citado 2 vezes nas páginas 63 and 69.

[133] Bognár, Z.; Paparó, M.; Molnár, L.; Pápics, P. I.; Plachy, E.; Verebélyi, E.; Sódor, Á. G 207-9 and LP 133-144: light-curve analysis and asteroseismology of two ZZ Ceti stars. , v. 461, n. 4, p. 4059–4070, Oct. 2016. Citado 2 vezes nas páginas 63 and 69.

[134] Castanheira, B. G.; Kepler, S. O.; Kleinman, S. J.; Nitta, A.; Fraga, L. Discovery of five new massive pulsating white dwarf stars. , v. 430, n. 1, p. 50–59, Mar. 2013. Citado 3 vezes nas páginas 63, 66, and 67.

[135] Hermes, J. J.; Montgomery, M. H.; Mullally, F.; Winget, D. E.; Bischoff-Kim, A. A New Timescale for Period Change in the Pulsating DA White Dwarf WD 0111+0018. , v. 766, n. 1, p. 42, Mar. 2013. Citado 2 vezes nas páginas 63 and 70.

[136] Mullally, F.; Thompson, S. E.; Castanheira, B. G.; Winget, D. E.; Kepler, S. O.; Eisenstein, D. J.; Kleinman, S. J.; Nitta, A. Eleven New DA White Dwarf Variable Stars from the Sloan Digital Sky Survey. , v. 625, n. 2, p. 966–972, June 2005. Citado 2 vezes nas páginas 64 and 65.

[137] Castanheira, B. G.; Kepler, S. O.; Kleinman, S. J.; Nitta, A.; Fraga, L. New developments of the ZZ Ceti instability strip: the discovery of 11 new variables. , v. 405, n. 4, p. 2561–2569, July 2010. Citado na página 64.

[138] Fontaine, G.; Bergeron, P.; Billères, M.; Charpinet, S. A Confirmation of the Optical Spectroscopy Approach: Discovery of Two More Pulsating DA (ZZ Ceti) White Dwarfs. , v. 591, n. 2, p. 1184–1191, July 2003. Citado na página 64.

[139] Mukadam, A. S.; Mullally, F.; Nather, R. E.; Winget, D. E.; von Hippel, T.; Kleinman, S. J.; Nitta, A.; Krzesiński, J.; Kepler, S. O.; Kanaan, A.; Koester, D.; Sullivan, D. J.; Homeier, D.; Thompson, S. E.; Reaves, D.; Cotter, C.; Slaughter, D.; Brinkmann, J. Thirty-Five New Pulsating DA White Dwarf Stars. , v. 607, n. 2, p. 982–998, June 2004. Citado 3 vezes nas páginas 64, 66, and 67.

[140] Castanheira, B. G.; Kepler, S. O.; Mullally, F.; Winget, D. E.; Koester, D.; Voss, B.; Kleinman, S. J.; Nitta, A.; Eisenstein, D. J.; Napiwotzki, R.; Reimers, D. Discovery of eleven new ZZ Ceti stars. , v. 450, n. 1, p. 227–231, Apr. 2006. Citado 3 vezes nas páginas 64, 65, and 67.

[141] Castanheira, B. G.; Kepler, S. O.; Costa, A. F. M.; Giovannini, O.; Robinson, E. L.; Winget, D. E.; Kleinman, S. J.; Nitta, A.; Eisenstein, D.; Koester, D.; Santos, M. G. Towards a pure ZZ Ceti instability strip. , v. 462, n. 3, p. 989–993, Feb. 2007. Citado 2 vezes nas páginas 65 and 67.

[142] Voss, B.; Koester, D.; Østensen, R.; Kepler, S. O.; Napiwotzki, R.; Homeier, D.; Reimers, D. Discovery of seven ZZ Ceti stars using a new photometric selection method. , v. 450, n. 3, p. 1061–1070, May 2006. Citado na página 67.

[143] Kepler, S. O.; Robinson, E. L.; Nather, R. E. The light curve of the ZZ Ceti star G 226-29. , v. 271, p. 744–753, Aug. 1983. Citado na página 67.

[144] Sayres, C.; Subasavage, J. P.; Bergeron, P.; Dufour, P.; Davenport, J. R. A.; AlSayyad, Y.; Tofflemire, B. M. A Multi-survey Approach to White Dwarf Discovery. , v. 143, n. 4, p. 103, Apr. 2012. Citado na página 67.

[145] Althaus, L. G.; Gil-Pons, P.; Córsico, A. H.; Miller Bertolami, M.; De Gerónimo, F.; Camisassa, M. E.; Torres, S.; Gutierrez, J.; Rebassa-Mansergas, A. The formation of ultra-massive carbon-oxygen core white dwarfs and their evolutionary and pulsational properties. , v. 646, p. A30, Feb. 2021. Citado 2 vezes nas páginas 70 and 73.

[146] Winget, D. E.; Kepler, S. O.; Kanaan, A.; Montgomery, M. H.; Giovannini, O. An Empirical Test of the Theory of Crystallization in Stellar Interiors. , v. 487, n. 2, p. L191–L194, Oct. 1997. Citado na página 70.

[147] Kanaan, A.; Kepler, S. O.; Giovannini, O.; Diaz, M. The Discovery of a New DAV Star Using IUE Temperature Determination. , v. 390, p. L89, May 1992. Citado na página 70.

[148] Córsico, A. H.; De Gerónimo, F. C.; Camisassa, M. E.; Althaus, L. G. New fully evolutionary models for asteroseismology of ultra-massive white-dwarf stars. In: . Editors Neiner, C.; Weiss, W. W.; Baade, D.; Griffin, R. E.; Lovekin, C. C.; Moffat, A. F. J. c2020. p. 297–300. Citado 2 vezes nas páginas 70 and 71.

[149] Metcalfe, T. S.; Montgomery, M. H.; Kanaan, A. Testing White Dwarf Crystallization Theory with Asteroseismology of the Massive Pulsating DA Star BPM 37093. , v. 605, n. 2, p. L133–L136, Apr. 2004. Citado na página 70.

[150] Montgomery, M. H.; Metcalfe, T. S.; Winget, D. E. The core/envelope symmetry in pulsating stars. , v. 344, n. 2, p. 657–664, Sept. 2003. Citado na página 71.

[151] Gaia Collaboration; Brown, A. G. A.; Vallenari, A.; Prusti, T.; de Bruijne, J. H. J.; Babusiaux, C.; Bailer-Jones, C. A. L.; Biermann, M.; Evans, D. W.; Eyer, L.; Jansen, F.; Jordi, C.; Klioner, S. A.; Lammers, U.; Lindegren, L.; Luri, X.; Mignard, F.; Panem, C.; Pourbaix, D.; Randich, S.; Sartoretti, P.; Siddiqui, H. I.; Soubiran, C.; van Leeuwen, F.; Walton, N. A.; Arenou, F.; Bastian, U.; Cropper, M.; Drimmel, R.; Katz, D.; Lattanzi, M. G.; Bakker, J.; Cacciari, C.; Castañeda, J.; Chaoul, L.; Cheek, N.; De Angeli, F.; Fabricius, C.; Guerra, R.; Holl, B.; Masana, E.; Messineo, R.; Mowlavi, N.; Nienartowicz, K.; Panuzzo, P.; Portell, J.; Riello, M.; Seabroke, G. M.; Tanga, P.; Thévenin, F.; Gracia-Abril, G.; Comoretto, G.; Garcia-Reinaldos, M.; Teyssier, D.; Altmann, M.; Andrae, R.; Audard, M.; Bellas-Velidis, I.; Benson, K.; Berthier, J.; Blomme, R.; Burgess, P.; Busso, G.; Carry, B.; Cellino, A.; Clementini, G.; Clotet, M.; Creevey, O.; Davidson, M.; De Ridder, J.; Delchambre, L.; Dell'Oro, A.; Ducourant, C.; Fernández-Hernández, J.; Fouesneau, M.; Frémat, Y.; Galluccio, L.; García-Torres, M.; González-Núñez, J.; González-Vidal, J. J.; Gosset, E.; Guy, L. P.; Halbwachs, J. L.; Hambly, N. C.; Harrison, D. L.; Hernández, J.; Hestroffer, D.; Hodgkin, S. T.; Hutton, A.; Jasniewicz, G.; Jean-Antoine-Piccolo, A.; Jordan, S.; Korn, A. J.; Krone-Martins, A.; Lanzafame, A. C.; Lebzelter, T.; Löffler, W.; Manteiga, M.; Marrese, P. M.; Martín-Fleitas, J. M.; Moitinho, A.; Mora, A.; Muinonen, K.; Osinde, J.; Pancino, E.; Pauwels, T.; Petit, J. M.; Recio-Blanco, A.; Richards, P. J.; Rimoldini, L.; Robin, A. C.; Sarro, L. M.; Siopis, C.; Smith, M.; Sozzetti, A.; Süveges, M.; Torra, J.; van Reeven, W.; Abbas, U.; Abreu Aramburu, A.; Accart, S.; Aerts, C.; Altavilla, G.; Álvarez, M. A.; Alvarez, R.; Alves, J.; Anderson, R. I.; Andrei, A. H.; Anglada Varela, E.; Antiche, E.; Antoja, T.; Arcay, B.; Astraatmadja, T. L.; Bach, N.; Baker, S. G.; Balaguer-Núñez, L.; Balm, P.; Barache, C.; Barata, C.; Barbato, D.; Barblan, F.; Barklem, P. S.; Barrado, D.; Barros, M.; Barstow, M. A.; Bartholomé Muñoz, S.; Bassilana, J. L.; Becciani, U.; Bellazzini, M.; Berihuete, A.; Bertone, S.; Bianchi, L.; Bienaymé, O.; Blanco-Cuaresma, S.; Boch, T.; Boeche, C.; Bombrun, A.; Borrachero, R.; Bossini, D.; Bouquillon, S.; Bourda, G.; Bragaglia, A.; Bramante, L.; Breddels, M. A.; Bressan, A.; Brouillet, N.; Brüsemeister, T.; Brugaletta, E.;

Bucciarelli, B.; Burlacu, A.; Busonero, D.; Butkevich, A. G.; Buzzi, R.; Caffau, E.; Cancelliere, R.; Cannizzaro, G.; Cantat-Gaudin, T.; Carballo, R.; Carlucci, T.; Carrasco, J. M.; Casamiquela, L.; Castellani, M.; Castro-Ginard, A.; Charlot, P.; Chemin, L.; Chiavassa, A.; Cocozza, G.; Costigan, G.; Cowell, S.; Crifo, F.; Crosta, M.; Crowley, C.; Cuypers, J.; Dafonte, C.; Damerdji, Y.; Dapergolas, A.; David, P.; David, M.; de Laverny, P.; De Luise, F.; De March, R.; de Martino, D.; de Souza, R.; de Torres, A.; Debosscher, J.; del Pozo, E.; Delbo, M.; Delgado, A.; Delgado, H. E.; Di Matteo, P.; Diakite, S.; Diener, C.; Distefano, E.; Dolding, C.; Drazinos, P.; Durán, J.; Edvardsson, B.; Enke, H.; Eriksson, K.; Esquej, P.; Eynard Bontemps, G.; Fabre, C.; Fabrizio, M.; Faigler, S.; Falcão, A. J.; Farràs Casas, M.; Federici, L.; Fedorets, G.; Fernique, P.; Figueras, F.; Filippi, F.; Findeisen, K.; Fonti, A.; Fraile, E.; Fraser, M.; Frézouls, B.; Gai, M.; Galleti, S.; Garabato, D.; García-Sedano, F.; Garofalo, A.; Garralda, N.; Gavel, A.; Gavras, P.; Gerssen, J.; Geyer, R.; Giacobbe, P.; Gilmore, G.; Girona, S.; Giuffrida, G.; Glass, F.; Gomes, M.; Granvik, M.; Gueguen, A.; Guerrier, A.; Guiraud, J.; Gutiérrez-Sánchez, R.; Haigron, R.; Hatzidimitriou, D.; Hauser, M.; Haywood, M.; Heiter, U.; Helmi, A.; Heu, J.; Hilger, T.; Hobbs, D.; Hofmann, W.; Holland, G.; Huckle, H. E.; Hypki, A.; Icardi, V.; Janßen, K.; Jevardat de Fombelle, G.; Jonker, P. G.; Juhász, Á. L.; Julbe, F.; Karampelas, A.; Kewley, A.; Klar, J.; Kochoska, A.; Kohley, R.; Kolenberg, K.; Kontizas, M.; Kontizas, E.; Koposov, S. E.; Kordopatis, G.; Kostrzewa-Rutkowska, Z.; Koubsky, P.; Lambert, S.; Lanza, A. F.; Lasne, Y.; Lavigne, J. B.; Le Fustec, Y.; Le Poncin-Lafitte, C.; Lebreton, Y.; Leccia, S.; Leclerc, N.; Lecoeur-Taibi, I.; Lenhardt, H.; Leroux, F.; Liao, S.; Licata, E.; Lindstrøm, H. E. P.; Lister, T. A.; Livanou, E.; Lobel, A.; López, M.; Managau, S.; Mann, R. G.; Mantelet, G.; Marchal, O.; Marchant, J. M.; Marconi, M.; Marinoni, S.; Marschalkó, G.; Marshall, D. J.; Martino, M.; Marton, G.; Mary, N.; Massari, D.; Matijevič, G.; Mazeh, T.; McMillan, P. J.; Messina, S.; Michalik, D.; Millar, N. R.; Molina, D.; Molinaro, R.; Molnár, L.; Montegriffo, P.; Mor, R.; Morbidelli, R.; Morel, T.; Morris, D.; Mulone, A. F.; Muraveva, T.; Musella, I.; Nelemans, G.; Nicastro, L.; Noval, L.; O'Mullane, W.; Ordénovic, C.; Ordóñez-Blanco, D.; Osborne, P.; Pagani, C.; Pagano, I.; Pailler, F.; Palacin, H.; Palaversa, L.; Panahi, A.; Pawlak, M.; Piersimoni, A. M.; Pineau, F. X.; Plachy, E.; Plum, G.; Poggio, E.; Poujoulet, E.; Prša, A.; Pulone, L.; Racero, E.; Ragaini, S.; Rambaux, N.; Ramos-Lerate, M.; Regibo, S.; Reylé, C.; Riclet, F.; Ripepi, V.; Riva, A.; Rivard, A.; Rixon, G.; Roegiers, T.; Roelens, M.; Romero-Gómez, M.; Rowell, N.; Royer, F.; Ruiz-Dern, L.; Sadowski, G.; Sagristà Sellés, T.; Sahlmann, J.; Salgado, J.; Salguero, E.; Sanna, N.; Santana-Ros, T.; Sarasso, M.; Savietto, H.; Schultheis, M.; Sciacca, E.; Segol, M.; Segovia, J. C.; Ségransan, D.; Shih, I. C.; Siltala, L.; Silva, A. F.; Smart, R. L.; Smith, K. W.; Solano, E.; Solitro, F.; Sordo, R.; Soria Nieto, S.; Souchay, J.; Spagna, A.; Spoto, F.; Stampa, U.; Steele, I. A.;

Steidelmüller, H.; Stephenson, C. A.; Stoev, H.; Suess, F. F.; Surdej, J.; Szabados, L.; Szegedi-Elek, E.; Tapiador, D.; Taris, F.; Tauran, G.; Taylor, M. B.; Teixeira, R.; Terrett, D.; Teyssandier, P.; Thuillot, W.; Titarenko, A.; Torra Clotet, F.; Turon, C.; Ulla, A.; Utrilla, E.; Uzzi, S.; Vaillant, M.; Valentini, G.; Valette, V.; van Elteren, A.; Van Hemelryck, E.; van Leeuwen, M.; Vaschetto, M.; Vecchiato, A.; Veljanoski, J.; Viala, Y.; Vicente, D.; Vogt, S.; von Essen, C.; Voss, H.; Votruba, V.; Voutsinas, S.; Walmsley, G.; Weiler, M.; Wertz, O.; Wevers, T.; Wyrzykowski, Ł.; Yoldas, A.; Žerjal, M.; Ziaeepour, H.; Zorec, J.; Zschocke, S.; Zucker, S.; Zurbach, C.; Zwitter, T. Gaia Data Release 2. Summary of the contents and survey properties. , v. 616, p. A1, Aug. 2018. Citado na página 73.

[152] Gaia Collaboration; Brown, A. G. A.; Vallenari, A.; Prusti, T.; de Bruijne, J. H. J.; Babusiaux, C.; Biermann, M.; Creevey, O. L.; Evans, D. W.; Eyer, L.; Hutton, A.; Jansen, F.; Jordi, C.; Klioner, S. A.; Lammers, U.; Lindegren, L.; Luri, X.; Mignard, F.; Panem, C.; Pourbaix, D.; Randich, S.; Sartoretti, P.; Soubiran, C.; Walton, N. A.; Arenou, F.; Bailer-Jones, C. A. L.; Bastian, U.; Cropper, M.; Drimmel, R.; Katz, D.; Lattanzi, M. G.; van Leeuwen, F.; Bakker, J.; Cacciari, C.; Castañeda, J.; De Angeli, F.; Ducourant, C.; Fabricius, C.; Fouesneau, M.; Frémat, Y.; Guerra, R.; Guerrier, A.; Guiraud, J.; Jean-Antoine Piccolo, A.; Masana, E.; Messineo, R.; Mowlavi, N.; Nicolas, C.; Nienartowicz, K.; Pailler, F.; Panuzzo, P.; Riclet, F.; Roux, W.; Seabroke, G. M.; Sordo, R.; Tanga, P.; Thévenin, F.; Gracia-Abril, G.; Portell, J.; Teyssier, D.; Altmann, M.; Andrae, R.; Bellas-Velidis, I.; Benson, K.; Berthier, J.; Blomme, R.; Brugaletta, E.; Burgess, P. W.; Busso, G.; Carry, B.; Cellino, A.; Cheek, N.; Clementini, G.; Damerdji, Y.; Davidson, M.; Delchambre, L.; Dell'Oro, A.; Fernández-Hernández, J.; Galluccio, L.; García-Lario, P.; Garcia-Reinaldos, M.; González-Núñez, J.; Gosset, E.; Haigron, R.; Halbwachs, J. L.; Hambly, N. C.; Harrison, D. L.; Hatzidimitriou, D.; Heiter, U.; Hernández, J.; Hestroffer, D.; Hodgkin, S. T.; Holl, B.; Janßen, K.; Jevardat de Fombelle, G.; Jordan, S.; Krone-Martins, A.; Lanzafame, A. C.; Löffler, W.; Lorca, A.; Manteiga, M.; Marchal, O.; Marrese, P. M.; Moitinho, A.; Mora, A.; Muinonen, K.; Osborne, P.; Pancino, E.; Pauwels, T.; Petit, J. M.; Recio-Blanco, A.; Richards, P. J.; Riello, M.; Rimoldini, L.; Robin, A. C.; Roegiers, T.; Rybizki, J.; Sarro, L. M.; Siopis, C.; Smith, M.; Sozzetti, A.; Ulla, A.; Utrilla, E.; van Leeuwen, M.; van Reeven, W.; Abbas, U.; Abreu Aramburu, A.; Accart, S.; Aerts, C.; Aguado, J. J.; Ajaj, M.; Altavilla, G.; Álvarez, M. A.; Álvarez Cid-Fuentes, J.; Alves, J.; Anderson, R. I.; Anglada Varela, E.; Antoja, T.; Audard, M.; Baines, D.; Baker, S. G.; Balaguer-Núñez, L.; Balbinot, E.; Balog, Z.; Barache, C.; Barbato, D.; Barros, M.; Barstow, M. A.; Bartolomé, S.; Bassilana, J. L.; Bauchet, N.; Baudesson-Stella, A.; Becciani, U.; Bellazzini, M.; Bernet, M.; Bertone, S.; Bianchi, L.; Blanco-Cuaresma, S.; Boch, T.; Bombrun, A.; Bossini, D.; Bouquillon, S.; Bragaglia, A.; Bramante, L.; Breedt, E.; Bressan, A.;

Brouillet, N.; Bucciarelli, B.; Burlacu, A.; Busonero, D.; Butkevich, A. G.; Buzzi, R.; Caffau, E.; Cancelliere, R.; Cánovas, H.; Cantat-Gaudin, T.; Carballo, R.; Carlucci, T.; Carnerero, M. I.; Carrasco, J. M.; Casamiquela, L.; Castellani, M.; Castro-Ginard, A.; Castro Sampol, P.; Chaoul, L.; Charlot, P.; Chemin, L.; Chiavassa, A.; Cioni, M. R. L.; Comoretto, G.; Cooper, W. J.; Cornez, T.; Cowell, S.; Crifo, F.; Crosta, M.; Crowley, C.; Dafonte, C.; Dapergolas, A.; David, M.; David, P.; de Laverny, P.; De Luise, F.; De March, R.; De Ridder, J.; de Souza, R.; de Teodoro, P.; de Torres, A.; del Peloso, E. F.; del Pozo, E.; Delbo, M.; Delgado, A.; Delgado, H. E.; Delisle, J. B.; Di Matteo, P.; Diakite, S.; Diener, C.; Distefano, E.; Dolding, C.; Eappachen, D.; Edvardsson, B.; Enke, H.; Esquej, P.; Fabre, C.; Fabrizio, M.; Faigler, S.; Fedorets, G.; Fernique, P.; Fienga, A.; Figueras, F.; Fouron, C.; Fragkoudi, F.; Fraile, E.; Franke, F.; Gai, M.; Garabato, D.; Garcia-Gutierrez, A.; García-Torres, M.; Garofalo, A.; Gavras, P.; Gerlach, E.; Geyer, R.; Giacobbe, P.; Gilmore, G.; Girona, S.; Giuffrida, G.; Gomel, R.; Gomez, A.; Gonzalez-Santamaria, I.; González-Vidal, J. J.; Granvik, M.; Gutiérrez-Sánchez, R.; Guy, L. P.; Hauser, M.; Haywood, M.; Helmi, A.; Hidalgo, S. L.; Hilger, T.; Hładczuk, N.; Hobbs, D.; Holland, G.; Huckle, H. E.; Jasniewicz, G.; Jonker, P. G.; Juaristi Campillo, J.; Julbe, F.; Karbevska, L.; Kervella, P.; Khanna, S.; Kochoska, A.; Kontizas, M.; Kordopatis, G.; Korn, A. J.; Kostrzewa-Rutkowska, Z.; Kruszyńska, K.; Lambert, S.; Lanza, A. F.; Lasne, Y.; Le Campion, J. F.; Le Fustec, Y.; Lebreton, Y.; Lebzelter, T.; Leccia, S.; Leclerc, N.; Lecoeur-Taibi, I.; Liao, S.; Licata, E.; Lindstrøm, E. P.; Lister, T. A.; Livanou, E.; Lobel, A.; Madrero Pardo, P.; Managau, S.; Mann, R. G.; Marchant, J. M.; Marconi, M.; Marcos Santos, M. M. S.; Marinoni, S.; Marocco, F.; Marshall, D. J.; Martin Polo, L.; Martín-Fleitas, J. M.; Masip, A.; Massari, D.; Mastrobuono-Battisti, A.; Mazeh, T.; McMillan, P. J.; Messina, S.; Michalik, D.; Millar, N. R.; Mints, A.; Molina, D.; Molinaro, R.; Molnár, L.; Montegriffo, P.; Mor, R.; Morbidelli, R.; Morel, T.; Morris, D.; Mulone, A. F.; Munoz, D.; Muraveva, T.; Murphy, C. P.; Musella, I.; Noval, L.; Ordénovic, C.; Orrù, G.; Osinde, J.; Pagani, C.; Pagano, I.; Palaversa, L.; Palicio, P. A.; Panahi, A.; Pawlak, M.; Peñalosa Esteller, X.; Penttilä, A.; Piersimoni, A. M.; Pineau, F. X.; Plachy, E.; Plum, G.; Poggio, E.; Poretti, E.; Poujoulet, E.; Prša, A.; Pulone, L.; Racero, E.; Ragaini, S.; Rainer, M.; Raiteri, C. M.; Rambaux, N.; Ramos, P.; Ramos-Lerate, M.; Re Fiorentin, P.; Regibo, S.; Reylé, C.; Ripepi, V.; Riva, A.; Rixon, G.; Robichon, N.; Robin, C.; Roelens, M.; Rohrbasser, L.; Romero-Gómez, M.; Rowell, N.; Royer, F.; Rybicki, K. A.; Sadowski, G.; Sagristà Sellés, A.; Sahlmann, J.; Salgado, J.; Salguero, E.; Samaras, N.; Sanchez Gimenez, V.; Sanna, N.; Santoveña, R.; Sarasso, M.; Schultheis, M.; Sciacca, E.; Segol, M.; Segovia, J. C.; Ségransan, D.; Semeux, D.; Shahaf, S.; Siddiqui, H. I.; Siebert, A.; Siltala, L.; Slezak, E.; Smart, R. L.; Solano, E.; Solitro, F.; Souami, D.; Souchay, J.; Spagna, A.; Spoto, F.; Steele, I. A.; Steidelmüller, H.; Stephenson, C. A.; Süveges,

M.; Szabados, L.; Szegedi-Elek, E.; Taris, F.; Tauran, G.; Taylor, M. B.; Teixeira, R.; Thuillot, W.; Tonello, N.; Torra, F.; Torra, J.; Turon, C.; Unger, N.; Vaillant, M.; van Dillen, E.; Vanel, O.; Vecchiato, A.; Viala, Y.; Vicente, D.; Voutsinas, S.; Weiler, M.; Wevers, T.; Wyrzykowski, Ł.; Yoldas, A.; Yvard, P.; Zhao, H.; Zorec, J.; Zucker, S.; Zurbach, C.; Zwitter, T. Gaia Early Data Release 3. Summary of the contents and survey properties. , v. 649, p. A1, May 2021. Citado na página 73.

[153] Gentile Fusillo, N. P.; Tremblay, P. E.; Cukanovaite, E.; Vorontseva, A.; Lallement, R.; Hollands, M.; Gänsicke, B. T.; Burdge, K. B.; McCleery, J.; Jordan, S. A catalogue of white dwarfs in Gaia EDR3. *arXiv e-prints*, p. arXiv:2106.07669, June 2021. Citado na página 73.

[154] Kowalski, P. M.; Saumon, D. Found: The Missing Blue Opacity in Atmosphere Models of Cool Hydrogen White Dwarfs. , v. 651, n. 2, p. L137–L140, Nov. 2006. Citado na página 73.

[155] Kowalski, P. M.; Saumon, D. Found: The Missing Blue Opacity in Atmosphere Models of Cool Hydrogen White Dwarfs. , v. 651, n. 2, p. L137–L140, Nov. 2006. Citado na página 73.

[156] Gentile Fusillo, N. P.; Tremblay, P. E.; Gaensicke, B. T.; Manser, C. J.; Cunningham, T.; Cukanovaite, E.; Hollands, M.; Marsh, T.; Raddi, R.; Jordan, S.; Toonen, S.; Geier, S.; Barstow, M.; Cummings, J. D. VizieR Online Data Catalog: Gaia DR2 white dwarf candidates (Gentile Fusillo+, 2019). *VizieR Online Data Catalog*, p. J/MNRAS/482/4570, Jan. 2019. Citado na página 73.

[157] Tremblay, P. E.; Bergeron, P. The Ratio of Helium- to Hydrogen-Atmosphere White Dwarfs: Direct Evidence for Convective Mixing. , v. 672, n. 2, p. 1144–1152, Jan. 2008. Citado 3 vezes nas páginas 77, 78, and 79.

[158] Ourique, G.; Kepler, S. O.; Romero, A. D.; Klippel, T. S.; Koester, D. Evidence of spectral evolution on the white dwarf sample from the Gaia mission. , v. 492, n. 4, p. 5003–5010, Mar. 2020. Citado na página 79.

[159] Mason, B. D.; Hartkopf, W. I.; Miles, K. N. Binary Star Orbits. V. The Nearby White Dwarf/Red Dwarf Pair 40 Eri BC. , v. 154, n. 5, p. 200, Nov. 2017. Citado na página 79.

[160] Bond, H. E.; Bergeron, P.; Bédard, A. Astrophysical Implications of a New Dynamical Mass for the Nearby White Dwarf 40 Eridani B. , v. 848, n. 1, p. 16, Oct. 2017. Citado na página 79.

[161] Kleinman, S. J.; Kepler, S. O.; Koester, D.; Pelisoli, I.; Peçanha, V.; Nitta, A.; Costa, J. E. S.; Krzesinski, J.; Dufour, P.; Lachapelle, F. R.; Bergeron, P.; Yip, C.-W.;

Harris, H. C.; Eisenstein, D. J.; Althaus, L.; Córsico, A. SDSS DR7 White Dwarf Catalog. , v. 204, n. 1, p. 5, Jan. 2013. Citado na página 81.

Appendices